ALTERNATIVE BUFFER LAYER DEVELOPMENT IN $Cu(In,Ga)Se_2$ THIN FILM SOLAR CELLS

by

Peipei Xin

A dissertation submitted to the Faculty of the University of Delaware in partial fulfillment of the requirements for the degree of Doctor of Philosophy in Materials Science and Engineering

Winter 2017

ALTERNATIVE BUFFER LAYER DEVELOPMENT IN

$Cu(In,Ga)Se_2$ THIN FILM SOLAR CELLS

by

Peipei Xin

Approved: _____

Darrin J. Pochan, Ph.D.
Chair of the Department of Materials Science and Engineering

Approved: _____

Babatunde A. Ogunnaike, Ph.D.
Dean of the College of Engineering

Approved: _____

Ann L. Ardis, Ph.D.
Senior Vice Provost for Graduate and Professional Education

I certify that I have read this dissertation and that in my opinion it meets the academic and professional standard required by the University as a dissertation for the degree of Doctor of Philosophy.

Signed: _____

William N. Shafarman, Ph.D.
Professor in charge of dissertation

I certify that I have read this dissertation and that in my opinion it meets the academic and professional standard required by the University as a dissertation for the degree of Doctor of Philosophy.

Signed: _____

Robert W. Birkmire, Ph.D.
Member of dissertation committee

I certify that I have read this dissertation and that in my opinion it meets the academic and professional standard required by the University as a dissertation for the degree of Doctor of Philosophy.

Signed: _____

Robert L. Opila, Ph.D.
Member of dissertation committee

I certify that I have read this dissertation and that in my opinion it meets the academic and professional standard required by the University as a dissertation for the degree of Doctor of Philosophy.

Signed: _____

John Q. Xiao, Ph.D.
Member of dissertation committee

I certify that I have read this dissertation and that in my opinion it meets the academic and professional standard required by the University as a dissertation for the degree of Doctor of Philosophy.

Signed: _____

Brian E. McCandless, B.S.
Member of dissertation committee

ACKNOWLEDGMENTS

I would like to first express my deepest and sincerest gratitude to my advisor Prof. William N. Shafarman for providing me the opportunity to conduct research at the Institute of Energy Conversion and invaluable guidance during my PhD study. I would like to thank Prof. Robert Birkmire and Brian McCandless for their insightful advice and discussions about my research work. I would also like to thank Prof. Robert Opila and Prof. John Xiao for serving on my committee and providing helpful input and feedback to my thesis.

I would like to acknowledge the funding support from DOE FPACE program for my PhD research.

I would like to thank the technical support and assistance from the following staff and students at the Institute of Energy Conversion and Materials Science and Engineering Department: Wayne Buchanan, Jes Larsen, Christopher Thompson, John Elliott, Kevin Dobson, Shannon Fields, Dan Ryan, Kevin Hart, JinWoo Lee, Kihwan Kim, Steve Hegedus, Dominik Berg, Greg Hanket, Fei Deng, Lulu Zhang, Brent Shu, Lala Zhu, Tiejun Meng, Robert Forest, Sina Soltanmohammad, Jianbo He, Hamed Simchi, and Kevin Jones. My PhD research would not have been possible without their kindly help in the past six years.

I would like to thank Dr. Mary Martin, Paula Newton, Sherry Stewart, Kathleen Forwood, Naima Hall for their administrative support.

Finally I would like to thank my parents for their love, understanding and moral support. It has been a long journey, and I’m truly thankful that they are there.

TABLE OF CONTENTS

LIST OF TABLES

LIST OF FIGURES

ABSTRACT

$Cu(In,Ga)Se_2$-based thin film solar cells are considered to be one of the most promising photovoltaic technologies. $Cu(In,Ga)Se_2$ (CIGS) solar devices have the potential advantage of low-cost, fast fabrication by using semiconductor layers of only a few micrometers thick and high efficiency photovoltaics have been reported at both the cell and the module levels. CdS via chemical bath deposition (CBD) has been the most widely used buffer option to form the critical junction in CIGS-based thin film photovoltaic devices. However, the disadvantages of CdS can't be ignored - regulations on cadmium usage are getting stricter primarily due to its toxicity and environmental impacts, and the proper handling of the large amount of toxic chemical bath waste is a massive and expensive task.

This dissertation is devoted to the development of Cd-free alternative buffer layers in CIGS-based thin film solar cells. Based on the considerations of buffer layer selection criteria and extensive literature review, Zn-compound buffer materials are chosen as the primary investigation candidates. Radio frequency magnetron sputtering is the preferred buffer deposition approach since it's a clean and more controllable technique compared to CBD, and is readily scaled to large area manufacturing.

First, a comprehensive study of the $ZnSe_{1-x}O_x$ compound prepared by reactive sputtering was completed. As the oxygen content in the reactive sputtering gas increased, $ZnSe_{1-x}O_x$ crystallinity and bandgap decreased. It's observed that oxygen miscibility in ZnSe was low and a secondary phase formed when the O_2 / (O_2 + Ar) ratio in the sputtering gas exceeded 2%. Two approaches were proposed to optimize

the band alignment between the CIGS and buffer layer. One method focused on the bandgap engineering of the absorber, the other focused on the band structure modification of the buffer. As a result, improved current of the solar cell was achieved although a carrier transport barrier at the junction interface still limited the device performance.

Second, an investigation of Zn(S,O) buffer layers was completed. Zn(S,O) films were sputtered in Ar using a $ZnO_{0.7}S_{0.3}$ compound target. Zn(S,O) films had the composition close to the target with S / (S+O) ratio around 0.3. Zn(S,O) films showed the wurtzite structure with the bandgap about 3.2eV. The champion $Cu(In,Ga)Se_2$ / Zn(S,O) cell had 12.5% efficiency and an $(Ag,Cu)(In,Ga)Se_2$ / Zn(S,O) cell achieved 13.2% efficiency. Detailed device analysis was used to study the $Cu(In,Ga)Se_2$ and $(Ag,Cu)(In,Ga)Se_2$ absorbers, the influence of absorber surface treatments, the effects of device treatments, the sputtering damage and the Na concentration in the absorber.

Finally alternative buffer layer development was applied to an innovative superstrate CIGS configuration. The superstrate structure has potential benefits of improved window layer properties, cost reduction, and the possibility to implement back reflector engineering techniques. The application of three buffer layer options – CdS, ZnO and ZnSe was studied and limitations of each were characterized. The best device achieved 8.6% efficiency with a ZnO buffer. Ga_xO_y formation at the junction interface was the main limiting factor of this device performance. For CdS / CIGS and ZnSe / CIGS superstrate devices extensive inter-diffusion between the absorber and buffer layer under CIGS growth conditions was the critical problem. Inter-diffusion severely deteriorated the junction quality and led to poorly behaved devices, despite different efforts to optimize the fabrication process.

Chapter 1

INTRODUCTION

1.1 Cu(In,Ga)Se_2 Photovoltaic Technology

1.1.1 CIGS Thin Film Solar Cells

Solar energy is the ultimate energy source for all life on earth. It's such a powerful source that the energy from the sun that falls on the earth in one hour is more than we need in one year. How to harness the solar energy is always a critical topic for all human beings. Photovoltaic technology is one of the most important technologies that are being developed to effectively utilize the solar energy. It directly converts the incident sunlight into electricity with minimum impact to the environment.

As a renewable energy source, the history of the photovoltaic devices is not long. Starting from the crystalline Si solar cells in the 1950s, more and more materials and technologies are being discovered and developed as the newer generations of the solar devices. Among them, Cu(In,Ga)Se_2-based thin film solar cells have been considered as one of the most promising technologies. Thin film photovoltaic devices have the advantages of low-cost, fast-fabrication by using semiconductor layers of only a few micrometers thick. High efficiency Cu(In,Ga)Se_2 (CIGS) devices have been reported at both the cell and the module levels worldwide. The champion lab-scale CIGS device has achieved 22.6% efficiency with the 0.5 cm^2 cell area [1]. Module efficiencies over 16% have also been demonstrate by several laboratories and companies [2, 3].

1.1.2 CIGS Solar Cell Configurations

1.1.2.1 Substrate Configuration

High efficiency CIGS-based solar cells normally employ the substrate configuration which is centered around the CIGS / buffer heterojunction, as shown in Figure 1.1 (a). In the substrate structure, the device fabrication starts with the molybdenum back contact deposition on the soda-lime glass (SLG), followed by the CIGS absorber deposition. A $MoSe_2$ interface layer between Mo and CIGS has been confirmed to form during the high temperature growth of the CIGS layer [4], which enhances the device performance by providing an ohmic contact. After that is the buffer layer growth on top of the CIGS to form the critical junction diode of the solar device. Currently the chemical bath deposited (CBD) CdS is the most common buffer option (and such devices are referred to as the baseline cells in this work), but other buffer candidate materials like Zn- or In- compounds and alternative deposition approaches are being investigated, primarily due to the adverse environmental impacts of CdS. Then a thin high resistance intrinsic ZnO (i-ZnO) layer and a transparent conductive oxide (TCO) layer – indium tin oxide (ITO) – are deposited as the front window layers. The device is completed by the deposition of the Ni/Al contact grids. The sunlight shines through the TCO window layer.

1.1.2.2 Superstrate Configuration

The superstrate configuration for a CIGS device as shown in Figure 1.1 (b) is less studied. In this structure the fabrication sequences are reversed compared to the substrate devices. It starts with the TCO window layer and buffer depositions, followed by the CIGS absorber growth. The Au back contact is used in this case. The final solar cell is illuminated through the SLG.

There are several potential advantages of the superstrate structure. It enables the high temperature process optimization of TCO window layers for improved long-term optoelectronic properties. Degradation of the TCO layers in substrate cells has been identified as one mechanism for deterioration of CIGS devices [5]. The superstrate device offers a pathway to a tandem cell structure [6]. It also provides the possibility to implement light trapping and back reflector engineering techniques. This is important for better solar energy utilization of CIGS absorber layers with thickness below 1 µm where a significant fraction of the incident light is not absorbed in a single pass through the device. Thinner CIGS absorbers are critical for cost-effective module productions. Furthermore, the superstrate device eliminates the need of a transparent encapsulation (usually glass or EVA films) as for normal substrate devices, which can lead to cost and weight reductions.

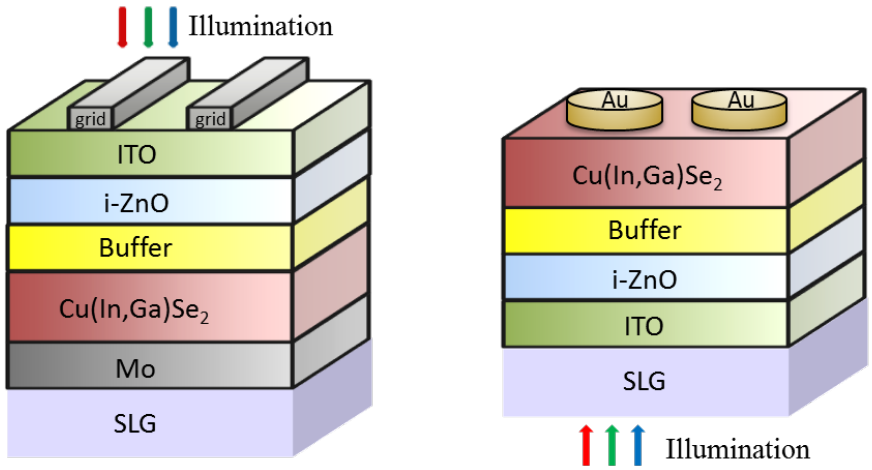

(a) Substrate configuration (b) Superstrate configuration

Figure 1.1: (a) CIGS-based solar cell in the substrate configuration. (b) CIGS-based solar cell in the superstrate configuration.

1.1.3 Basics of CIGS Device Operation

The essential component of the CIGS-based solar cells is the p-n junction formed by the p-type CIGS layer and the n-type buffer layer. The sunlight is primarily absorbed in the CIGS layer. The photogenerated electron-hole pairs are created and then separated by the built-in electric field in the space charge region (SCR). The electrons are transported to the front contact / window layers and the holes are collected by the back contact. The analysis of CIGS devices is largely dependent on the previous experience with the crystalline Si solar cells. Considerable efforts have been put on building the theoretical models to explain the behaviors of interfaces, defect states, grain boundaries and so on that occur with polycrystalline thin film solar cells, but the underlying device mechanism of CIGS-based thin film solar cells is still an incomplete picture.

The CIGS device analysis is mainly about identifying the loss mechanisms, which generally consist of three categories [7]. The first one is the optical loss that affects the generation of photo-carriers and the short circuit current (J_{sc}) of the solar devices. Quantum efficiency (QE) is a powerful tool to characterize the optical loss. The QE results are controlled by the bandgap of the CIGS absorber, front surface reflection, parasitic absorption in the front window and buffer layer, and incomplete absorption in the CIGS absorber. The analysis of the QE spectrum with measured reflection can effectively point out the specific optical loss problems of the devices. The corresponding optimization solutions include the deposition of anti-reflection (AR) coating layer, the use of light trapping techniques, the application of wider bandgap buffer/window material, the improvement of the absorber quality and so on.

The second loss mechanism is the electron-hole recombination in the device that affects the open circuit voltage (V_{oc}) and fill factor (FF). As shown in Figure.2,

there are several possible recombination pathways in CIGS devices including: 1 – buffer / absorber interface recombination; 2 – space charge region (SCR) or depletion region recombination; 3 – quasi neutral region (QNR) or CIGS bulk recombination; 4 – absorber / back contact (Mo) interface recombination. The current – voltage (J-V) relation of solar cells can be expressed by the general diode equation [7]:

$$J = J_0 \exp[\frac{q}{AkT}(V - R_s J] + G(V - R_s J) - J_L \quad (1.1)$$

And the diode current J_0 can be further written as:

$$J_0 = J_{00} \exp(-\frac{\Phi_b}{AkT}) \quad (1.2)$$

Here R_s stands for the series resistance, G stands for the shunt conductance, and J_L is the light generated current. The analysis of the ideality factor A, the barrier height Φ_b, and the prefactor J_{00} can be used to identify the dominant recombination current of a specific device [8, 9].

A well-behaved CIGS / CdS solar cell is normally controlled by Shockley – Read – Hall recombination occurring in the SCR or QNR of CIGS layer through deep trap states, which are lying in the midgap of the CIGS where the supply of both electrons and holes is adequate [10]. The ideality factor A varies between 1 and 2, depending upon the energy positions of those defect states [11]. The absorber / buffer interface recombination is generally not limiting the performance of a baseline CIGS cell with the CBD-CdS buffer, although defects due to the lattice mismatch and air exposure do exist at this critical interface. The main explanation of this phenomenon is the type inversion of the absorber surface region near the heterojunction [9, 12]. The type inversion makes the absorber surface a thin n^+ layer as seen in Figure 1.2. Hence the electrons in this region become the actual majority carriers and the interface recombination is suppressed by the limited amount of holes. Besides that, the nature of

CIGS Cu-poor surface as discussed in 1.2.1 later leads to a decrease in the valence band maximum based on the theoretical models [8, 13], also shown in Figure 1.2. This surface valence band bending forms an effective barrier for the hole transport to the junction interface and further inhibits the recombination current. However, the story might be different when the baseline device fabrication steps are modified, including the application of alternative buffer materials or deposition approaches, and the variations of the absorber layer qualities. In those cases, the absorber / buffer interface recombination might severely limit the device performance. The effect of the absorber / back contact interface recombination is usually negligible for the baseline CIGS devices but could be a problem for the devices with the CIGS layer thickness less than 1 μm, since once the minority diffusion length exceeds the absorber thickness, the recombination at the back surface will contribute to the device V_{OC} loss [14, 15]. The possible solutions include the use of back reflector and a Ga / bandgap gradient towards the back to repel electrons [16].

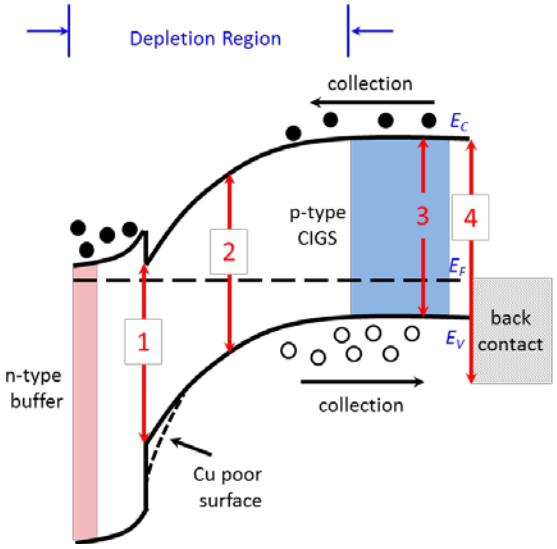

Figure 1.2: The band diagram of CIGS / buffer hetero-junction. The numbered pathways are the possible electron-hole recombination routes. 1 – buffer / absorber interface recombination; 2 – SCR recombination; 3 – QNR recombination; 4 – absorber / back contact interface recombination.

Finally, the last efficiency loss originates from parasitic losses including series resistance, shunt conductance and voltage-dependent current collection, which are primarily reflected by the decreased FF but can also affect V_{oc} and J_{sc} [7]. Those parasitic losses could induce serious fabrication issues during the module production.

1.2 CIGS Absorber

1.2.1 Structural, Optical and Electrical Properties

As a p-type semiconductor material, the CIGS film is the core layer of the CIGS-based solar devices. It is an alloy of $CuInSe_2$ and $CuGaSe_2$ with the chalcopyrite structure, as depicted in Figure 1.3. In and Ga atoms stay on the same lattice sites and are interchangeable. The lattice parameter c / a ratio is roughly around 2.

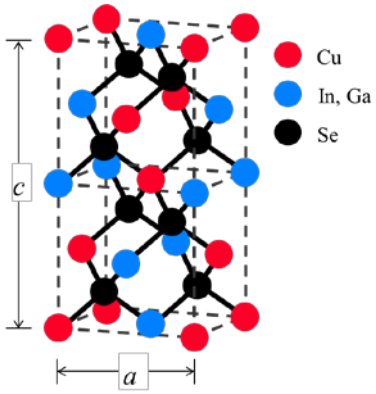

Figure 1.3: The chalcopyrite lattice structure of CIGS.

$Cu(In,Ga)Se_2$ is capable of accommodating large variations in compositions without appreciable difference in optoelectronic properties [17]. Solar cells of good performance can be fabricated with Cu / (In+Ga) ratio (or I / III ratio) from 0.7 to nearly 1.0 [17]. Cu / (In+Ga) ratio >1 will form the Cu_xSe phase and cause shunting problems of the device. The nature of the Cu deficiency of the CIGS films leads to the formation of the ordered defect compounds (ODC phases) like $CuIn_3Se_5$, $CuIn_5Se_8$ as well as Cu vacancies V_{Cu} at the film surface [18], which turns out to be beneficial to the device performance as shown in Figure 1.2. The valence band bending near the junction interface due to Cu vacancies creates a barrier for the hole transport and therefore reduces the recombination current [12].

The Ga / (Ga+In) ratio (or Ga / III ratio) in the compound affects the lattice parameters and more importantly, the bandgap (E_g) of CIGS. The Ga / III ratio can be varied from 0 to 1, accompanied by the E_g ranging from 1.035 eV ($CuInSe_2$) to 1.68 eV ($CuGaSe_2$). The composition dependence of the E_g values can be expressed by the following equation [19]:

$$E_g = 1.04 + 0.65x - 0.26x(1 - x) \quad (1.3)$$

Here x stands for the Ga / (Ga+In) ratio. More Ga incorporation into CIGS provides a wider E_g value and therefore enhanced open circuit voltage V_{oc} but reduced short circuit current J_{sc} of the device as a trade-off. The optimal device performance is usually obtained with the Ga / III ratio around 0.3 – 0.4, corresponding to the CIGS E_g about 1.18 eV to 1.24 eV.

CIGS is called the absorber layer in the solar devices since it's where the sunlight spectrum gets absorbed and electron-hole pairs are created. CIGS is a direct bandgap material. The absorption coefficient α of CIGS is higher than $3*10^4$ / cm for photon energies ($h\nu$) larger than 1.3 eV [19]. The high absorption coefficient means that 95% of the solar illumination with the photon energy above the E_g can be absorbed within the first 1 μm of CIGS film, while for crystalline Si it needs more than 100 μm thickness to absorb that much solar energy. The comparison is clearly depicted in Figure 1.4. This is one of the reasons why CIGS is a promising cost-effective photovoltaic material. In the real manufacturing environment the thickness of CIGS layer is usually around 1.5 - 2 μm.

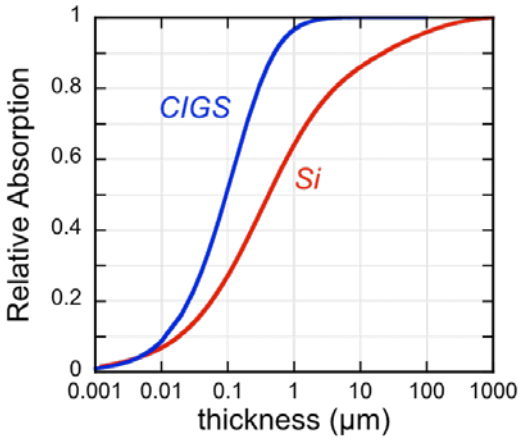

Figure 1.4: The total fraction of photons with $h\nu > E_g$ in the AM1.5 solar spectrum absorbed in CIGS as a function of film thickness, compared to the crystalline Si [7].

The device-quality CIGS film is a polycrystalline system, as seen from the cross section SEM image in Figure 1.5 [7], where the CIGS is grown on the Mo back contact. The grain size is usually on the order of 1 μm or even through the film thickness, varying a lot depending on the growth methods and conditions. A great amount of grain boundaries and structural defects including voids, dislocations, stacking faults have been observed in the chalcopyrite system, however, the CIGS solar cells seem insensitive to those imperfections and still produce over 20% efficiencies routinely. Unlike the case with crystalline Si, no significant recombination loss has been found at the grain boundaries [20], making CIGS a remarkably forgiving material.

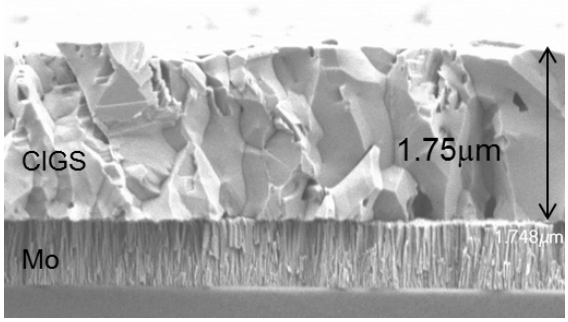

Figure 1.5: The cross-section SEM image of CIGS grown on Mo back contact [7].

There are also a variety of intrinsic defects present in the CIGS material system confirmed from the photoluminescence measurements. Some of those are native p type dopants of CIGS [18]. The minority carrier density of the CIGS absorber is on the order of $10^{15} – 10^{16}$ /cm^3 [21] and the electron mobility from capacitance-based measurements is about 5 – 20 cm^2/Vs [22].

1.2.2 Effects of Sodium

The presence of sodium in the CIGS-based absorbers plays a critical role in achieving high efficiency devices. Although a definitive picture of the working mechanism of sodium is still lacking, it's well accepted that sodium is involved in the passivation of defect states at the CIGS film surface and along the grain boundaries, which reduces the recombination current and leads to V_{oc} improvements [7, 23]. Na also helps to increase the free carrier density in the bulk absorber layer [24]. The SLG substrates commonly used for CIGS solar cells are a good source of sodium. During the high temperature growth of the absorber layer, sodium from SLG diffuses through the Mo back contact and into the bulk of the absorber layer. Sodium can also be added

intentionally during the absorber layer deposition depending on the specific experimental needs.

1.2.3 Effects of Ag Alloying

Based on Shockley-Queisser calculations [25], the optimal bandgap value of the absorber layer should be around 1.35 eV for the maximized utilization of the solar spectrum. Aluminum alloying with $CuInSe_2$ to form $Cu(In,Al)Se_2$ [26] and sulfur incorporation into CIGS to form $Cu(In,Ga)(Se,S)_2$ [27] have been reported to increase the bandgap of CIGS-based materials. The incorporation of more Ga into the CIGS material system is certainly another way to widen the bandgap, but the device efficiencies have been demonstrated not to vary linearly [28] as a function of E_g. One proposed reason is that a defect band at 0.8 eV above the valence band moves close to the midgap and becomes a more efficient recombination center as the Ga / (Ga+In) ratio increases [29].

It's been found that Ag alloying with CIGS to form the $(Ag,Cu)(In,Ga)Se_2$ (ACIGS) compound is another effective approach to obtain the wider bandgap absorbers [30]. As the Group I element, Ag replaces some of Cu atoms in the chalcopyrite system. Ag alloying lowers the melting temperature of the compound and therefore reduces the structural defect densities of the absorber layer [31]. Detailed material characterizations of ACIGS can be found in [30]. An ACIGS device with 19.9% efficiency has been demonstrated in our lab [32].

1.3 Buffer Layer

1.3.1 Selection Criteria

Historically, the introduction of a thin buffer layer – CdS – into $Cu(In,Ga)Se_2$-based chalcopyrite thin film solar cells was a significant step in the development of higher efficiency [33]. The buffer layer is an n-type material to form the p-n junction of the photovoltaic devices. $Cu(In,Ga)Se_2$ cells with a CdS buffer layer have shown the best and most reliable performance, and the basic configuration of typical $Cu(In,Ga)Se_2$ devices has not changed much since then.

Formation of the hetero-junction between the p-type CIGS absorber and the n-type buffer layer is of critical significance to the device performance. There are several important criteria that need to be considered when selecting a suitable buffer material:

1. Wide bandgap (E_g). The sunlight illuminates through the window layer side as shown in Figure 1.1. It should be mainly absorbed in the bulk CIGS where the electron-hole pairs are generated and contribute to the photocurrent. Hence the E_g of the buffer layer is should be wide enough to avoid undesirable absorption of the solar spectrum. The normally used ITO window layer in the CIGS devices has E_g over 3.3 eV. Ideally the buffer material should be of similar value to allow the short wavelength light to reach the CIGS absorber.

2. Suitable conduction band alignment. The conduction band alignment at the absorber / buffer interface is critical to the minority carrier transport. According to Anderson's model [34], the conduction band offset (CBO) can be estimated by $CBO = \chi_{absorber} - \chi_{buffer}$, where $\chi_{absorber}$ and χ_{buffer} are the electron affinities of the materials. For CIGS with baseline composition ($Cu/(In+Ga) \sim 0.9$, $Ga/(In+Ga) \sim 0.3$), the electron affinity is reported to be 4.5 eV [35]. If the conduction band minimum of the buffer is below that of the absorber at the junction interface, CBO is negative and a cliff structure forms as seen in Figure 1.6 (a). In this case the electron – hole recombination current will increase dramatically which limits the V_{oc} performance of the solar cells [36]. If the conduction band minimum of the buffer is well above that of the

absorber, CBO is positive as seen in Figure 1.6 (b) and a huge spike structure forms at the interface. The electron transport from CIGS to the n side buffer will be severely blocked. The J_{sc} and efficiency of the device will then drop sharply [36]. However, if CBO is less than 0.5 eV, the small spike will not become the carrier collection barrier since the electrons can be assisted by the thermionic energy to overcome the small spike [37]. Therefore, the preferred CBO range between the buffer and the absorber is 0 eV – 0.5 eV.

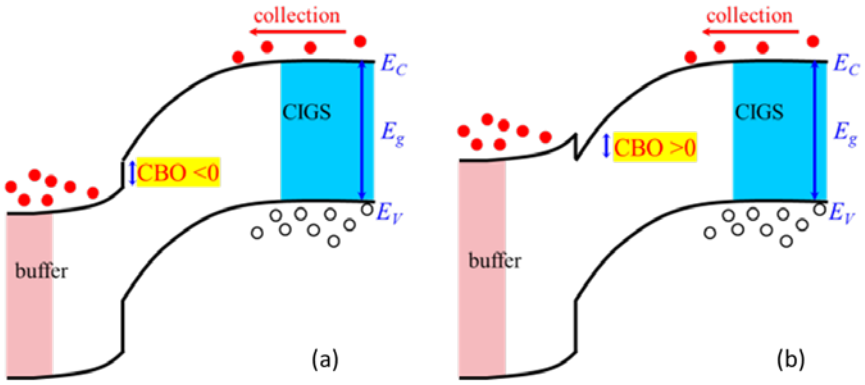

Figure 1.6: (a) Band diagram of the CIGS / buffer heterojunction with the cliff structure of the conduction band alignment (CBO < 0). (b) Band diagram of the CIGS / buffer heterojunction with the spike structure of the conduction band alignment (CBO > 0).

3. Other parameters that could have minor influence on the cell performance include the lattice parameter mismatch and thermal expansion coefficient match between the buffer layer and the absorber layer.

Above mentioned are the general criteria for the buffer materials in the commonly used substrate device configuration. For the innovative CIGS superstrate configuration, there are extra requirements that need to be considered. The thermal and chemical stability of the n-type buffer material is of the greatest importance. The inter-diffusion and chemical reactions are more likely to occur at the interface here

than in the substrate structure, since the CIGS absorber is deposited onto the SLG / window layer / buffer stack at a high temperature, usually around 550 °C. Chemical reactions and inter-diffusion between the buffer and the absorber can lead to interface defects, doping of the absorber and formation of undesirable phases, all of which can be detrimental to the device performance.

An ideal material would fulfill all of the selection criteria but it is challenging to find a material with all of the required properties. Yet several materials have sufficiently desirable properties and could be applied in CIGS solar cells as the promising buffer candidates. Table 1.1 compares the basic properties of several buffer candidate materials with CdS. The possible thermal reaction pathways in the superstrate configuration are also proposed. Detailed discussions will be presented in Chapter 5.

Table 1.1: Properties of candidate buffer materials.

Material	E_g (eV)	Electron affinity (eV)	CBO (eV)	Most likely reaction (in superstrate structure)	ΔG[38] (kJ/mol)
CdS	2.4 [39]	4.2 [39]	0.3	Ga_2Se_3+CdS--> Ga_2S_3+CdSe	-73.4
ZnO	3.3 [39]	4.6 [40]	-0.1	3ZnO+Ga_2Se_3 --> 3ZnSe + Ga_2O_3	-147.5
ZnS	3.8 [41]	3.9 [42]	0.6	3ZnS+Ga_2Se_3 --> 3ZnSe + Ga_2S_3	-21.8
ZnSe	2.7 [41]	4.1 [42]	0.4	ZnSe + 2 Cu --> Zn+Cu_2Se	72.7
In_2S_3	2.7 [43]	?	?	In_2S_3 + Cu_2Se --> 2CuIn$(S,Se)_2$	?

1.3.2 CdS Buffer Layer

CdS deposited via chemical bath deposition (CBD) has been the most widely used buffer option in CIGS-based thin film photovoltaic devices. It still produces some of the highest-efficiency lab-scale and module-scale devices, and CBD proves to be a

robust and reproducible process. The CBO between CdS and CIGS is reported to be 0.3 eV [44], falling into the optimal CBO range for the well-behaved solar devices. Besides the preferred electronic band alignment, it's proposed that the Cd doping of the absorber during the chemical bath process helps to invert the surface CIGS into a n^+ layer and achieve the favorable conduction band downward bending at the interface, which is beneficial for the photoelectron collection [45]. There have been a few investigations on the CdS depositions by 'dry' methods, e. g., sputtering or PVD, but the device performance cannot compete with the CBD-CdS, with the efficiencies usually below 10% [46, 47].

However the drawbacks of CdS can't be ignored. The parasitic light absorption in the CdS buffer layer accounts for approximately 2 mA/cm^2 loss in short circuit current of the device if the typical 50 nm thickness is applied since the E_g of CdS is only 2.4 eV [48]. The proper handling of the large amount of toxic chemical bath waste can be a massive and expensive task. What's more, the regulations on cadmium usage are getting stricter around the world primarily due to its toxicity and environmental impacts.

1.3.3 Alternative Buffer Layers

Because of the disadvantages of the CdS buffer, the search for environment-friendly alternative buffer layers with a wider bandgap continues. A wide variety of Cd-free buffer candidate materials deposited by various approaches have demonstrated excellent device results. The primary focus is on Zn- and In- compounds, including $Zn_{1-x}Mg_xO$ by magnetron co-sputtering [49, 50], Zn(S,O,OH) by CBD [51-53] or atomic layer deposition (ALD) [54] or molecular beam epitaxy (MBE) [55] or magnetron sputtering [56], Zn(Se,O,OH) by CBD [57, 58] or metal organic chemical

vapor deposition (MOCVD) [59] or ALD [60], In_2S_3 by atomic layer chemical vapor deposition (ALCVD) [61] or spray-ion layer gas reaction (ILGAR) [62] or physical vapor deposition (PVD) [63, 64] or ultrasonic spray pyrolysis (USP) [65].

Above mentioned work has shown the great promise of the Cd-free buffer materials. The mainstream buffer layer growth approach is still the chemical bath deposition, but more and more efforts have been dedicated to the 'dry' methods that are more applicable and convenient to the large-scale manufacturing environment, including sputtering, PVD and so on.

ZnSe is one of the promising alternative buffer candidates. Compared to CdS, ZnSe has a wider bandgap of 2.7eV [66], which leads to less absorption loss in the buffer. Due to the complicated nature of the interface properties and measurement approach limitations, the accurate conduction band offset between ZnSe and $Cu(InGa)Se_2$-based absorber layer is experimentally difficult to determine, but it's well accepted that a large spike type (> 0.5 eV) of CBO tends to form [67]. Two approaches are proposed in this work to modify the conduction band alignment of the CIGS / ZnSe junction. One method focuses on the absorber layer bandgap engineering, the other focuses on the buffer layer band structure modification via oxygen incorporation by means of RF reactive sputtering. Compared to CBD [58] or MOCVD [59], sputtering deposition is more applicable to the manufacturing productions.

Among the various Cd-free buffer options, Zn(S,O)-based material has been the most successful one. The main problem of using binary ZnS as the alternative buffer in CIGS devices is the electron affinity mismatch, which will create a huge conduction band spike ≥ 0.6 eV at the absorber / buffer junction interface and block the minority carrier transport [36]. It's been reported that by alloying ZnS with ZnO

to form the intermediate compound Zn(S,O), the conduction band position can be modified [68] to achieve a desired band alignment with the absorber layer. Chemical bath deposition is one way to produce the intermediate compound Zn(S,O). CBD-Zn(S,O) buffer has always been producing outstanding device performance [51-53], and finally achieves the world record CIGS-based solar cell recently with 22.3% efficiency [69]. Besides that, over 18% CIGS / Zn(S,O) devices with the buffer deposited by magnetron sputtering have been reported recently [56], further demonstrating its great potentials as the alternative buffer material in the CIGS solar industry for large-scale manufacturing production.

1.4 Thesis Statement

This dissertation proposes that: 1. the toxic CdS in CIGS-based photovoltaic devices can be replaced by environmentally friendly alternative buffer materials; and 2. Radio frequency magnetron sputtering can replace chemical bath deposition as the buffer layer deposition approach with benefits for large - scale industrial manufacturing. $ZnSe_{1-x}O_x$ and Zn(S,O) compounds are chosen as the primary investigation candidates. The material characterizations of the Zn-compounds are conducted, and the applications in both substrate and superstrate CIGS-based devices are investigated.

Chapter 2 gives the detailed information about the relevant thin film deposition techniques, the material characterization metrologies and the device analysis techniques applied in this work.

Chapter 3 provides the comprehensive study of the $ZnSe_{1-x}O_x$ compound prepared by reactive sputtering. The $ZnSe_{1-x}O_x$ compound composition is varied by controlling the $O_2/(O_2+Ar)$ ratio of the sputtering working gas. Material property

changes with the $ZnSe_{1-x}O_x$ composition changes that arise due to process variations in a reactive sputtering approach will be analyzed in detail. The application of the $ZnSe_{1-x}O_x$ alternative buffer in CIGS-based solar devices will then be discussed.

Chapter 4 focuses on the investigations of Zn(S,O) buffer material. The Zn(S,O) films are deposited by magnetron sputtering of a compound target $ZnS_{0.3}O_{0.7}$. The structural, compositional and optical properties of the sputtered Zn(S,O) films are studied by various material characterization techniques. The discussions of the applications of Zn(S,O) buffer in CIGS-based solar cells include the use of CIGS and ACIGS absorbers, the influence of the absorber surface treatments, the effects of post-device treatments, the sputtering damage and the sodium concentration in the absorber.

Chapter 5 talks about the buffer layer development in the framework of the innovative superstrate CIGS configuration. The essential components of this chapter are the absorber / buffer interface characterizations and superstrate device behavior analysis. The potentials and limitations of three buffer layer options – CdS, ZnO and ZnSe are studied. The specific problems of the superstrate device behaviors are identified and compared. In-depth interface characterizations are used to investigate the root causes that limit the device efficiencies.

Chapter 2

EXPERIMENTAL METHODS

2.1 Thin Film Deposition

2.1.1 RF Magnetron Sputtering of Zn-Compound

2.1.1.1 Sputtering Technique

The sputtering process is considered as an environmentally friendly material engineering technology. In recent years, the progress in the study and understanding of the plasma physics has led to the wide application of sputtering in the semiconductor industry as a key approach for thin film depositions. In this work, RF magnetron sputtering is employed for Zn – compound alternative buffer layer depositions.

As depicted in Figure 2.1, a standard sputtering system is composed of a pair of parallel electrodes. The target material is placed on the cathode and the cooling water circulates beneath. The cathode is connected to the power supply and negatively biased. Sample substrates are located on the anode which is usually grounded. The thermal heater can be installed near the anode for the cases where high temperature growth is needed during the film sputtering. Inert gas like Ar is usually chosen as the sputtering working gas. The glow discharge is initiated and sustained by the ionization of Ar atoms in the electric field between the electrodes. The Ar^+ ions are accelerated towards the cathode by the electric field and strike the target. The target atoms are then ejected by the energetic Ar^+ ion bombardment. The sputtered atoms traverse

through the plasma region and land onto the substrates to form the desired thin films. A plasma environment, active electrodes that participate in the deposition process, and low – temperature processing are distinct features of the sputtering technology [70].

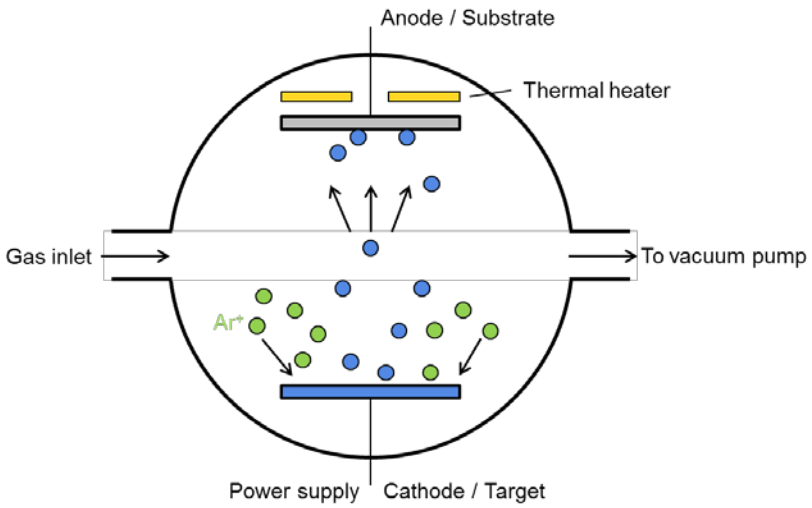

Figure 2.1: The schematic of the sputtering system.

Due to its relatively simple system setup and high deposition rate, DC sputtering is widely used for metal alloy targets which consist of conductive materials. However, if insulator targets are used, Ar^+ positive ions will build up immediately near the target cathode, which keeps the glow discharge from sustaining [71]. This problem can be solved by substituting the DC power supply with the RF (AC) power supply. Therefore, RF sputtering is often used for high resistance target materials. An impedance – matching network is included in the RF sputtering system setup. The electrodes can be viewed as a dielectric capacitor and the impedance of the capacitor

drops with increasing frequency. Thus the glow discharge can be sustained [70]. The frequency used in the RF sputtering system is usually 13.56 MHz.

The sputtering system is further optimized by the superimposition of the magnetron field with the electric field. In the magnetron sputtering system, permanent magnets are installed at the cathode in a way that the magnetic field is perpendicular to the electric field between the electrodes. Due to the Lorentz force, electrons are trapped and forced to move in a cycloidal hopping orbit. This significantly enhances the probability of electron - gas collisions and the gas ionization efficiency, which then results in more cathode sputtering and the increased film growth rate. The working gas pressure needed to sustain a stable glow discharge can also be lowered because of the confined electron movements in the magnetic – electric field. This again helps to increase the deposition rate since the collisions and scatterings between the sputtered particles and gas phase are reduced, and the sputtered – species flux is more directional to the anode substrates [70]. The targets used in the magnetron sputtering are usually found to have a circular erosion pattern or a 'racetrack' ditch. Figure 2.2 gives one example of a ZnO target with such racetrack pattern. The non-uniform plasma sputtering of the targets is a typical feature of the magnetron sputtering system. Owing to the confined electron motions, the gas ionization and the plasma are most intense above the racetrack. A circular glow discharge is often observed and leads to the preferential sputtering along the racetrack. The non-uniform sputtering shortens the target life time and results in the waste of materials. This problem can be lessened by the application of swept – field magnetrons where the permanent magnets installed near the cathode target are mechanically moved, so are the confined electron movements and the glow discharge region [70].

Figure 2.2: A ZnO target used in the magnetron sputtering system showing the typical racetrack erosion pattern.

Reactive sputtering is achieved when a reactive gas is introduced into the inert gas (Ar) and the gas mixture is used as the sputtering working gas. The resulting sputtered films are thus target materials ‘doped’ with the reactive element from the working gas mixture. For instance, oxide or nitride films can be fabricated by sputtering metallic targets in O_2 / Ar or N_2 / Ar gas environments. Compared to the direct sputtering from a compound target in pure Ar for substrate films with a fixed composition, reactive sputtering is more versatile and adjustable. The partial pressure and gas flow rate of the reactive gas components provide more possibilities to vary the compositions and properties of the sputtered thin films. During the reactive sputtering, the reactions to form the compounds take place near both of the electrodes; therefore the compound deposition is expected at the anode substrate as well as the cathode target. The compound formed on the target surface is then sputtered again by ion bombardment with usually different sputter yield and sputter rate. Conditioning of the

cathode target in pure Ar can help to restore the original target surface status in this case [71].

The sputtering system used in this work is shown in Figure 2.3. It is a cryo-pumped high vacuum thin film deposition system. One circular TORUS magnetron sputter source from Kurt J. Lesker is installed inside the deposition chamber with cooling water circulation. The size of the sputter target is 4" in diameter. A rotational sample tray is located 8.5 cm above the sputter source. Four substrate holders can be loaded at a time, and each holder has four spots for 1"x1" samples. A substrate heater is installed above the sample tray and up to 550 °C heating of the substrates can be achieved. An MKS gas low controller is used to control the sputtering gas flow rate. The chamber pressure is maintained at around 4 x 10^{-6} Torr before initiating the plasma and can be varied from 5 mTorr to 50 mTorr during the sputtering process.

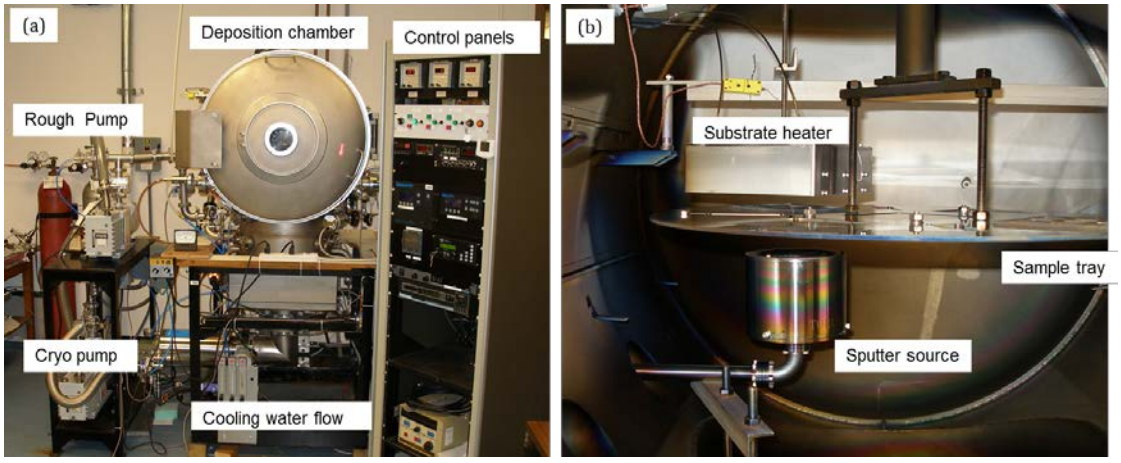

Figure 2.3: (a) Front view of the sputter system. (b) Inside view of the deposition chamber.

2.1.1.2 Sputtering of Zn-Compounds

Reactive RF magnetron sputtering was employed for $ZnSe_{1-x}O_x$ depositions. $ZnSe_{1-x}O_x$ films were deposited onto SLG and Si wafer substrates for the purpose of material characterizations and onto SLG / Mo / CIGS for device preparations. ZnSe was used as the cathode target. Ar and O_2 were chosen as the sputtering working gas. The total gas flow was maintained at 30 sccm. The O_2 content of the sputtering gas mixture (O%) was changed in order to vary the oxygen content of $ZnSe_{1-x}O_x$ films. A series of samples were prepared in different oxygen - content environments: O% = 0% - 1.4% with a step size of 0.1% for detailed investigations. The sputtering power density was 1.48 W/cm^2 and the sputtering pressure was kept at 10 mTorr. No intentional substrate heating was applied in this case. The film thickness was determined by a Dektak mechanical step profilometer. The desired thickness was obtained by adjusting the deposition time.

Zn(S,O) films were deposited in the same sputtering system. In this case, a Zn(S,O) compound target was purchased from Process Materials Inc. with 70 at% ZnO and 30 at% ZnS powder mixture. The sputtering conditions were similar to that of $ZnSe_{1-x}O_x$ films except that no reactive sputtering was carried out and only pure Ar was used as the working gas. The substrate heating during sputtering was applied to study the dependence of materials properties on growth temperature. The investigation range was from room temperature up to 200 °C.

2.1.2 Physical Vapor Deposition of CIGS

Physical vapor deposition (PVD) is used for the CIGS absorber growth in this study. It is a thermal co-evaporation process where the Cu, In, Ga, and Se elemental sources are placed in Knudsen effusion cells and delivered simultaneously to the

substrates by resistive heating [72]. Figure 2.4 (a) gives an illustration of the lab – scale evaporation system, and Figure 2.4 (b) shows the inside view of the evaporation chamber. The substrates are loaded above the elemental sources. The angles of the source bottles are adjusted to point to the center of the substrate holder. Depending on the system design and the elemental fluxes needed, the metal sources (Cu, In, Ga) are typically heated over 1000 °C and the Se source temperature is around 350 °C. The substrates loaded are usually Mo / SLG and heated to the range of 350 °C – 550 °C. Thermocouples are inserted to monitor and control the substrate temperature profiles. High temperature around 550 °C is needed for the proper growth of CIGS absorbers with good qualities and high crystallinities. However, in some cases the substrate temperature is lowered intentionally to reduce the thermal load to the substrate stack materials especially in the superstrate device configuration.

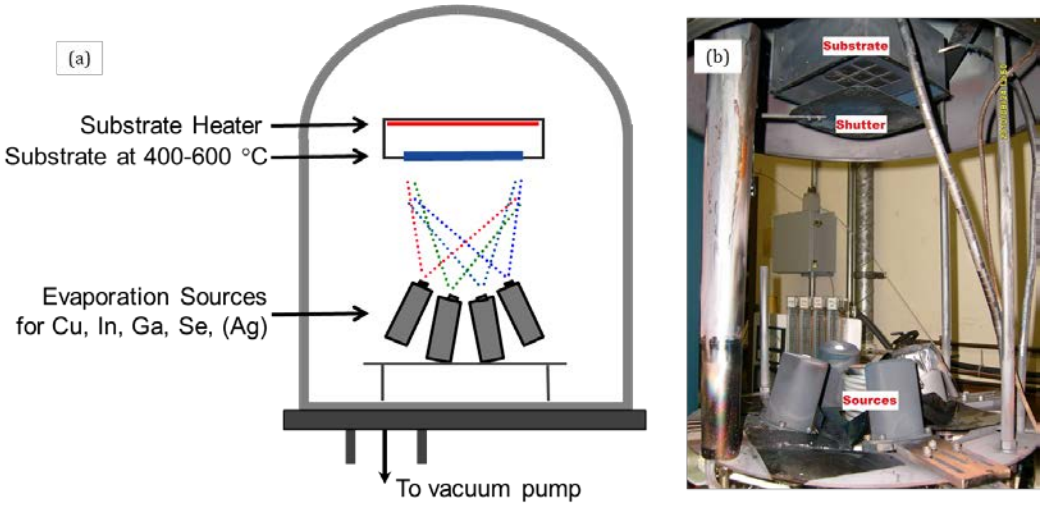

Figure 2.4: (a) The illustration of a laboratory evaporation system for CIGS productions. (b) Inside view of the evaporation chamber.

The absorber composition variations and the film growth rate are determined by the elemental fluxes and effusion rates, which are directly controlled by the source bottle temperatures. The absorbers are Cu – poor with Cu / (In+ Ga) ratio about 0.8 – 0.9 since Cu-rich will cause the shunting of the solar devices [73]. The Ga / (In+Ga) ratio is around 0.3 – 0.4 (corresponding to E_g = 1.18 eV – 1.24 eV based on Chapter 1 section 1.2.1) for the baseline process and can be varied by adjusting the relevant source bottle temperatures. The baseline film thickness is about 2 μm.

Based on the elemental flux sequences and source bottle temperature profiles, there are two primary co – evaporation processes. Both have produced CIGS films with high qualities and excellent device performance in our lab. The first one is single – stage process in which all fluxes are constant throughout the deposition [74]. The elemental constituents are evaporated simultaneously to the substrates for CIGS growth. The composition distribution along the film thickness is expected to be no variations. This is the simplest co – evaporation process. But it usually takes several test runs to establish a reproducible process with target film compositions due to the flux fluctuations and the lack of control during the evaporation course.

Most of the highest efficiency CIGS devices worldwide are fabricated with the other co – evaporation process – three – stage process in which Group I and Group III elemental fluxes are separated [74]. Sufficient Se flux is provided during the entire process. The first stage starts with the In and Ga evaporation to form $(In, Ga)_2Se_3$ compound and determines the final film thickness. Cu evaporates in the second stage and diffuses into $(In, Ga)_2Se_3$ to form CIGS until the film composition reaches the stoichiometry point (Cu / (In+Ga) = 1). After that, Cu_xSe compound forms on the surface and changes the film emissivity, which can be immediately picked up by the

substrate thermal couple monitor (End Point Detection) [75]. The Cu_xSe secondary phase formation has been reported to benefit the CIGS grain growth [76] but no conclusive answer has been reached yet about its function on the improvements of device performance [77]. The second stage produces Cu – rich films with Cu / (In+Ga) ratio = 1 – 1.1. The third stage is again In and Ga evaporations to bring the films back to Cu – poor status. The final Cu – poor composition can be guaranteed by the End Point Detection approach. Due to the different elemental diffusivity and flux sequences, composition gradients are present in the three-stage CIGS films with a Ga notch in the bulk of the film and increasing Ga / (In+Ga) ratios towards the front and back surfaces [78]. Composition gradients lead to the bandgap variations, which proves to closely relate to the device performance [79]. Three – stage is more complicated than single – stage deposition, but it is a better controlled and more reproducible process. It also provides more knobs to tune the absorber properties.

A Ag source has also been installed in the evaporation system for the production of ACIGS absorbers [80]. Ag evaporation temperature profile follows that of Cu, and the baseline Ag / (Ag + Cu) ratio is around 0.2. The effusion rate is again adjusted by controlling the source bottle temperature.

2.2 Material Characterizations

2.2.1 Structural Characterization

Thin film structural properties were characterized by symmetric X-ray diffraction (XRD) in a θ - 2θ geometry with a Philips / Norelco wide angle goniometer. The X-ray source was Cu Kα radiation with a wavelength of 0.15418 nm. The X-ray incident beam was produced by the high energy electron bombardment of the Cu

target and irradiated the sample with an angle θ to the surface. The diffracted X-ray beam was collected by the detector with a 2θ angle to the incoming beam. Due to the θ - 2θ geometry setup, the diffraction patterns were mostly contributed from the lattice planes in parallel to the sample surface. The symmetric XRD usually showed the information of the bulk of the thin film samples as well as the underlying substrate. The superimposed XRD patterns sometimes made the data analysis challenging.

The grazing incidence X-ray diffraction (GIXRD) technique was also employed with a Rigaku D/Max 2200 system. The asymmetric X-ray measurements had the Cu Kα beam incoming at a fixed angle to the sample surface and only the detector moving during the scan course. In this way the resulting patterns contained the diffraction peaks from randomly oriented grains and lattice planes, since the scattering vector direction was changing with the detector rotating and not always perpendicular to the sample surface any more [81, 82]. Due to the nature of the geometry setup, GIXRD was better suited for the randomly oriented polycrystalline thin films. The X-ray beam incoming angle could be varied as needed, which led to the X-ray beam penetration depth change. Therefore, GIXRD could be a surface-sensitive technique when the small angle incidence was used and avoided the pattern interference from the substrate; it could also detect the structural property evolutions along the film thickness when different incident angles were used. The structural properties of the thin film materials are better characterized when the symmetric XRD is used in combination with the asymmetric GIXRD.

The primary techniques used to determine the material compositions were Energy Dispersive X-ray Spectroscopy (EDS) by Oxford Instruments with an AMRAY 1810 scanning electron microscope (SEM) and X-ray Fluorescence

Spectroscopy (XRF) with an Oxford Instruments X-Strata 980 X-ray fluorescence spectrometer. Both EDS and XRF technologies utilize the characteristic X-ray energies emitted by the specific elements upon irradiation to identify and quantify the species. The irradiation source of XRF is X-ray beam, while EDS uses high energy electron beam with an accelerating voltage of 20 KV.

2.2.2 Optical Characterization

The optical properties of the samples were characterized by a PerkinElmer Lambda 750 UV/Vis/NIR spectrophotometer equipped with an integrating sphere. The thin films were deposited onto SLG substrates for the transmittance and reflectance measurements in the wavelength range usually from 300 nm to 1200 nm. Based on the optical measurements, the absorption coefficient α of the thin films can be calculated by relation [83]:

$$\alpha \approx \frac{1}{d} \ln \frac{(1-R)^2}{T} \tag{2.1}$$

Where T and R stand for transmittance and reflectance, d is the film thickness determined from the Dektak profilometer or cross-section SEM measurements.

The absorption coefficient α can be expressed by the following equation: $\alpha(h\upsilon) \sim (h\upsilon - E_g)^n$ (where $h\upsilon$ is the photon energy), and n is 1/2 for direct optical transitions [83]. Thus the bandgap values of the thin film samples can be derived by linear extrapolation of $(\alpha h\upsilon)^2 \; versus \; h\upsilon$ plot to X axis.

2.2.3 Surface Characterization

The surface properties of the samples were characterized by X-ray Photoelectron Spectroscopy (XPS). The XPS system is Physical Electronics 5600 series equipped with a dual Al/Mg anode X-ray source. The measurements were taken

in ultra-high vacuum environment around 10^{-9} to 10^{-10} Torr. The X-ray source used was monochromatic Al Kα with photon energy hν = 1486.7 eV or Mg Kα with hν = 1253.6 eV. The incoming X-rays irradiate the sample and lead to the emission of photoelectrons from specific electron orbitals. The detector measures the kinetic energies of the emitted electrons. The binding energies of the electron orbitals from which the photoelectrons originate can therefore be derived based on the equation [84]:

$$B.E. = h\nu - K.E. - \phi_s \quad (2.2)$$

Where B.E. and K.E. stand for binding energy and kinetic energy, $h\nu$ is the incoming X-ray photon energy, and ϕ_s is work function of the spectrometer (known factor). Once the binding energies are determined, the atomic species can be identified, since each element has its unique electronic structure and a characteristic binding energy spectrum. The chemical state of elements can also be identified from XPS measurements. The compound formation or chemical environment change will modify the electronic structures of the elements involved, which is reflected by the binding energy shift of the orbital peak positions on the XPS spectrum. Due to the existence of atomic sub-orbitals, the spin-orbit splitting of p, d, and f levels is often observed, shown as the binding energy peak splitting on the spectrum. The binding energy peak intensities or areas can furthermore be utilized to quantitatively determine the atomic concentrations or composition ratios of the samples.

After the photoelectric event, there is an electron vacancy left in the inner atomic orbital. The ionized atom may get relaxed through the process where an electron from an outer orbital fills in the vacancy. The released energy equal to the difference between the two orbital involved can be absorbed by a second electron from an outer orbital, leading to the emission of Auger electron. The kinetic energies of

Auger electrons are independent of the primary X-ray source (Al Kα / Mg Kα). The emission process of photoelectrons and Auger electrons is shown in Figure 2.5. Auger electron peaks can also be used to identify elemental species and their chemical states. The mean free path of electrons in solid samples is small due to the energy loss from collisions or scattering, meaning that only the photoelectrons emitted from the top few atomic layers can have enough kinetic energies to escape the sample surface and be captured by the detector, which makes XPS a surface-sensitive technique.

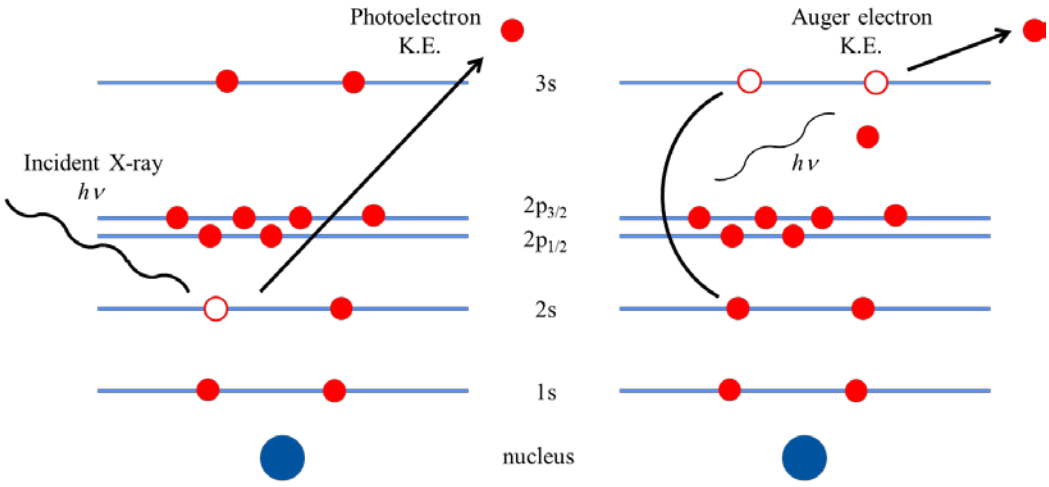

Figure 2.5: The schematic of the photoelectron emission process (left) and the Auger electron emission process (right).

2.2.4 Interface Characterization

The XPS system is equipped with an Ar ion gun for sputter-etching of the sample loaded into the vacuum chamber, which makes the system capable of doing depth profile measurements. The depth profiling of a sample was achieved by the repetition of the 'sputter-etching / XPS scan' cycle. The etching rate was about 1 nm / min calibrated for CIGS films with 3 KV voltage applied. The depth profile

measurement demonstrated the elemental distributions and chemical state change along the film thickness. It also facilitated the access to the critical interface properties of multi-layer samples. 'Soft' Ar^+ etching with only 500 V voltage applied was used in some cases to get rid of surface C-O contaminations with minimal etching, which helped to expose the real sample surface to the X-ray beam while still reserving the surface properties.

The interface properties were also characterized by high resolution transmission electron microscopy (TEM) using a JEM-2010F transmission electron microscope. The specimens were prepared by Zeiss Auriga-60 dual beam high resolution scanning electron microscope (SEM) and focused ion beam (FIB).

2.3 Device Fabrication and Analysis

2.3.1 Substrate CIGS Devices

2.3.1.1 Device Fabrication Steps

The commonly used substrate CIGS devices have the basic structure: SLG / Mo / CIGS / buffer / i-ZnO / ITO / grids as shown in Figure 1.1. The device fabrication started with Mo back contact deposition on SLG by DC sputtering with a thickness around 700 nm, followed by the multi-source co-evaporation of the absorber layer. ACIGS / CIGS absorbers and one-stage / there-stage evaporation process were used depending on the experimental requirements. Next step was the buffer layer deposition to form the heterojunction with the absorber layer. This will be described in details in section 2.3.1.2. The front window layers were high-resistance ZnO (resistivity around 1-100 Ω cm [85]) of ~50 nm and ITO layer (resistivity around 10^{-4} – 10^{-3} Ω cm [85]) of ~150 nm, both of which were deposited by magnetron sputtering.

The devices were completed with Ni/Al metal grids by electron-beam evaporation and then mechanically scribed to the defined cell area of 1 cm^2 or 0.4 cm^2.

2.3.1.2 Buffer Layer Deposition

CdS is the most commonly used buffer material and usually grown by chemical bath deposition (CBD). Figure 2.6 shows the laboratory apparatus for CBD of CdS [86]. The solution contained three main ingredients: $CdSO_4$ (0.015M), Thiourea $(NH_2)CS$ (0.75M) and ammonia to make it an alkaline environment. The beaker containing the solution was placed in a water bath and preheated to a temperature around 65 °C. The absorbers were then immersed into the solution for the CdS buffer growth. Typically 14 min growth produced a CdS layer of ~ 50 nm thickness.

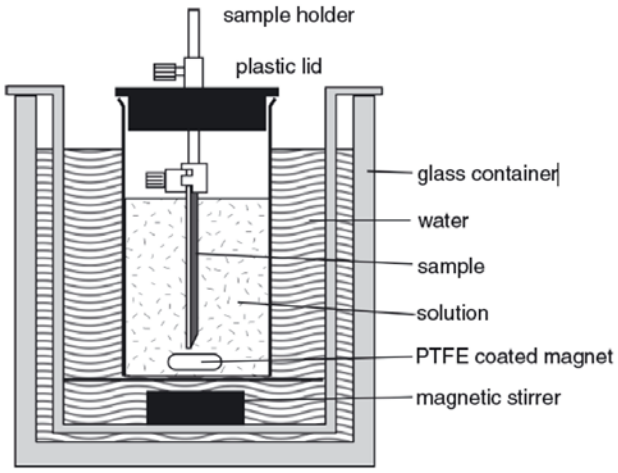

Figure 2.6: The laboratory apparatus for chemical bath deposition of CdS and wet surface treatment of the absorber surface prior to the alternative buffer Zn-compound depositions [7].

$ZnSe_{1-x}O_x$ and Zn(S,O) buffer materials were deposited by RF magnetron sputtering. $ZnSe_{1-x}O_x$ was reactively sputtered from a ZnSe target in O_2/Ar environment; Zn(S,O) was sputtered from a Zn(S,O) targets in Ar. The detailed sputtering conditions were described in section 2.1.1.2.

2.3.1.3 Wet Chemical Surface Treatment of the Absorbers

CIGS samples transferred from the absorber evaporation system to the Zn-compound sputtering system inevitably exposed the absorber surface to the air. Carbon and Oxygen related contaminants and Na compounds [23] would accumulate on the (A)CIGS surface quickly and modify the absorber / buffer interface properties significantly. Therefore various wet chemical treatments and cleaning procedures of the absorber surface prior to the Zn-compound buffer sputtering were conducted and compared as listed below:

Water rinse. The absorbers were rinsed in room temperature nano-pure water, blown dry by N_2 and then loaded into the sputtering system.

Cd^{2+} partial electrolyte (Cd PE) treatment. The solution was prepared with the same chemical molar concentration as the solution used for CBD of CdS except that no Thiourea was added. The solution was placed in a 65 °C water bath. The absorbers were immersed into the solution for 1min, then rinsed in nano-pure water, blown dry and loaded into the sputtering system.

Zn^{2+} partial electrolyte (Zn PE) treatment. The solution was prepared with $ZnSO_4$ (0.025M) and ammonia. The treatment procedure was the same as Cd PE treatment.

KCN cleaning. The KCN solution was pre-heated to 60 °C. The absorbers were immersed into the 10% KCN solution for 1min, then rinsed in nano-pure water, blown dry and loaded into the sputtering system.

The mechanism for the above mentioned absorber surface treatments will be further explained in section 4.3.3.1.

2.3.2 Superstrate CIGS Devices

Three buffer materials CdS, ZnO, and ZnSe were tested and compared in the superstrate CIGS configuration. Substrates for all samples were SLG coated with 300 nm thick ITO. Samples were then loaded into the RF magnetron sputtering system for the deposition of ZnO or ZnSe buffer layers. Chamber pressure was maintained at 10 mTorr and sputtering power density was 1.2 W/cm^2. The baseline ZnO / ZnSe layer thickness was 100 nm / 70 nm. Films were deposited with no intentional substrate heating except in a few cases where ZnO was sputtered at substrate temperature T_{sub} = 500°C for improved thermal stability. Experiments with CdS buffer were guided by the approaches that were developed for superstrate CdTe solar cells. First a 20 nm Ga_2O_3 high resistance layer was formed on the SLG / ITO by high temperature oxidation of a Ga thin film [87]. Then a 100 nm CdS layer was deposited via a chemical surface deposition (CSD) process [88]. This formed films with significantly reduced density of particulate defects on the surface which were commonly observed with a conventional chemical bath deposition due to inhomogeneous CdS growth in the bath. Some CdS films were then annealed in parallel – plate $CdCl_2$ vapor (where a plate dipped in $CdCl_2$ solution was placed above CdS films to provide the $CdCl_2$ vapor at 425°C for 10 mins [87, 89] in order to crystallize the films and increase material

thermal stability. The ITO / Ga_2O_3 / CdS structure has been utilized in high efficiency CdTe solar cells [87], demonstrating that no current blocking behavior is expected.

CIGS absorbers were then deposited on top of the buffer layers using a single stage co-evaporation process. Elemental fluxes were kept constant during deposition to avoid composition gradients. All absorbers were Cu-poor with Cu / (In+Ga) = 0.8 - 0.9 and Ga / (In+Ga) = 0.3. Baseline films were evaporated at T_{sub} = 550°C. In some cases T_{sub} was lowered in order to reduce the thermal load to the window layer stacks. Devices were completed by electron-beam evaporation of 200 nm thick Au back contacts with area = 0.4 cm^2.

2.3.3 Device Analysis

The CIGS-based thin film solar devices were primarily evaluated by current-voltage (JV) measurements under 100 mW/cm^2 AM1.5 illumination. The JV parameters – open circuit voltage (V_{oc}), short circuit current (J_{sc}), fill factor (FF) and efficiency (Eff) – were the critical indicators of the device performance and behaviors. In order to investigate the recombination mechanism that limited the V_{oc} of CIGS-based solar cells, temperature dependent V_{oc} (V_{oc} – T) [90] measurements were conducted in the range of -160 °C to 100 °C; To better understand the current collection problem in the devices, Quantum efficiency (QE) measurements were carried out in the wavelength range from 350 nm to 1200 nm; Another device analysis technique applied in this work was the capacitance – voltage (C-V) measurements. The significant information including the minority carrier densities, potential barriers and deep trap densities can be extracted from the junction capacitance behaviors [91].

Chapter 3

STUDY OF $ZnSe_{1-x}O_x$ COMPOUND AS THE ALTERNATIVE BUFFER MATERIAL

3.1 Introduction

Zn-compounds with various deposition approaches have shown potential and attracted lots of interest in photovoltaic industry. ZnSe films deposited by metal organic chemical vapor deposition (MOCVD) or chemical bath deposition (CBD) were reported as alternative buffer layers in CIGS solar cells [58, 59]. As mentioned in Chapter 1, there are several criteria that need to be considered when selecting suitable buffer candidates. Compared to CdS, ZnSe has a wider bandgap of 2.7eV [66], therefore reducing absorption loss in the buffer layer. Due to the complicated nature of the interface properties and measurement approach limitations, the accurate conduction band offset between ZnSe buffer and $Cu(InGa)Se_2$-based absorber layer is experimentally difficult to determine. Bauknecht [92] measured the valence band offset between ZnSe and $CuGaSe_2$ (001) using XPS and calculated CBO to be 0.4 ± 0.1 eV. Nelson [67] presented a theoretical prediction and an experiment - determined value of 0.7 ± 0.1 eV for the ZnSe / $CuInSe_2$ (112) conduction band offset. The deposition process for ZnSe can also affect the apparent band alignment. For instance, chemical bath deposition leads to the formation of a compound Zn(Se,O,OH) [58]. The intermixing of selenide, oxide and hydroxide modifies the energy band diagram at the interface.

In this chapter, the application of RF magnetron sputtered $ZnSe_{1-x}O_x$ as the buffer layer in CIGS solar cells is discussed. The electron affinity χ of ZnSe is lower than that of CdS (4.1 eV [93] vs. 4.5 eV [73]).Based on the Anderson rule [34], the conduction band offset between ZnSe and CIGS is likely to be larger than the preferred range and this will create an electron transport barrier as discussed in Chapter 1. We propose two ways to better tune the conduction band alignment between ZnSe and CIGS. The first one comes from the band engineering of the CIGS absorber layer. It's well known that the bandgap E_g of CIGS increases significantly with the Ga addition, from 1.035 ev for $CuInSe_2$ to 1.68 eV for $CuGaSe_2$ [19]. The correlation between the CIGS bandgap and Ga / (Ga+In) ratio has been discussed in detail in chapter 1. The CIGS E_g widening is mainly due to the conduction band minimum upward shift [94], which suggests that the conduction band offset between ZnSe and CIGS can be reduced by increasing Ga content. The composition of the CIGS layer relies on the Cu, In, Ga and Se elemental fluxes, which are controlled by the elemental source evaporation temperatures. In this study, single stage CIGS absorbers with Ga / (Ga+In) ratio = 0.3, 0.5 and 0.8 (corresponding to E_g = 1.18eV, 1.30eV, and 1.52eV) were used with RF sputtered ZnSe buffer layers. The Ga / (Ga+In) ratio was varied for the purpose of tuning the conduction band alignment between the absorber and buffer, and was achieved by adjusting the elemental source temperature profiles.

The other approach to potentially reduce the barrier height is to lower the conduction band energy position of the ZnSe layer. Adding oxygen could be an effective approach to modify the electronic band structure of ZnSe [95-97]. Models suggest that the conduction band position could be significantly reduced by oxygen

atoms creating isovalent impurity levels near the conduction band minimum (CBM) based on large scale plane-wave pseudopotential calculation [95]. This would lead to dramatic E_g narrowing – the E_g value drops to 1.8eV when x = 0.5 in $ZnSe_{1-x}O_x$ according to first - principles calculation [97]. A band anticrossing model (BAC) also attributes an oxygen - induced E_g reduction to the conduction band downward shift caused by the interaction of localized oxygen impurity states and the conduction band of the ZnSe host matrix [96]. Experimental results on the $ZnSe_{1-x}O_x$ compound system have been reported with films deposited by molecular beam epitaxy (MBE) [98-100] or pulsed laser deposition (PLD) [101]. They have shown the consistent trend of E_g reduction with oxygen incorporation as the theoretical predictions, although only a narrow range of oxygen incorporation has been obtained. In this study, rf magnetron reactive sputtering is used to prepare $ZnSe_{1-x}O_x$ films. The capability of bandgap engineering of $ZnSe_{1-x}O_x$ films expands its further applications in photovoltaic technology.

Chapter 3 first presents the device results and analysis of ZnSe / CIGS solar cells with various Ga / (Ga+In) ratios. Next the comprehensive investigations of the structural, optical and compositional properties of the reactive sputtered $ZnSe_{1-x}O_x$ compound films, and its applications in CIGS solar cells will be discussed in section 3.3.

3.2 Application of ZnSe Alternative Buffer in CIGS Devices

3.2.1 CIGS / ZnSe Device Results

Figure 3.1 shows the CIGS substrate device structure with RF magnetron sputtered ZnSe alternative buffer. For device preparation, the CIGS absorbers with

various Ga concentrations were cleaned in a 10% KCN solution for 1 min before loading for ZnSe sputtering. ZnSe was sputtered from a ZnSe target in Ar atmosphere to a thickness of around 25nm. For comparison, reference samples with the baseline CBD deposited CdS were also prepared with absorbers from the same evaporation run.

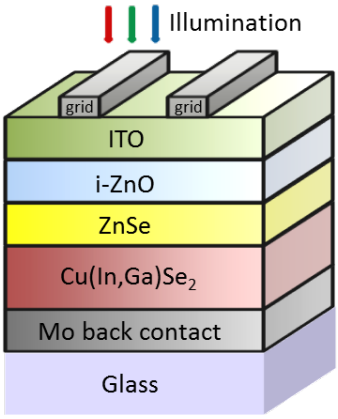

Figure 3.1: Substrate CIGS device configuration with ZnSe alternative buffer layer.

Figure 3.2 shows light JV curves of substrate CIGS devices of various Ga concentrations with sputtered ZnSe buffers. Dashed curves are reference cells with CBD-CdS buffers from the same CIGS absorber evaporation runs. The corresponding JV parameters are summarized in Table 3.1. The E_g of the absorbers are determined based upon the discussions in Section 1.2 in Chapter 1. Dark JV curves are not shown for clarity but none of the devices have significant shunt losses.

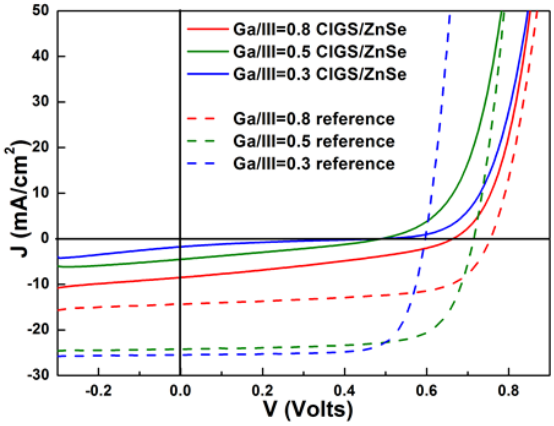

Figure 3.2: Light JV curves of CIGS devices with various Ga concentrations under AM1.5 illumination. Solid curves are substrate cells with ZnSe buffers, dashed curves are reference cells with CdS buffers.

Table 3.1: JV parameters from Figure 3.2.

Buffer	Ga/ (In+Ga)	E_g (eV)	V_{oc} (mV)	J_{sc} (mA/cm^2)	FF (%)	Eff (%)
ZnSe	0.8	1.52	664	8.5	34.4	1.9
	0.5	1.30	490	4.5	29.3	0.6
	0.3	1.18	489	1.8	17.9	0.2
CdS	0.8	1.52	775	14.4	63.5	6.9
	0.5	1.30	715	24.2	71.5	12.4
	0.3	1.18	596	25.5	74.9	11.4

For the reference cells with CdS buffer, as Ga / (In+Ga) ratio increases, the bandgap of CIGS increases leading to an increase of V_{oc} and a decrease of J_{sc} due to less photon absorption. With the ZnSe buffer, V_{oc} shows the same trend but J_{sc} increases despite the lower light absorption with wider E_g. The results suggest a spike in the CBO at the CIGS / ZnSe interface, which leads to suppressed photocurrent collections. As more Ga is incorporated into the CIGS, the conduction band minimum of the absorber shifts to higher energy [94], so the CBO is reduced and more photo-

generated minority carriers can overcome the barrier. For the lower V_{oc} compared to the reference cells, a possible cause could be the interface recombination and the lack of CdS - bath cleaning of the absorber surface [102].

3.2.2 CIGS / ZnSe Device Analysis

CIGS / ZnSe devices demonstrate voltage dependent current collection J_L (V), as shown in Figure 3.3. This contributes to the poor fill factors of the devices (Table 3.1) and is further confirmed from QE measurements. Figure 3.3 shows the case where the absorber has Ga/(In+Ga) = 0.5, the current collection is low over the whole wavelength range under 0V applied bias. Under -1V and -2V reverse bias where the junction depletion region gets widening, the current collection improves dramatically.

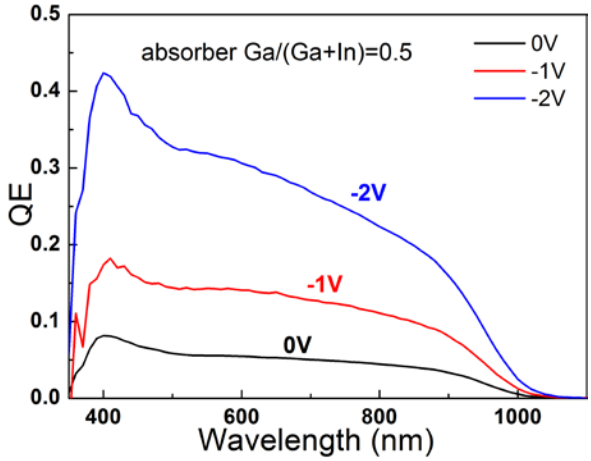

Figure 3.3: Quantum efficiency measurements of the device with Ga/(In+Ga) = 0.5 under 0V, -1V and -2V reverse bias.

To better characterize the device behavior of the CIGS cells with ZnSe buffer layers, temperature dependent JV (JVT) measurements were performed. Figure 3.4

shows the JV light curves of the device with the absorber content Ga / (In+Ga) = 0.8 measured in the temperature range from -60 °C to 130 °C. As the temperature increases, J_{sc} is enhanced as a result of greater thermal activation energies for minority carriers to overcome the barrier [7], as shown in Figure 3.5. Figure 3.6 plots the V_{oc} values measured as a function of temperature. By the linear extrapolation of V_{oc} (T) to absolute zero, the recombination activation energy E_a is derived to be around 0.81V, well below the bandgap value of the bulk CIGS (~1.5 eV for Ga / (Ga+In) = 0.8 [19]). This suggests that the interface recombination is the dominating mechanism in the CIGS / ZnSe devices [91], which leads to lower V_{oc} as seen in Table 3.1.

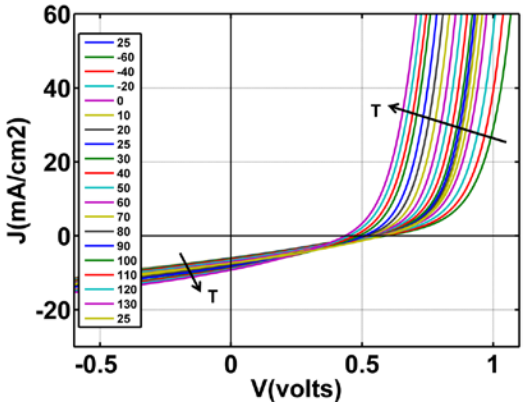

Figure 3.4: Illuminated curves of JVT measurements for the device with Ga / (Ga+In) = 0.8; Temperature ranges from -60 °C to 130 °C.

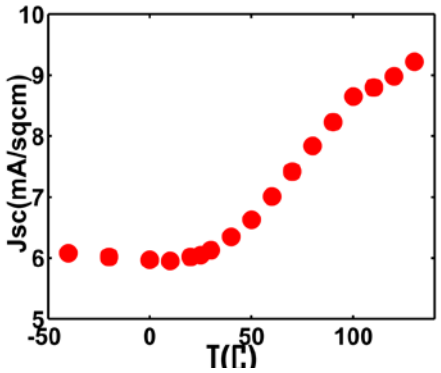

Figure 3.5: The evolution of J_{sc} vs. temperature in JVT measurements for the device with Ga / (Ga+In) = 0.8.

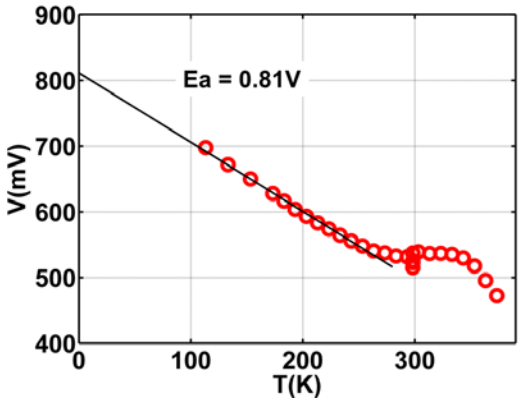

Figure 3.6: The evolution of V_{oc} vs. temperature in JVT measurements for the device with Ga / (Ga+In) = 0.8. Linear extrapolation to T = 0K shows the recombination activation energy E_a = 0.81 V.

In addition to the voltage dependent current collection J_L (V), the fill factor is reduced by a kink in the power quadrant of the JV curve. A more definitive way to detect such behavior is to plot the derivative dV / dJ against 1 / (J+ J_{sc}) [91], as shown in Figure 3.7. The dark curve (not shown here) is well-behaved with a straight line that extrapolates to the series resistance. However, the light data as shown in Figure 3.7 has a peak indicating a blocking barrier [91]. The peak is related to the kink in the

fourth quadrant of the JV curve. The point ($1 / J_{sc}$, dV_{oc} / dJ) where the device is under open circuit voltage is on the left side of the maximum peak (out of the current Y axis scale). This blocking barrier is presumably located at the ZnSe / CIGS junction, rather than CIGS / back contact since this behavior is not observed in the devices with reference CdS buffer layers and the conventional Mo back contact used here forms a non-blocking contact. The peak height in Figure 3.7 decreases at higher temperature, suggesting greater thermal activation of the minority carriers over the barrier [91].

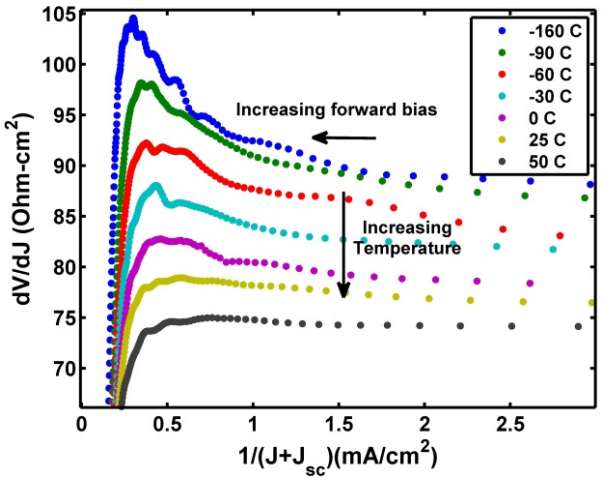

Figure 3.7: Plot of dV/dJ vs. $1/(J+J_{sc})$ in the forward bias region under different temperatures.

In summary, the first approach to modify the band alignment between ZnSe and CIGS focuses on the bandgap engineering of the absorber layer by adjusting the Ga / (Ga+In) ratio. Device analysis reveals a conduction band spike at the CIGS / ZnSe heterojunction. Use of wider bandgap absorbers has shown a reduction of the

height of this blocking barrier. However, the suppressed current transport is still the main limiting factor of the device performance.

3.3 Development of Reactive Sputtered $ZnSe_{1-x}O_x$ Compounds

3.3.1 Material Characterization of $ZnSe_{1-x}O_x$

As described in Chapter 2, section 2.1, reactive sputtering of a ZnSe target in Ar + O_2 atmosphere was employed to prepare $ZnSe_{1-x}O_x$ films. O_2 content of the sputtering gas mixture (O% = O_2 / (O_2 + Ar)) was varied from 0% - 1.4% with a step size of 0.1% for detailed investigations. The film growth rate was determined from thickness measurement by a Dektak mechanical step profilometer. The film thickness (usually around 2 μm) was varied by adjusting the deposition time.

3.3.1.1 Structural Properties

XRD measurements of the sputtered $ZnSe_{1-x}O_x$ films show zinc-blende structure with preferential growth along the (111) direction. Figure 3.8 shows the XRD full pattern of one ZnSe film sputtered in Ar (O_2 / (O_2+Ar) = 0%) with the main peaks identified. Figure 3.9 (a) compares the normalized XRD (111) peaks of seven $ZnSe_{1-x}O_x$ samples sputtered in various oxygen - content gas mixtures and the calculated lattice spacings based on Bragg's Law are plotted in Figure 3.9 (b). As the O_2 / (O_2+Ar) ratio (O%) of the sputtering gas increases, $ZnSe_{1-x}O_x$ (111) peaks shift to higher angles. The crystal lattice shrinks according to Bragg's Law with the exchange of oxygen on selenium sites since the radius of an O atom is much smaller than Se. However, the possibility that some oxygen atoms might stay on the interstitial sites or along the grain boundaries cannot be ruled out. Accompanied by the peak shift, the (111) peak broadens and the intensity drops dramatically as O% increases, as shown

clearly in the inset figure (without peak normalization) in Figure 3.9 (a). For films sputtered in O% = 1.3% and above, the signal to noise ratio of the diffraction peak is further reduced.

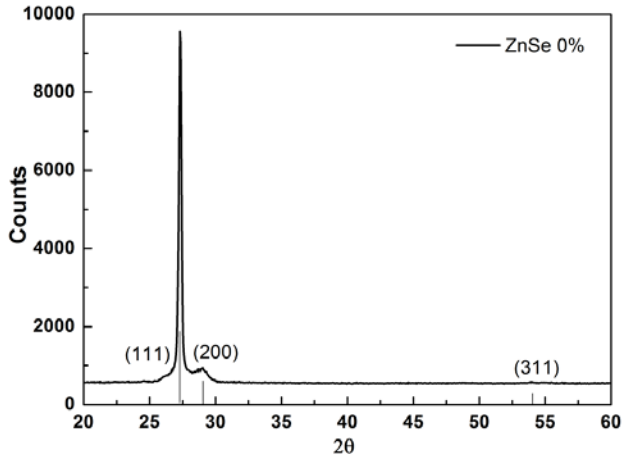

Figure 3.8: XRD full scan of the ZnSe film sputtered in Ar (O_2/O_2+Ar = 0%).

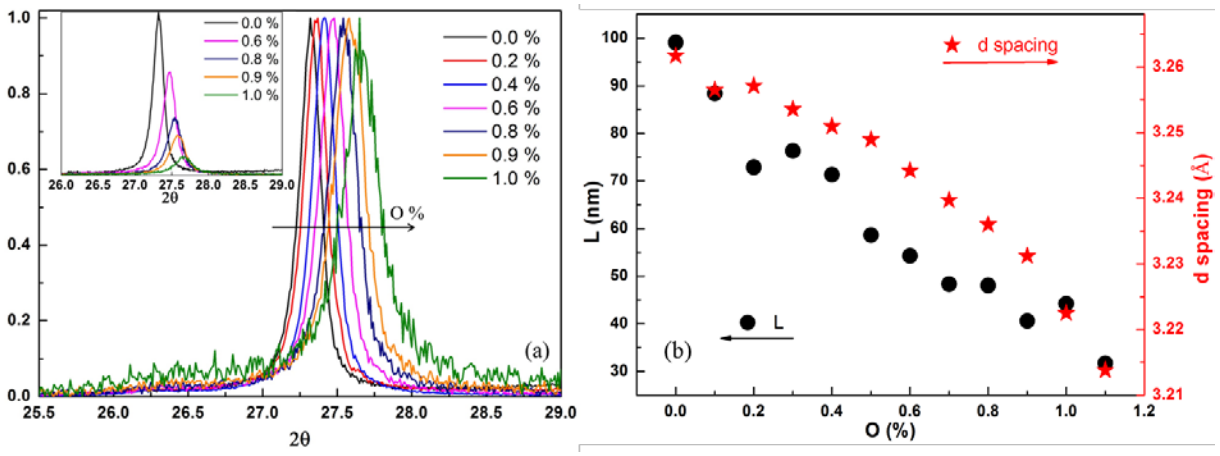

Figure 3.9: (a) XRD fine scans of the (111) peak of the $ZnSe_{1-x}O_x$ films sputtered in various oxygen – content working gas. The inset figure shows the (111) peak of the $ZnSe_{1-x}O_x$ films without normalization. (b) XRD (111) lattice spacing and the calculated coherence length of the $ZnSe_{1-x}O_x$ samples sputtered in various oxygen – content gas mixture.

The film crystallinity is evaluated by application of the Scherrer formula:

$$L = \frac{k\lambda}{\beta \cos\theta} \tag{3.1}$$

where L is the coherence length which is an indicator of the grain size; k is the shape factor and approximately equals 0.9 [103]; λ is the incident X-ray wavelength (Cu Kα = 0.15405 nm); β is the corrected full width at half maximum (FWHM) of the (111) peak ($\beta = \sqrt{{\beta_{mea}}^2 - {\beta_{ins}}^2}$, β_{mea} is the measured FWHM and β_{ins} = 0.12° is the instrument resolution); and θ is the Bragg diffraction angle. The calculated results are plotted in Figure 3.9 (b) in black dots. Decreasing apparent grain size further demonstrates the trend of the degraded crystallinity as more oxygen is incorporated into the $ZnSe_{1-x}O_x$ films.

Figure 3.10 presents the SEM plain-view (a, b, c) and cross-section (d, e, f) images of samples sputtered in O% = 0%, 0.4%, and 1% respectively. The $ZnSe_{1-x}O_x$ films show columnar growth. It's found that the $ZnSe_{1-x}O_x$ film growth rate is around 30 nm/min, independent of variations in the O% of the sputtering gas in the current investigation range. The film thickness difference observed from cross-section SEM here is mainly due to the variations of deposition time. The diminished grain size from the sample sputtered in O% = 0% to the one sputtered in O% = 1% is correlated to the oxygen incorporation into the $ZnSe_{1-x}O_x$. No grain structure can be observed from the films sputtered in O% = 1.3% and above.

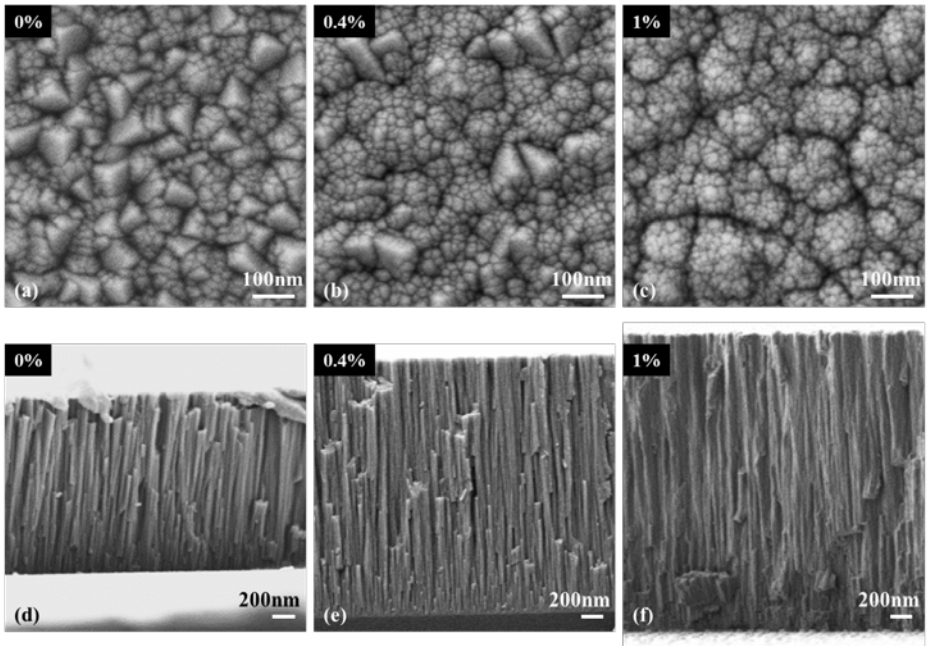

Figure 3.10: (a), (b), (c) SEM images of the $ZnSe_{1-x}O_x$ films sputtered in different oxygen – content working gas conditions. (d), (e), (f) Cross-section SEM images of the $ZnSe_{1-x}O_x$ films sputtered in different oxygen – content working gas conditions.

3.3.1.2 Optical Properties

The optical transmittance (*T*) spectra of selected $ZnSe_{1-x}O_x$ films are plotted in Figure 3.11 (a). For $ZnSe_{1-x}O_x$ sputtered in higher O% gas mixture, the transmittance onset edge shifts to longer wavelength indicating bandgap narrowing. The oxygen incorporation of $ZnSe_{1-x}O_x$, which leads to decreased crystallinity and smaller grain size as mentioned above, can introduce defect states into the forbidden band and sub-bandgap absorption tails [83]. The decreased transmittance around bandgap edge (550 nm – 700 nm) with higher oxygen concentration is due to this low energy absorption, as shown in Figure 3.11 (b) where the corrected absorption (1- $\frac{T}{1-R}$ with *R* the reflection) is plotted versus wavelength.

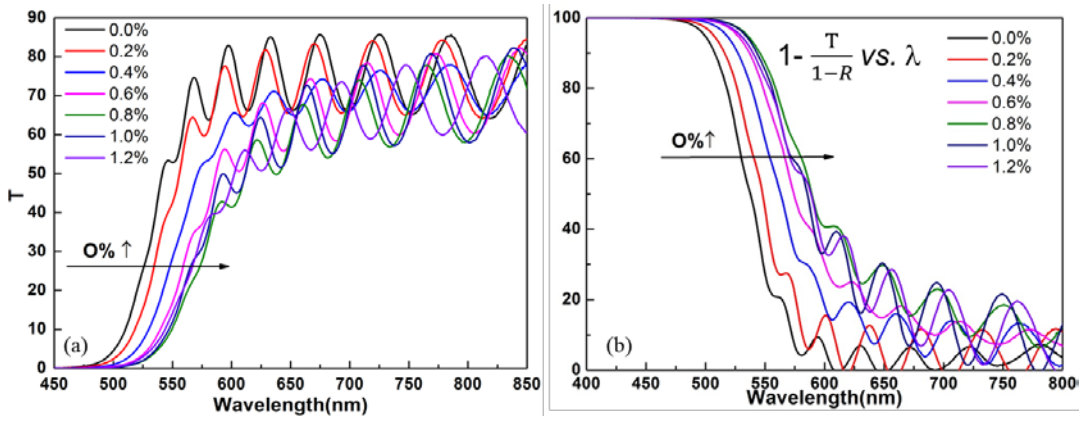

Figure 3.11: (a) Transmittance spectra of the $ZnSe_{1-x}O_x$ films sputtered in different oxygen – content working gas conditions. (b) The corrected absorption spectra (1- T / (1-R) vs. wavelength) of the $ZnSe_{1-x}O_x$ films sputtered in different oxygen – content working gas conditions.

Absorption coefficient α can be calculated by relation [83]:

$$\alpha \approx \frac{1}{d} \ln \frac{(1-R)^2}{T} \tag{3.2}$$

Where d is the film thickness determined from Dektak profilometer and cross-section SEM measurements. Absorption coefficient can be expressed by the following equation: $\alpha(h\upsilon) \sim (h\upsilon - E_g)^n$ (where $h\upsilon$ is the photon energy), and n = 1/2 for direct optical transition [83]. Thus E_g values of $ZnSe_{1-x}O_x$ can be derived by linear extrapolation of $(\alpha h\upsilon)^2$ versus $(h\upsilon)$ plot to X axis. Figure 3.12 (a) shows one example of the E_g derivation for the ZnSe film sputtered in $O_2/(O_2+Ar)$ = 0%. Nanocrystalline $ZnSe_{1-x}O_x$ films don't have well-defined band edges due to the substantial absorption tails, which makes accurate E_g determination uncertain, but the evolution of $ZnSe_{1-x}O_x$ bandgaps with increased oxygen concentration can still be obtained by this method. The E_g reduction vs. the O_2 / (O_2 + Ar) ratio of the sputtering

gas mixture is shown in Figure 3.12 (b). For the $ZnSe_{1-x}O_x$ film sputtered in 1% O_2 gas mixture, E_g decreases by about 0.2 eV compared to ZnSe sputtered in pure Ar.

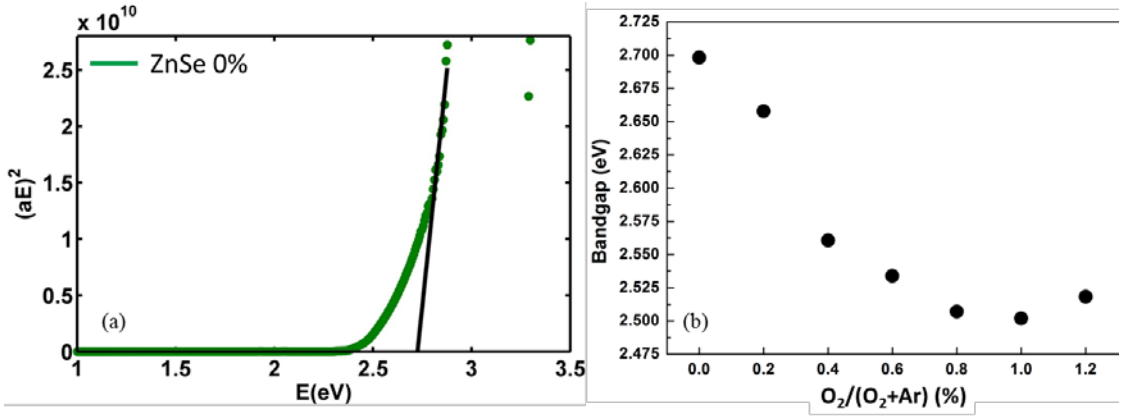

Figure 3.12: (a) E_g derivation for the ZnSe film sputtered in $O_2/(O_2+Ar)$ = 0%. (b) Derived bandgap values for $ZnSe_{1-x}O_x$ films sputtered in different oxygen – content working gas conditions.

Figure 3.13 compares the valence band spectra measured by XPS of two samples – ZnSe sputtered in Ar and $ZnSe_{1-x}O_x$ sputtered in O_2 / (O_2 + Ar) = 1%. The films were pre – cleaned by 'soft' Ar etching (500 V) for 30 mins in the XPS chamber to get rid of surface contamination. The leading edges of the valence band spectra for the two samples overlap with each other, indicating that the valence band position remains unchanged [104] with oxygen added into ZnSe. Therefore the E_g value reduction can be attributed to a lower conduction band position, consistent with previous studies [95, 96].

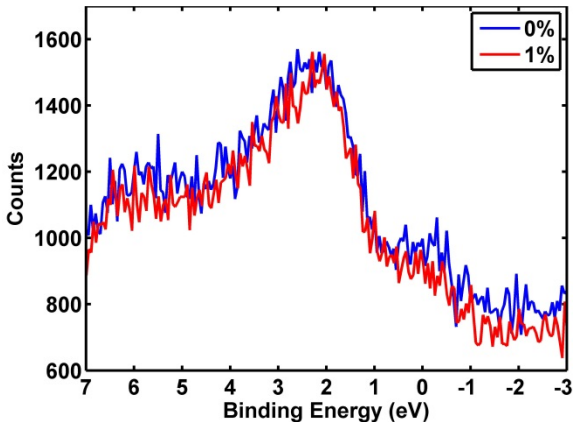

Figure 3.13: Valence band spectra from XPS measurements for samples sputtered in 0% (blue) and 1% (red) oxygen - content gas mixture.

3.3.1.3 Compositional Analysis

Determination of the oxygen concentration in $ZnSe_{1-x}O_x$ films is challenging, especially when the amount of oxygen actually incorporated is small. Multiple techniques were used here - EDS, XPS, XRD and E_g by comparison with literature [97]. For EDS measurements, $ZnSe_{1-x}O_x$ films were grown > 2 μm thick on Si wafers to avoid substrate effects and measurements were done with 20 kV electron excitation. For XPS measurements, air exposure during sample transfer was usually within one hour and necessary surface cleaning by in-situ Ar sputtering was conducted as mentioned in Chapter 2 section 2.2.4. The oxygen content (O / (O+Se) ratio) of the films was quantified using integrated XPS O 1s and Se 3d peak areas divided by atomic sensitivity factors [84]. $ZnSe_{1-x}O_x$ film lattice constants were calculated from the XRD spectra mentioned above and x value was obtained using Vegard's Law assuming zinc-blende ZnO lattice constant to be 4.47 Å [105]. By optical measurements, x values were derived based on the measured bandgap values and the reported bowing parameter b = 5.76 eV [97]. The results for x in $ZnSe_{1-x}O_x$ films vs.

O_2 / (O_2 + Ar) of the sputtering gas mixture are plotted in Figure 3.14. The higher oxygen concentrations measured from EDS and XPS suggest that a considerable amount of oxygen is not incorporated into the ZnSe host lattice but resides along the grain boundaries instead. XRD and optical measurements, on the other hand, mainly characterize the effects of oxygen incorporated into the grains, which induces the lattice parameter change. The results here reveal that the oxygen concentration in $ZnSe_{1-x}O_x$ films is very low. O / (O+Se) ratio is only about 0.06 – 0.12 for the sample sputtered in 1% oxygen - content gas mixture.

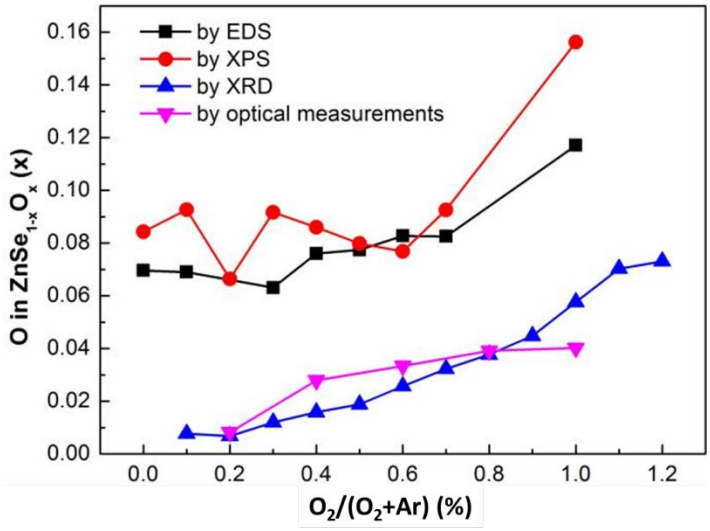

Figure 3.14: Composition measurements of the $ZnSe_{1-x}O_x$ films sputtered in various oxygen – content working gas by EDS, XPS, XRD and optical E_g comparisons with previous report.

3.3.1.4 Oxygen Solubility in ZnSe Matrix

Due to the significant atomic radius difference (O atom ~ 48 pm vs. Se atom ~ 103 pm) and the crystal structure mismatch (ZnO wurtzite structure vs. ZnSe

zincblende structure), the oxygen solubility in the ZnSe host lattice is extremely low. We are only able to achieve about 6% (by XRD and optical measurements) oxygen incorporation by reactive sputtering of the ZnSe target in 1% oxygen – content gas mixture, which induces about 0.2 eV bandgap narrowing. Further increasing the O_2 content in the sputtering gas resulted in secondary phase formation as shown by XPS measurements. Figure 3.15 are the XPS Se 3d doublet peak profiles measured on four samples sputtered in (a) 0%, (b) 1%, (c) 2% and (d) 4% oxygen - content gas mixture respectively. For these measurements, samples were taken out from the sputtering system and loaded into the XPS chamber within 30 mins. XPS fine scans started when the XPS chamber pressure returned to 10^{-9} Torr. No Ar etching cleaning of the film surface was conducted in this case. The collected XPS spectra are calibrated for charging effects with the carbon 1s peak at 285 eV. For the films grown in 0% and 1% oxygen environment, the binding energy of the Se 3d peak is around 54 eV (Figure 3.15 (a) and (b)), which is ascribed to a Zn – Se bond [84]. When the oxygen content of the sputtering gas is increased to 2%, another Se 3d peak shows up at higher binding energy around 58 eV which corresponds to the chemical state of Se in SeO_3^{2-} [106]. This Se 3d peak intensity appears much stronger in the sample sputtered in 4% oxygen, indicating a large amount of zinc selenite ($ZnSeO_3$) formation, though no peaks are observed in the XRD measurement.

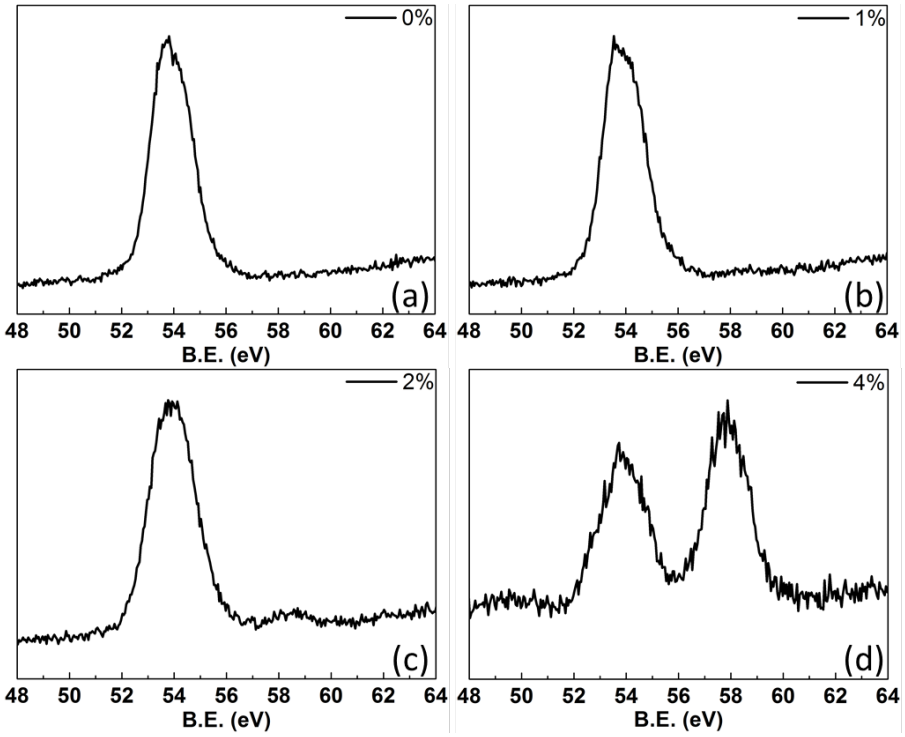

Figure 3.15: XPS Se 3d peak profiles of four $ZnSe_{1-x}O_x$ samples sputtered in (a) 0%, (b) 1%, (c) 2%, and (d) 4% O_2 – content gas mixture.

Similar phenomena are observed from XPS O 1s peak profiles, as shown in Figure 3.16. One small oxygen peak with binding energy 532 eV in Figure 3.16 (a) is attributed to surface contamination due to air exposure for ZnSe film sputtered in pure Ar. For $ZnSe_{1-x}O_x$ film sputtered in 1% oxygen environment (Figure 3.16 (b)), O 1s profile can be deconvoluted into two peaks – one at 532 eV due to surface contamination and the other one at 530.4 eV corresponding to O bonded to Zn in $ZnSe_{1-x}O_x$ [107]. For the sample sputtered in 4% oxygen, the O 1s profile intensity increases and is dominated by the third peak at 531.2 eV, which can be ascribed to oxygen in SeO_3^{2-}. The ratio of integrated peak area divided by atomic sensitivity factor of two peaks – O 1s at 531.2 eV and Se 3d at 58 eV is about 3.4, which roughly agrees

with the above conclusion that $ZnSeO_3$ phase forms when the oxygen content of the sputtering gas mixture increases to 2% and above.

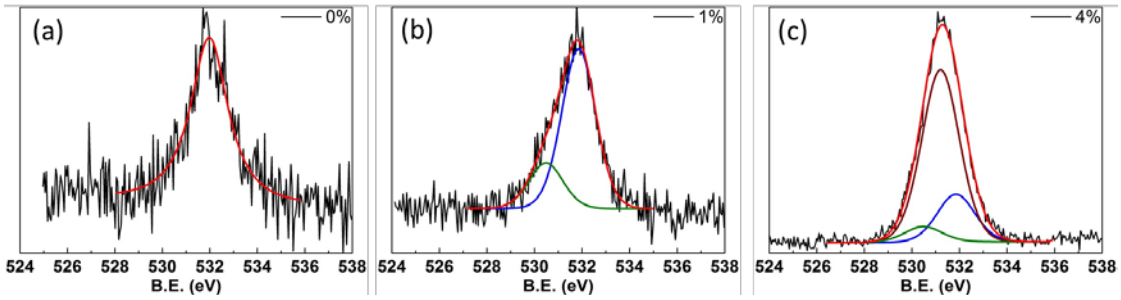

Figure 3.16: XPS O 1s peak profiles of three $ZnSe_{1-x}O_x$ samples sputtered in (a) 0%, (b) 1%, and (c) 4% O_2 – content gas mixture.

$ZnSeO_3$ secondary phase formation is also thermodynamically preferable. Table 3.2 lists several possible reaction pathways to form $ZnSeO_3$, assuming the existence of elemental Zn, Se, O as well as ZnSe, and O_2 in the sputtering plasma. Gibbs free energies of reaction at 298K ΔG_{rxn}^{298K} are calculated based on Gibbs free energies of formation data from ref. [38]. When the oxygen content of the sputtering gas mixture is < 1%, the reaction pathways to $ZnSeO_3$ phase formation are limited due to oxygen scarcity. If there's enough O or O_2 available in the plasma, the reactions proceed to form $ZnSeO_3$, as suggested by the negative values of ΔG_{rxn}^{298K}. As shown in Figure 3.17, the phase diagram of the Zn-O-Se ternary system [108] also demonstrates the formation of $ZnSeO_3$ compound when adequate oxygen is present in the system.

Table 3.2: Possible pathways of $ZnSeO_3$ secondary phase formation and calculated Gibbs free energy of reaction at 298K with Gibbs free energy of formation data from [38].

Reaction	ΔG_{rxn}^{298K} $(KJ \cdot mol^{-1})$
Zn + Se + 3 O (G) ⇌ $ZnSeO_3$	-1260
Zn + Se + 1.5 O_2 (G) ⇌ $ZnSeO_3$	-565
Zn + Se (G) + 3 O (G) ⇌ $ZnSeO_3$	-1455
Zn + Se (G) + 1.5 O_2 (G) ⇌ $ZnSeO_3$	-760
ZnSe + 3 O (G) ⇌ $ZnSeO_3$	-1092
ZnSe + 1.5 O_2 (G) ⇌ $ZnSeO_3$	-396

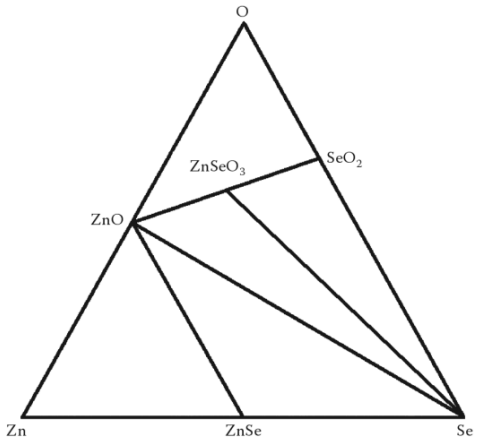

Figure 3.17: The Zn-O-Se ternary system phase diagram at room temperature [108].

3.3.2 CIGS / $ZnSe_{1-x}O_x$ Device Performance

$ZnSe_{1-x}O_x$ films sputtered in 1% oxygen - content gas mixture were chosen to be applied in CIGS devices as the alternative buffer. As shown in the previous studies, $ZnSe_{1-x}O_x$ films prepared under such conditions have bandgap values around 2.5 eV, and the actual O / (O + Se) ratio in the film is around 0.06 – 0.12. Device fabrication steps were similar to the case with the sputtered ZnSe buffers. The device performance

is shown in Figure 3.18 and the JV parameters are summarized in Table 3.3. The results of ZnSe / CIGS and CdS / CIGS are also presented for comparison. The Ga / (Ga + In) ratio of the absorbers used here is around 0.3 with the bandgap E_g about 1.18 eV [19]. As analyzed in section 3.2, compared to the baseline CdS buffer, CIGS / ZnSe device shows a suppressed photocurrent collection due to the conduction band spike / electron transport barrier formed at the junction interface.

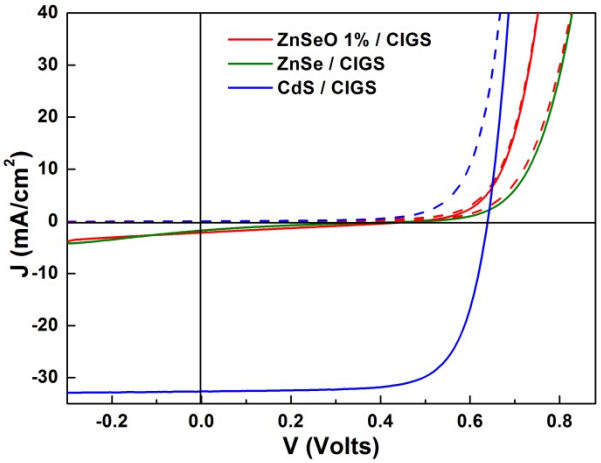

Figure 3.18: JV curves of CIGS devices with $ZnSe_{1-x}O_x$ buffer (sputtered in 1% oxygen-content gas mixture), ZnSe buffer and CdS as reference. Solid curves were measured under AM1.5 illumination and dashed curves were measured in dark.

Table 3.3: JV parameters from Figure 3.18.

Buffer	V_{oc} (mV)	J_{sc} (mA/cm^2)	FF (%)	Eff (%)
ZnSeO	482	2.2	26.2	0.3
ZnSe	489	1.8	17.9	0.2
CdS	639	32.6	71.7	15.0

By incorporating oxygen into ZnSe during the reactive sputtering in 1% oxygen – content gas mixture, $ZnSe_{1-x}O_x$ films are proved to have a bandgap reduction resulting from the conduction band downward shift (section 3.3). Hence the conduction band offset CBO between the buffer $ZnSe_{1-x}O_x$ and CIGS is expected to decrease. However, the CIGS / $ZnSe_{1-x}O_x$ device shows almost no improvement in current collection compared to the one with ZnSe, indicating that the spike type of CBO still significantly impedes the electron transport and collection. The possible explanation could be the limited capabilities of tuning the ZnSe band structure by the approach of oxygen incorporation. It's shown in Figure 3.12 that the $ZnSe_{1-x}O_x$ film sputtered in 1% oxygen - content gas mixture has only 0.2 eV bandgap reduction, which might not be enough to lower the CBO to the preferred range (0 – 0.5 eV). With further increase of the oxygen content in the sputtering gas mixture, the oxygen concentration in the $ZnSe_{1-x}O_x$ film is saturated and second phase formation is observed as discussed in 3.3.1.4. What's more, it's shown in section 3.3 that $ZnSe_{1-x}O_x$ crystallinity decreases dramatically as the concentration of oxygen increases; Composition measurements imply that oxygen are not only incorporated into the ZnSe crystal lattice, but also reside along the grain boundaries. This will create defect states and potentially degrade the $ZnSe_{1-x}O_x$ thin film qualities, as well as the CIGS / $ZnSe_{1-x}O_x$ device performance.

It's interesting to mention the preliminary results of $ZnSe_{1-x}O_x$ applied in ACIGS devices. The advantages of Ag alloying with CIGS have been addressed in Chapter 1. Here ACIGS absorbers (Ag / (Ag + Cu) ratio around 0.3, corresponding to 0.1 eV E_g widening [30]) are tested with the sputtered ZnSe and $ZnSe_{1-x}O_x$ (sputtered in 1% oxygen - content gas mixture) alternative buffers. The results are shown in

Figure 3.19 and the JV parameters are summarized in Table 3.4. Device with the baseline CdS buffer is again included as comparison. Although it still cannot compete with the ACIGS / CdS reference cell, ACIGS / ZnSe and ACIGS / $ZnSe_{1-x}O_x$ both outperform the ones with CIGS absorbers. The JV results indicate a better conduction band alignment between ACIGS and ZnSe / $ZnSe_{1-x}O_x$ alternative buffers. Detailed investigations and optimizations are still needed for a better understanding and application.

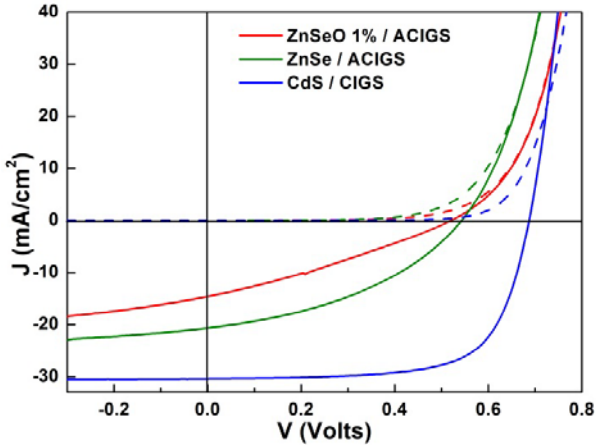

Figure 3.19: JV curves of ACIGS devices with $ZnSe_{1-x}O_x$ buffer (sputtered in 1% oxygen-content gas mixture), ZnSe buffer and CdS as reference. Solid curves were measured under AM1.5 illumination and dashed curves were measured in dark.

Table 3.4: JV parameters from Figure 3.19.

Buffer	V_{oc} (mV)	J_{sc} (mA/cm^2)	FF (%)	Eff (%)
ZnSeO	521	14.6	29.6	2.3
ZnSe	543	20.7	39.9	4.5
CdS	687	30.37	68.8	14.4

Chapter 4

STUDY OF Zn(S,O) ALTERNATIVE BUFFER IN (A)CIGS DEVICES

4.1 Introduction

ZnS is a wide bandgap II-VI compound with the electron affinity around 3.9 eV [55]. The main problem of using ZnS as the alternative buffer in CIGS devices is the electron affinity mismatch, which will create a huge conduction band spike ≥ 0.6 eV at the absorber / buffer junction interface as mentioned in Chapter 1 section 1.3.1 and block the minority carrier transport [36]. On the other hand, if ZnO is couple with CIGS a negative conduction band cliff $\leq$ -0.1 eV as shown in Chapter 1 section 1.3.1 will be formed, which can lead to increased interface recombinations and low V_{oc} performance [109]. It's been reported that when ZnS is alloyed with ZnO to form the intermediate compound Zn(S,O), the bandgap narrowing is observed [110] and the conduction band position can be tuned [68] to obtain a desired conduction band line-up with the CIGS absorber.

As a matter of fact, the application of Cd-free Zn(S,O) buffer layer in the CIGS industry is getting wider. The world record CIGS / Zn(S,O) device has achieved 22.3% efficiency [69]. As with the case of CdS buffer, chemical bath deposition is the mainstream approach for the Zn(S,O) growth. But it involves the handling of massive chemical liquid waste. Recently, over 18% CIGS / Zn(S,O) devices with the buffer deposited by magnetron sputtering have been demonstrated [56]. The result is promising because that the sputtering approach is a more robust and applicable

process to the industry fabrication, while in the chemical bath deposition the formation of hydroxides or oxides is less controllable.

With more and more effort dedicated to the application of Zn(S,O) buffer in CIGS cells, investigation of using this buffer material with ACIGS devices is lacking. The purpose of this project is to develop a robust Zn(S,O) buffer deposition process in our lab and apply it in both CIGS and ACIGS devices with detailed analysis comparing the results with the different absorbers. Considering above-mentioned advantages, RF magnetron sputtering is chosen as the deposition method for the Zn(S,O) buffer. Based on the literature reports about the dependence of the conduction band alignment on the Zn(S,O) composition [56, 68], a mixed compound target containing 70 at.% ZnO and 30 at.% ZnS ($ZnO_{0.7}S_{0.3}$) was selected. The Zn(S,O) was sputtered in Ar environment to SLG (for optical and structural measurements) or Si (for XPS and structural measurements) substrates. The substrate temperature T_{sub} was varied from room temperature to 200°C. The experimental procedures are given in details in Chapter 2. In this chapter, the material characterizations and (A)CIGS device applications of the sputtered Zn(S,O) buffer layer will be discussed in details.

4.2 Material Characterizations of the Sputtered Zn(S,O) Films

4.2.1 Structural Properties

4.2.1.1 GIXRD Measurements

Structural properties of the Zn(S,O) films sputtered at different substrate temperatures on Si wafers were first characterized by GIXRD. Figure 4.1 (a) and (b) show the GIXRD patterns of the Zn(S,O) films compared to ZnO standard from ICDD Powder Diffraction File (PDF) 036-1451 and ZnS standard PDF 036-1450 (black

dotted lines) respectively. The sputtered Zn(S,O) films had the same wurtzite lattice structure as the binary compounds ZnO and ZnS, but the lattice constants changed. The diffraction angles of the main peaks with Miller indices (100), (002) and (101) as labeled in Figure 4.1 (a) and (b) were in between that of ZnO standard and ZnS standard, indicating that both S and O atoms were incorporated into the crystal lattice via the compound target sputtering. The uniform Zn(S,O) ternary compound formation was confirmed by the fact that no phase segregation was observed from the XRD patterns. The Zn(S,O) films sputtered at higher substrate temperatures had better crystallinity, as suggested by the increased XRD peak intensities and reduced peak FWHM in Figure 4.1 (a) and (b). This was further demonstrated by the fine scans of the (002) diffraction peak as shown in Figure 4.1 (c). It was also observed that the (002) peak shifted to higher diffraction angles when the film was sputtered at elevated substrate temperature, corresponding to a decreased lattice spacing and thus reduced sulfur content. With the lattice parameter information of ZnO and ZnS extracted from the PDF standards and the Zn(S,O) lattice constant calculated based on Bragg's law: $2a*\sin\theta = n\lambda$, the Zn(S,O) film compositions can be estimated by application of Vegard's law: $a_{Zn(S,O)} = x * a_{ZnO} + (1-x) * a_{ZnS}$. The compositional variations of the Zn(S,O) films with the substrate temperature changes will be further discussed in Section 4.2.2.

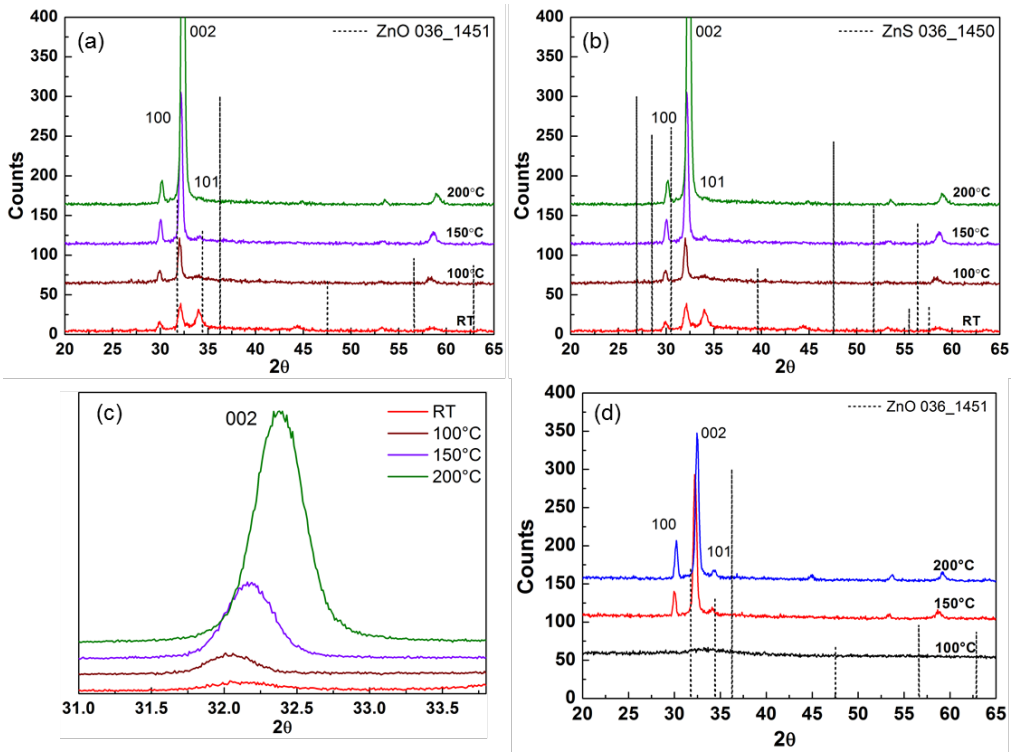

Figure 4.1: (a) GIXRD patterns of Zn(S,O) films sputtered on Si wafers at different substrate temperatures compared to ZnO standard. (b) GIXRD patterns of Zn(S,O) films sputtered on Si wafers at different substrate temperatures compared to ZnS standard. (c) GIXRD fine scans of the (002) peak of Zn(S,O) films sputtered on Si wafers at different substrate temperatures. (d) GIXRD patterns of Zn(S,O) films sputtered on SLG at different substrate temperatures compared to ZnO standard.

Table 4.1: GIXRD (002) peak analysis based on Figure 4.1.

T_{sub}	2θ (°)	a (Å)	
RT	32.118	2.7846	a (ZnO)
100°C	32.019	2.793	2.603 Å
150°C	32.15	2.7819	a (ZnS)
200°C	32.353	2.7649	3.129 Å

The sputtered Zn(S,O) films demonstrated substrate dependent structural properties, as shown in Figure 4.1 (d). ZnO PDF standard was still included in the

black dotted lines. In this case SLG was used as the substrate instead of Si wafer while the other sputtering conditions kept the same. Unlike the Zn(S,O) / Si samples which showed the GIXRD diffraction peaks from room temperature sputtering, the Zn(S,O) / SLG samples started to show the observable peaks when the substrate was heated to 150°C. For lower temperature (T_{sub} = RT or 100 °C) sputtering using the SLG substrates, the Zn(S,O) films were amorphous, indicated by the GIXRD pattern where only a broad bump around $2\theta = 34°$ was observed. Even for the films sputtered at T_{sub} = 150°C and 200°C, poorer crystallinities were found based on the substantially decreased GIXRD peak intensities. The compositions of the sputtered Zn(S,O) films were not affected by the substrate material used, since the diffraction angles of the GIXRD peaks were unchanged for the same T_{sub} sputtering.

4.2.1.2 SEM Measurements

SEM was also used to characterize the structural properties of the sputtered Zn(S,O) films. Figure 4.2 shows two samples sputtered on Si wafer substrates at T_{sub} = room temperature (Figure 4.2 (a)) and T_{sub} = 200°C (Figure 4.2 (b)). Both lower magnification (30 KX) and higher magnification SEM images are presented here. Compared to the Zn(S,O) grains in Figure 4.2 (a), the crystal growth under higher temperature sputtering can be observed from Figure 4.2 (b). The grain size was still under 100 nm based on the SEM measurements even though the substrate was heated to 200°C. Such poor crystallinity of the sputtered intermediate Zn compound was also reported by other groups [111]. SEM images showed consistent results with the XRD measurements as discussed in 4.2.1.1.

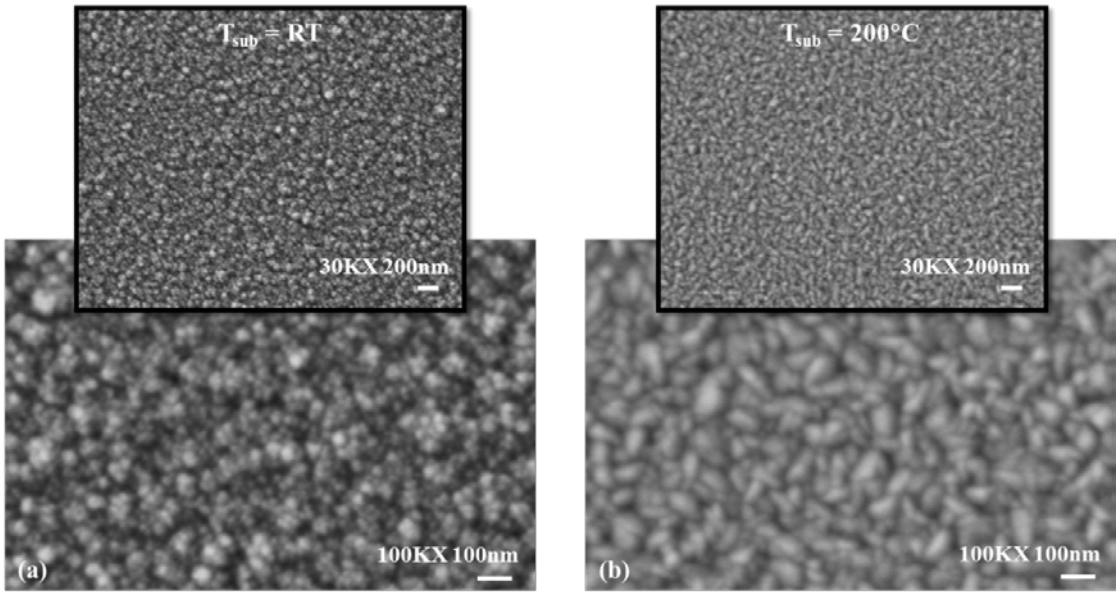

Figure 4.2: (a) SEM image of the Zn(S,O) film sputtered on Si substrate at T_{sub} = room temperature. (b) SEM image of the Zn(S,O) film sputtered on Si substrate at T_{sub} = 200°C.

4.2.2 XPS and Compositional Analysis

XPS was used to characterize surface properties of the sputtered Zn(S,O) films. Since XPS is a surface sensitive technique, Zn(S,O) samples were loaded into XPS chamber shortly after the sputtering deposition with air exposure time kept within one hour. Low-voltage (500V) Ar sputter-cleaning of the sample surface was carried out first in the XPS main chamber to remove C-O contaminations before taking the actual measurements. Figure 4.3 shows the XPS fine scan and the fit spectra for the S 2p spin orbit splitting doublets of a Zn(S,O) sample after 30 mins of soft Ar sputter surface cleaning. The Zn(S,O) sample was sputtered at T_{sub} = room temperature in this case. The binding energy of the S 2p peak demonstrated the presence of sulfide (Zn-S bond). No sulfates or other S-O phases were observed from XPS measurements. Similar

phenomena were found for the other Zn(S,O) films sputtered at various substrate temperatures.

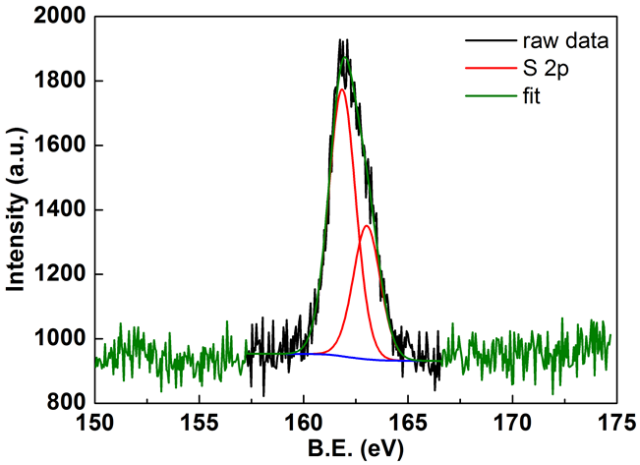

Figure 4.3: XPS fine scan for the S 2p spin orbit splitting doublet peaks of a Zn(S,O) sample.

Both XPS quantitative analysis and XRD calculation were applied to determine the compositions of the sputtered Zn(S,O) films. The approach of the XRD data analysis was described in 4.2.1.1. For XPS measurements, the composition analysis was conducted based on the integrated elemental peak areas divided by their sensitivity factors [84]. The S / (S+O) ratios of the Zn(S,O) films sputtered at different substrate temperatures measured by both XRD and XPS approaches are listed and compared in Table 4.2 and Figure 4.4. The compound target composition S / (S+O) = 0.3 is also included in Figure. 4.4. It's shown that the compositions of the sputtered Zn(S,O) films were very close to the target with slightly higher sulfur concentration. Meanwhile the films sputtered at higher substrate temperatures suffered from mild sulfur loss. The diffraction peak shifting with various substrate temperatures observed

from the XRD patterns in Figure 4.1 was due to the film compositional changes. The results from XRD and XPS measurements were similar and consistent with each other.

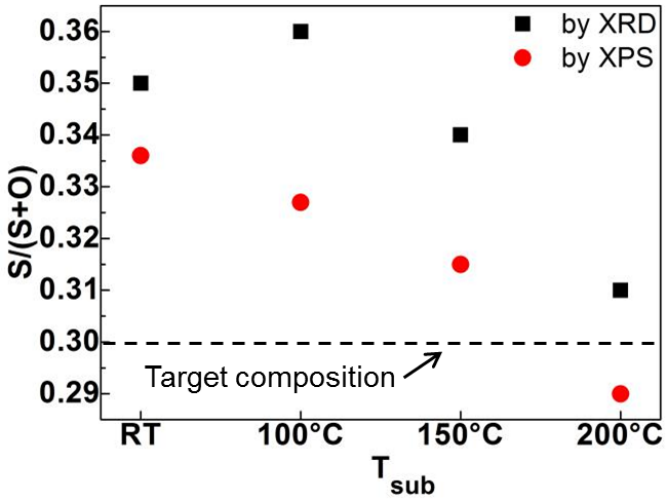

Figure 4.4: The S / (S+O) ratios of the Zn(S,O) films sputtered at different substrate temperatures measured by both XRD and XPS. The compound target composition is also plotted with S / (S+O) ratio = 0.3.

Table 4.2: The S / (S+O) ratios of the Zn(S,O) films sputtered at different substrate temperatures measured by both XRD and XPS.

T_{sub}	S/(S+O)	
	by XRD	by XPS
RT	35	33.6
100°C	36	32.7
150°C	34	31.5
200°C	31	29

4.2.3 Optical Properties

4.2.3.1 UV/Vis Spectrophotometer Measurements

The optical transmittance and reflectance of the Zn(S,O) films sputtered onto SLG substrates at different temperatures were measured by UV/Vis spectrophotometer. The transmittance spectra in the wavelength range from 250 nm to 850 nm are plotted in Figure 4.5 (a). Also included is the room temperature sputtered ZnO transmittance spectrum for comparison. The transmittance onset edges of the Zn(S,O) films were very close to that of ZnO, with a shift to longer wavelength region for the samples sputtered at higher T_{sub}. The Zn(S,O) films demonstrated decreased transmittance around the bandgap edges (350 nm – 450 nm) compared to the ZnO reference, indicating the existence of the sub-bandgap absorption tails [83]. This is better shown from the $(\alpha E)^2$ vs. E plots of the Zn(S,O) films and ZnO reference in Figure 4.5 (b). Here the absorption coefficient α was calculated by the equation [83]:

$$\alpha \approx \frac{1}{d} \ln \frac{(1-R)^2}{T} \tag{4.1}$$

where T and R stand for transmittance and reflectance from the UV-Vis spectrophotometer measurements; d is the film thickness determined from Dektak profilometer and cross-section SEM measurements. The absorption coefficient can also be expressed by the relation $\alpha(h\upsilon) \sim (h\upsilon - E_g)^{\frac{1}{2}}$ (where $h\upsilon$ is the photon energy) for the direct bandgap materials [83]. Therefore the E_g values of the Zn(S,O) films or ZnO reference can be derived by linear extrapolation of the $(\alpha E)^2$ vs. E plots to the x-axis. According to the structural analysis in section 4.2.1, the sputtered Zn(S,O) films had poor crystallinities with the grain size under 100 nm scale even though the substrate temperature had been increased to 200°C. The structural disorders created defect states around the conduction and valence band edges, leading to the observed

sub-bandgap absorptions. This is further demonstrated by the significantly different plot profiles between the ZnO reference and the Zn(S,O) films in Figure 4.5 (b). In contrast to the sputtered Zn(S,O), the highly crystalized ZnO film showed a sharp absorption edge, with the E_g value derived to be 3.3 eV. The E_g of the Zn(S,O) films were also determined from the linear extrapolation of the $(\alpha E)^2$ vs. E plots in Figure 4.5 (b). And the inset figure gives one example of the linear fitting for the Zn(S,O) sample sputtered at T_{sub} = 200°C. The derived E_g values are shown in Figure 4.6. The sputtered Zn(S,O) was confirmed to have E_g close to that of ZnO. The E_g value decreased slightly at elevated T_{sub}. The sputtered Zn(S,O) films don't have sharp band edges due to the substantial sub-bandgap absorptions, which makes accurate E_g determination uncertain, but the E_g variations of Zn(S,O) films as a function of T_{sub} can still be obtained by this method. Based on the compositional analysis in section 4.2.2, the bandgap narrowing corresponded to the decreased sulfur content of the Zn(S,O) films sputtered at higher substrate temperature, which was consistent with the literature reports [68].

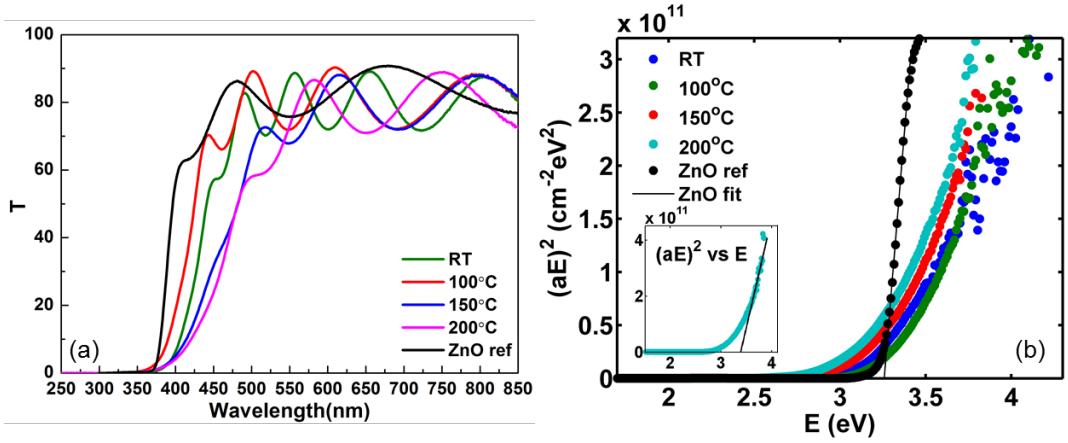

Figure 4.5: (a) The transmittance spectra of the Zn(S,O) films sputtered at different substrate temperatures. The transmittance spectrum of ZnO sputtered at room temperature is also plotted for comparison. (b) The $(\alpha E)^2$ vs. E plots of the Zn(S,O) films sputtered at different substrate temperatures and the ZnO reference for the bandgap estimation. The inset figure shows one example of linear fitting to derive E_g of the Zn(S,O) sample sputtered at 200°C.

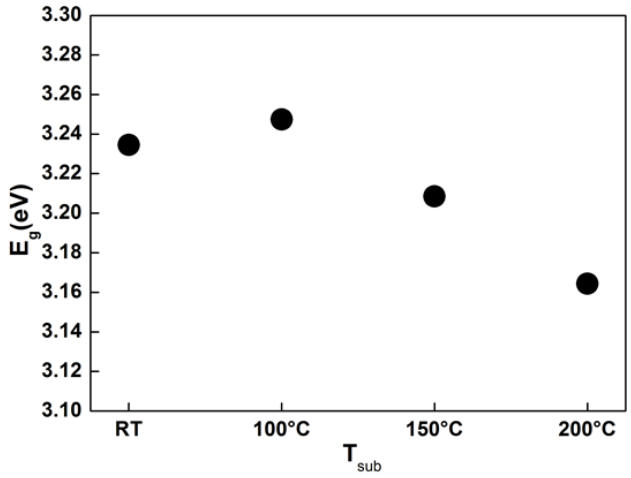

Figure 4.6: The derived E_g values of the Zn(S,O) films sputtered at different substrate temperatures.

4.2.3.2 Raman Spectroscopy Measurements

Raman spectroscopy was also used to characterize the optical properties of the Zn(S,O) films deposited onto SLG substrates. The irradiation laser beam of the Raman measurements was 532 nm. The irradiation power was below 2mW to avoid any property modifications due to the local heating.

Based upon the optical phonon behaviors, the mixed ternary compounds can be classified into two types: 'one-mode' phonon behavior type and 'two-mode' phonon behavior type [112]. In 'one-mode' behavior type, the optical phonon peaks vary approximately linearly and closely with the compound compositional changes from the characteristic frequencies of one binary member to the other one. In 'two-mode' behavior type, two sets of allowed optical phonon peaks that belong to the two binary end members coexist in the Raman spectrum with the frequencies close to the characteristic ones of the binary compounds. The modified random-element-isodisplacement (MREI) model [112] gives the criteria to predict which phonon mode a ternary compound would exhibit. If the compound $AB_{1-x}C_x$ qualifies for the conditions: $m_B < \mu_{AC} < m_A$, m_C and $m_C > \mu_{AB}$, it should follow the 'two-mode' phonon type. Otherwise the compound would follow the 'one-mode' type. Here m stands for the atomic mass and μ is the reduced mass of the binary compound calculated via the equation $\mu = \frac{m_1 * m_2}{m_1 + m_2}$. For the sputtered $ZnO_{1-x}S_x$ ternary compound, $m_{Zn} = 65.38$, $m_O = 16$, $m_S = 32$, $\mu_{ZnO} = 12.85$ and $\mu_{ZnS} = 21.48$ [113]. The above mentioned criteria are satisfied – $m_O < \mu_{ZnS} < m_{Zn}$, m_S and $m_S > \mu_{ZnO}$, therefore $ZnO_{1-x}S_x$ should follow the 'two-mode' phonon behavior.

Wurtzite ZnO and ZnS belong to the C_{6v}^4 space group [114]. Group theory predicts that the 1st order optic modes at the Γ point of the Brillouin zone are expressed as $\Gamma_{opt} = A_1 + 2B_1 + E_1 + 2E_2$ [114]. While A_1, E_1, and E_2 modes are Raman

active, B_1 are silent modes that won't show up in the Raman spectrum. Two E_2 modes are non-polar branches and associated with the Zn atom motion (E_2^{low}) and the oxygen atom (sulfur atom) motion (E_2^{high}). A_1 and E_1 are polar branches and each splits into longitudinal optical mode (LO) and transverse optical mode (TO) with different wavenumbers. The Raman optical peak assignments for both ZnO and ZnS have been well studied in the literature [114-117].

Figure 4.7 presents the Raman spectra of two Zn(S,O) samples sputtered at 150°C (in green) and 200°C (in red). The spectrum of a reference ZnO sample prepared by RF sputtering is also plotted for comparison (in black). The Raman phonon peaks of the sputtered Zn(S,O) films were closely related to its structural properties. For the Zn(S,O) sputtered at 100°C and room temperature onto SLG substrates, no XRD diffraction peaks were observed as shown in Figure 4.1. This was also the case for the Raman phonon peaks (not plotted here). The Zn(S,O) sputtered at 200°C had better crystallinity than the one sputtered at 150°C as discussed in 4.2.1. Also Raman peaks with higher intensities were observed from Figure 4.7.

The ZnO E_2^{high} phonon peak at the frequency 438 cm^{-1} was related to the oxygen atom vibration. It's very sensitive to the lattice distortion or structural defects induced by doping or alloying with the peak shift, broadening or weakening phenomena observed [118]. In the case of sulfur substitution of oxygen atoms, the ZnO E_2^{high} peak vanished [113] as seen from Figure 4.7. ZnO A_1(LO) and E_1(LO) phonon modes overlapped with each other and showed up as a broad peak around 575 cm^{-1}. With the incorporation of sulfur, red shift to the lower wavenumber of this peak was observed. The amount of shift corresponded to the amount of sulfur present in the film [113]. For the sample sputtered at 200°C, this phonon peak shifted to the

frequency around 536 cm^{-1}; for the sample sputtered at 150°C with slightly higher sulfur content (Figure 4.4), this peak shifted to the even lower frequency at 531 cm^{-1}. Above observation could be used as an indicator of the sulfur content in the Zn(S,O) films. The broad peak at 351 cm^{-1} and the peak at 261 cm^{-1} were attributed to the ZnS overlapping $A_1(LO)$ / $E_1(LO)$ modes and $A_1(TO)$ / $E_1(TO)$ modes respectively, which stayed close to the characteristic peak frequencies of the binary compound ZnS [117]. Another broad peak at the frequency 208 cm^{-1} was assigned to the second order Raman scattering of ZnO [115]. The analysis of the Zn(S,O) Raman spectra confirmed that this ternary compound indeed followed the 'two-mode' phonon behavior as predicted by the MREI model [112]. The optical phonon frequencies were highly sensitive to the structural and compositional variations of the sputtered Zn(S,O) films.

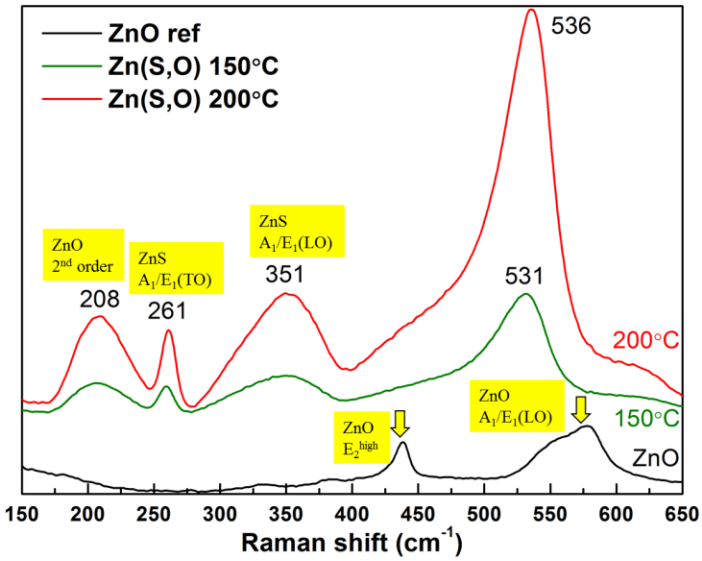

Figure 4.7: The Raman spectra of the ZnO reference and the Zn(S,O) films sputtered at different substrate temperatures.

4.3 Applications of the Sputtered Zn(S,O) Buffer in (A)CIGS Devices

4.3.1 Device Fabrications

The sputtered Zn(S,O) film was applied as the alternative buffer with both CIGS and ACIGS absorbers produced in our lab. The device structure is shown in Figure 4.8. The sputtered Zn(S,O) buffer replaced the chemical bath deposited CdS while the other processing steps remained the same. The Zn(S,O) films was sputtered at T_{sub} = room temperature for the device application. Similar to the CBD-CdS buffer, the thickness of the Zn(S,O) buffer was around 50 nm. The Ga / (Ga+In) ratio was around 0.3 – 0.4 for the baseline absorbers and Ag / (Ag+Cu) ratio was around 0.2 for ACIGS. The baseline (A)CIGS / CdS devices were always fabricated in parallel with (A)CIGS / Zn(S,O) devices using the absorbers grown in the same evaporation run. In this way the (A)CIGS / CdS devices acted as the reference or control cells to better evaluate the performance of the Zn(S,O) alternative buffer. Usually the baseline CIGS / CdS cells achieved ~ 15% efficiency and ACIGS / CdS cells could reach over 17% efficiency in our lab.

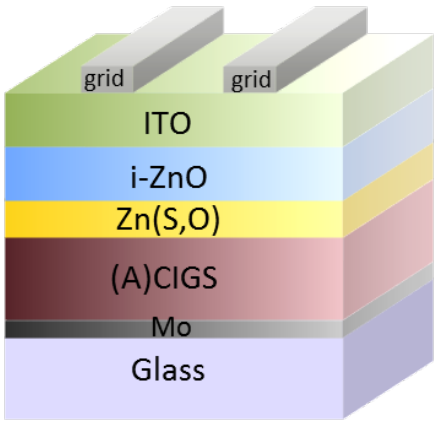

Figure 4.8: The device structure of the (A)CIGS / Zn(S,O) solar cells.

Figure 4.9 shows the cross section SEM image of the sample SLG / Mo / ACIGS / Zn(S,O) after the buffer sputtering growth. The Zn(S,O) layer thickness was around 50 nm in this case. It can be observed that the sputtered Zn(S,O) film uniformly covered the absorber layer and closely followed the morphology of the ACIGS grains.

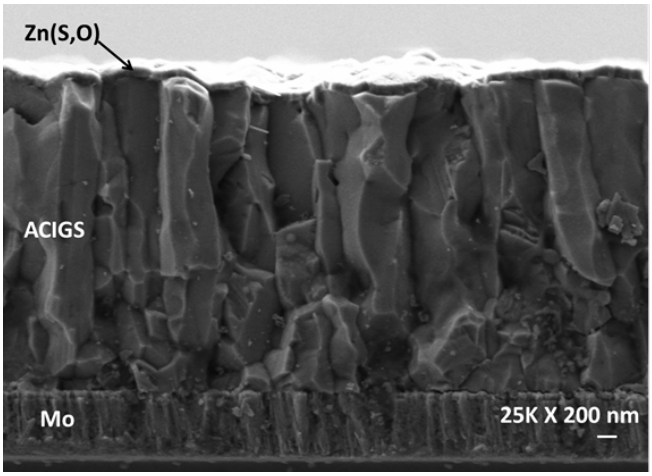

Figure 4.9: The cross section SEM image of the sample Zn(S,O) / ACIGS / Mo / SLG.

4.3.2 Champion CIGS / Zn(S,O) and ACIGS / Zn(S,O) Devices

4.3.2.1 Device Performance

Figure 4.10 shows the JV results of the champion CIGS / Zn(S,O) device (Figure 4.10 (a)) and ACIGS / Zn(S,O) device (Figure 4.10 (b)). The light and dark JV curves were plotted in red and the corresponding JV parameters were displayed in the inset tables. The reference cells with the CBD-CdS buffer were also plotted in blue curves. The Zn(S,O) layer was sputtered at T_{sub} = room temperature with the thickness

around 50 nm. The CIGS and ACIGS absorbers in this case went through the Cd PE treatment for 1 min before Zn(S,O) deposition. Absorber surface treatments will be discussed in section 4.3.3. Both CIGS / Zn(S,O) and ACIGS / Zn(S,O) devices had the J_{sc} and FF similar to their reference cells with the CdS buffer. The CIGS / Zn(S,O) cell achieved 12.5% efficiency with V_{oc} about 50 mV less than the reference. The ACIGS / Zn(S,O) cell achieved 13.2 % efficiency with V_{oc} about 100 mV less than the reference. It was found that the V_{oc} deficiency was the main factor limiting the device performance. The V_{oc} and efficiency deficit of ACIGS / Zn(S,O) devices compared to the reference cells were always greater than the case with CIGS / Zn(S,O) devices. The incorporation of Ag into the chalcopyrite system complicated the absorber surface properties, which was then reflected by the application of the sputtered Zn(S,O) buffer in the devices. However, the underlying mechanism for the different behaviors between CIGS and ACIGS devices still needs further investigation.

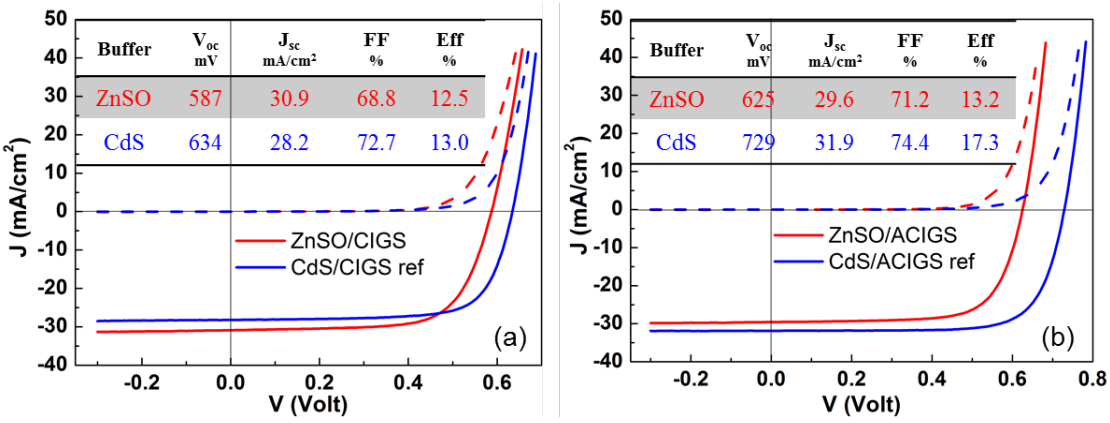

Figure 4.10: (a) The JV plots of the champion CIGS / Zn(S,O) device and the reference CIGS / CdS cell. (b) The JV plots of the champion ACIGS / Zn(S,O) device and the reference ACIGS / CdS cell.

4.3.2.2 Device Analysis

In order to investigate the recombination mechanism that limited the V_{oc} behavior of (A)CIGS devices with the sputtered Zn(S,O) buffer, temperature dependent V_{oc} (V_{oc} – T) measurements were conducted. There exist several recombination pathways in the (A)CIGS thin film solar cells that could dominate the device performance and lead to low V_{oc} values, including the electron-hole recombination in the space charge region or the neutral region of the absorber layer, or at the critical interfaces of the device (e.g. absorber / buffer interface, absorber / back contact interface) [91]. Since the major difference between (A)CIGS / Zn(S,O) and (A)CIGS / CdS cells was the buffer layer option, it's suspected that the recombination currents at the absorber / Zn(S,O) interface via the defect states led to the low V_{oc} behaviors.

Based on the method given in [91], the open circuit voltage V_{oc} can be expressed as:

$$V_{oc} = \frac{\Phi_b}{q} - \frac{AkT}{q}\ln(\frac{J_{00}}{J_L}) \tag{4.2}$$

where Φ_b stands for the barrier height, q is the electron charge, A is the ideality factor, J_{00} is the prefactor of the diode current dependent on the specific recombination mechanism and J_L is the light generated current. By recording the V_{oc} at different temperature, the V_{oc} at T = 0K as well as the barrier height Φ_b can be derived. Figure 4.11 shows the V_{oc}-T measurements of the ACIGS / Zn(S,O) cell (in red) and its reference cell with the CdS buffer (in blue). The temperature range was varied from 120 K to 440 K. V_{oc} vs. T was plotted and the data was fitted with a linear line extrapolating to T = 0K. The intercept gave the Φ_b value. For the reference ACIGS / CdS cell, Φ_b was determined to be 1.13 eV, close to the E_g of the ACIGS layer,

indicating that the dominant recombination path was in the bulk of the absorber [91]. The result of $\Phi_b = E_g$(absorber) is commonly observed for well-behaved (A)CIGS solar cells where the absorber / buffer (usually CBD-CdS) interface is of high quality [91]. However, the determined Φ_b = 938 meV of the ACIGS / Zn(S,O) cell was much less than the absorber bandgap value, which supported the previous hypothesis that the ACIGS / Zn(S,O) interface recombination via the trap states dominated the device behavior and led to the observed low V_{oc}. Similar results were also found for our CIGS / Zn(S,O) devices where Φ_b was only 1.02 eV, below the bulk E_g of the absorber.

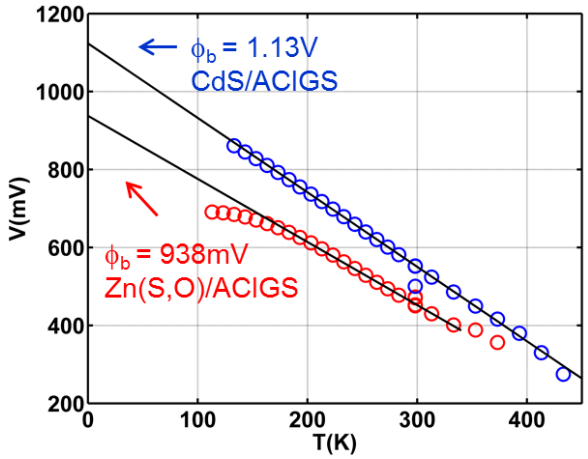

Figure 4.11: The V_{oc}-T measurements of the ACIGS / Zn(S,O) device and the reference ACIGS / CdS device.

Since the sputtered Zn(S,O) buffer layer has a wider bandgap (see Figure 4.6) than the CBD-CdS (2.4 eV), less light absorption loss should occur in the buffer region and therefore higher J_{sc} is expected for the devices with the Zn(S,O) buffer. However, in most cases J_{sc} of the (A)CIGS / Zn(S,O) devices was around 30 mA/cm^2,

close to the reference cells with the CBD-CdS buffer. The main advantage of using a wider bandgap buffer material has not been realized so far.

To better understand the current collection in the (A)CIGS / Zn(S,O) devices QE measurements were carried out. Figure 4.12 shows the QE results of one ACIGS / Zn(S,O) cell (solid red curve) and its reference cell (solid black curve) for comparison. The measurement range was from 360 nm to 1200 nm. No external voltage was applied. In the short wavelength region the enhanced current with the Zn(S,O) buffer was indeed observed, showing that the wider bandgap Zn(S,O) buffer did allow more blue light to reach the absorber layer underneath. However, the current collection gain in the blue region was compensated by the loss in the mid to long wavelength region (700 nm – 1000 nm), as shown clearly in Figure 4.12. The QE measurements explained the underperformed J_{sc} value of the devices. To further analyze the origin of the mid to long wavelength region loss, optical reflection measurements were conducted for the devices. The QE data corrected by calculating $(\frac{\mathrm{QE}}{1-\mathrm{R}})$ were plotted for ACIGS / Zn(S,O) in a dashed red line and ACIGS / CdS reference in a dashed black line in Figure 4.12. The ratios of QE and $\frac{\mathrm{QE}}{1-\mathrm{R}}$ for ACIGS / Zn(S,O) and ACIGS / CdS devices were also included as the inset in Figure 4.12 for better comparison. It's shown that the mid to long wavelength region loss of ACIGS / Zn(S,O) device was greatly reduced once the QE was corrected from optical reflection, indicating that the optical loss was the main reason for not achieving a higher J_{sc} with the Zn(S,O) buffer.

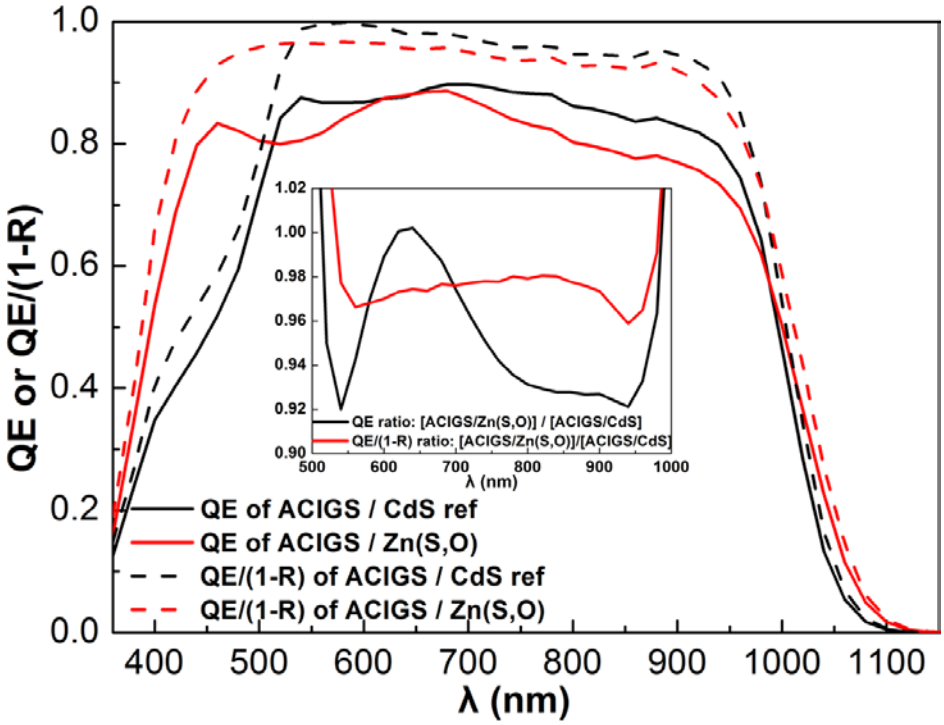

Figure 4.12: The quantum efficiency analysis of the ACIGS / Zn(S,O) device and the reference ACIGS / CdS device. The inset shows the ratio of $QE_{[ACIGS/Zn(S,O)]}$ / $QE_{[ACIGS/CdS]}$ in black and the ratio of $\frac{QE}{1-R}_{[ACIGS/Zn(S,O)]}$ / $\frac{QE}{1-R}_{[ACIGS/CdS]}$ in red.

4.3.3 The Absorber Surface Treatments

4.3.3.1 Introduction

As mentioned in Chapter 2 Experimental Methods, after taking the (A)CIGS absorbers out of the evaporation system and before loading them into the Zn(S,O) sputtering chamber, the absorbers went through various surface cleaning or treatment procedures in an effort to minimize contamination from the air exposure during the sample transfer. While the deionized water rinse was simply to remove any residue dust or soluble sodium compounds without altering the absorber surface properties,

the other treatments (KCN cleaning, Cd PE, and Zn PE) were believed to induce the chemical and electronic modifications of the (A)CIGS surface.

KCN cleaning: KCN treatment is a common technique used for the surface cleaning of chalcopyrite absorbers. It can effectively eliminate excess elemental Se during the cool down time after the film deposition and the residual copper selenide compounds existed on the absorber surface or in the grain boundaries [119, 120]. Copper selenide is a conductive material which could create the shunting path and destroy the diode. Copper selenide is likely to form when excess Cu is provided during the absorber growth. By application of the KCN cleaning the absorber composition can be restored from Cu rich to the stoichiometric state.

Cd PE treatment: The CBD-CdS has worked well with the (A)CIGS absorbers, producing the solar devices with high efficiencies and reproducibility. The chemical bath process not only deposits a thin layer of CdS on top of the (A)CIGS, but also modifies the surface properties of the absorber. The harsh alkaline environment of the chemical solution helps remove the native oxides of In or Ga formed on the absorber surface due to the air exposure [121]. More importantly, Cd ions diffuse into the top few atomic layers of CIGS and possibly occupy the Cu vacancies V_{Cu} [122]. Since Cd is a n-type donor of CIGS, the Cd doping may invert the surface CIGS into a n^+ layer and achieve the preferred conduction band downward bending near the heterojunction interface, which is beneficial for the minority carrier collection [45].

For alternative buffer materials and deposition approaches, the Cd PE treatment (which is a solution of Cd salt and ammonium hydroxide) can also introduce the effective Cd doping of CIGS surface layer and prepare the absorber with preferred electronic and chemical status [123] for the following process. The existence of Cd

ions within the top few atomic layers of the absorbers after a short Cd PE treatment was confirmed from the XPS and SIMS measurements. The device performance improvement was also reported [123].

Zn PE treatment: The same idea of modifying the absorber surface properties by Cd PE treatment applies to the Zn PE process. Zn has also been reported as a n-type donor of CIGS and is likely to occupy the Cu vacancies when diffused into the material [124]. Therefore the Zn doping can also achieve the type inversion of the absorber surface like the case with Cd doping, creating the desired electronic band structure for the electron transport [123]. More importantly, a fully Cd-free process can be realized with the application of Zn PE treatment with regard to the environment and safety issues. The Zn PE process of the (A)CIGS surface is similar to the Cd PE treatment with a solution of $ZnSO_4$ salt and ammonia hydroxide. The experimental details are described in Chapter 2.

4.3.3.2 Effects on Device Performance

The various absorber surface treatments mentioned above were applied to both CIGS and ACIGS absorbers before the Zn(S,O) buffer sputtering. Figure 4.13 shows the JV plots of the best devices from each absorber surface treatment (no treatment, DI water rinse, KCN clean, Cd PE and Zn PE respectively) for CIGS / Zn(S,O) cells (Figure 4.13 (a)) and ACIGS / Zn(S,O) cells (Figure 4.13 (b)). The corresponding JV parameters are collected in Table 4.3 for CIGS and Table 4.4 for ACIGS. The Zn(S,O) buffer was sputtered at T_{sub} = room temperature with the thickness around 50 nm.

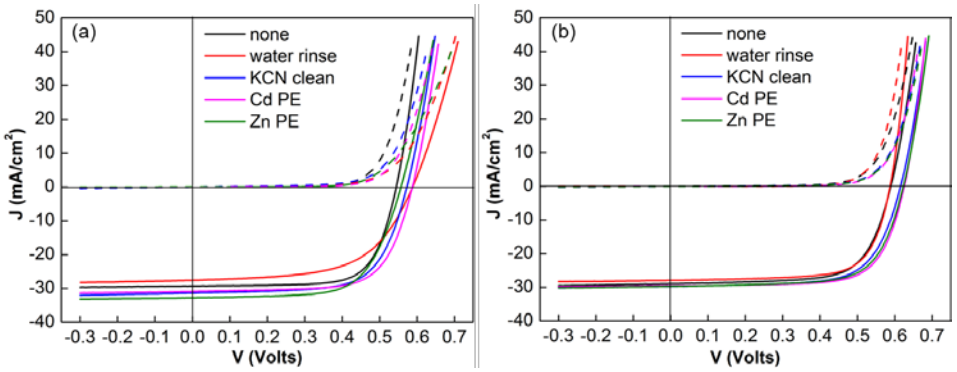

Figure 4.13: (a) The JV plots of CIGS / Zn(S,O) cells with various absorber surface treatments. (b) The JV plots of ACIGS / Zn(S,O) cells with various absorber surface treatments.

Table 4.3: CIGS/Zn(S,O) device performance with various absorber surface treatments.

	V_{oc} mV	J_{sc} mA/cm^2	FF %	Eff %
none	544	29.3	71.1	11.3
water rinse	588	27.6	58.3	9.5
KCN clean	573	31.4	67.2	12.1
Cd PE	587	30.9	68.8	12.5
Zn PE	557	32.8	66.2	12.1

Table 4.4: ACIGS/Zn(S,O) device performance with various absorber surface treatments

	V_{oc} mV	J_{sc} mA/cm^2	FF %	Eff %
none	590	28.9	69.0	11.8
water rinse	588	27.9	70.8	11.6
KCN clean	616	29.8	68.3	12.5
Cd PE	625	29.6	71.2	13.2
Zn PE	623	29.7	69.3	12.8

CIGS and ACIGS devices over 10% efficiency were made from all of those absorber surface treatment approaches and the dependence of the cell performance on the surface treatments applied can be observed. The (A)CIGS / Zn(S,O) devices with no absorber surface treatment or DI water rinse generally had lower efficiencies and V_{oc}. With KCN cleaning the absorber surface, the junction interface was of better qualities. The cell performance got boosted. The most effective way to reduce the heterojunction interface defect states was by applying the absorber surface Cd PE or Zn PE treatment. The PE treatment apparently modified the absorber surface chemical environment and electronic band structure to the preferred state as suggested by the literature [123, 124]. The interface recombination current was therefore reduced, which led to improved V_{oc} and efficiency. So far the champion CIGS / Zn(S,O) and ACIGS / Zn(S,O) devices as seen in Figure 4.10 both had the absorber Cd PE treatment, suggesting the necessity of this step to our device processing flow. Zn PE treatment did not work as effectively as Cd PE treatment but still outperformed the other absorber surface treatment approaches. The ACIGS absorber growth process was better optimized in our lab and thus had higher and more consistent performance than the CIGS absorbers. Although the device performance for both CIGS / Zn(S,O) and ACIGS / Zn(S,O) as shown in Table 4.3 and Table 4.4 was close to each other, the efficiency and V_{oc} deficits of ACIGS / Zn(S,O) cells when compared to their reference cells with the CdS buffer were greater.

From a statistical point of view, the dependence of the (A)CIGS / Zn(S,O) device performance (Efficiencies and V_{oc}) on the absorber surface treatments is demonstrated in Figure 4.14 (CIGS cells) and Figure 4.15 (ACIGS cells). The biggest challenge in the Zn(S,O) alternative buffer project has been the irreproducible device

performance. Quite different device behaviors were often observed for two cells using the absorber and buffer from the same runs and going through the other processing steps side by side – one might show efficiency over 10% while the other had less than 1% efficiency with a huge kink present in the light JV curve. This has happened with both CIGS and ACIGS devices with the Zn(S,O) buffer. It's likely that the sputtered Zn(S,O) layer was sensitive to slight variations of the absorber surface defect states or local electronic property fluctuations. It's apparently not as robust and tolerant a process as the CBD CdS. Figure 4.14 and Figure 4.15 show the scattered efficiency and V_{oc} values for (A)CIGS / Zn(S,O) devices under various absorber surface treatments. The fact that we did not have consistent device behavior indicated that the absorber surface treatment was not the only influence on the cell performance. The complexity of the problem added to the difficulty of drawing conclusions on the effectiveness of absorber surface treatments. However, we did observe that the probability of obtaining the (A)CIGS / Zn(S,O) devices with higher efficiency and V_{oc} was higher when KCN or PE treatment was applied to the absorber surface. And both the champion CIGS / Zn(S,O) and ACIGS / Zn(S,O) cells had received the Cd PE treatment. While with no absorber surface treatment or DI water rinse, the (A)CIGS / Zn(S,O) JV behaviors tended to be worse and more irreproducible. The observed results here emphasized the essential modifications of the PE treatment introduced to the absorber surface, and the importance of this step in our device processing flow.

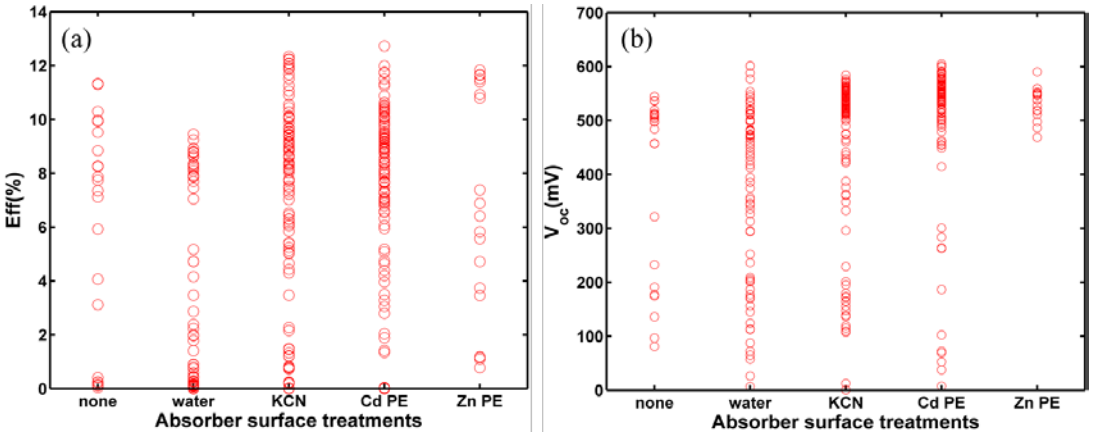

Figure 4.14: Summary of the CIGS / Zn(S,O) device performance under various absorber surface treatments. (a) Efficiencies of the CIGS / Zn(S,O) cells. (b) V_{oc} of the CIGS / Zn(S,O) cells.

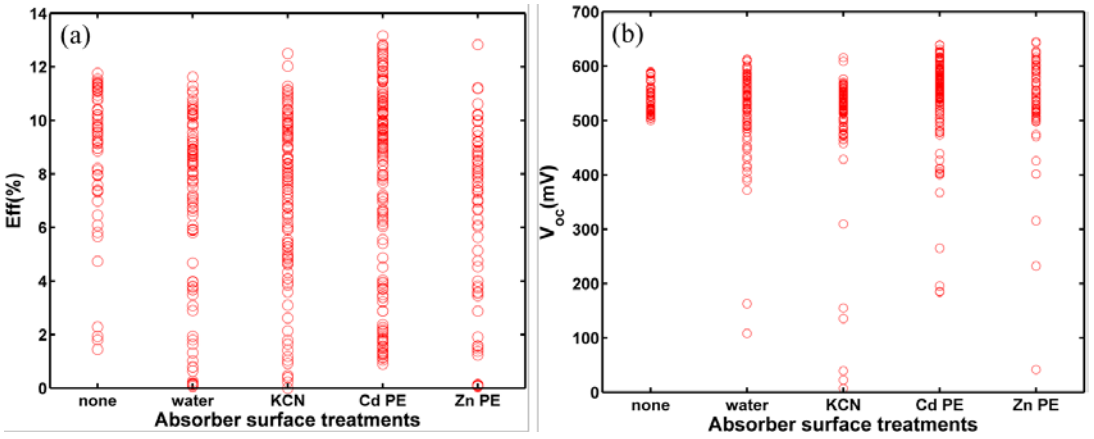

Figure 4.15: Summary of the ACIGS / Zn(S,O) device performance under various absorber surface treatments. (a) Efficiencies of the ACIGS / Zn(S,O) cells. (b) V_{oc} of the ACIGS / Zn(S,O) cells.

4.3.4 Effects of Light Soaking and Forward Biasing Treatments

There are several ways to improve the (A)CIGS cell performance after the device fabrication steps are completed, including post annealing, light soaking, and forward bias treatments. Those device post-treatments have been reported to

dramatically enhance the (A)CIGS / Zn(S,O) cell efficiencies due to the compensation of metastable states at the heterojunction interface [125]. They were also applied to our (A)CIGS cells with the sputtered Zn(S,O) buffer.

As one example, Figure 4.16 shows the light JV curves for a ACIGS / Zn(S,O) cell before (initial test) and after light soaking (LS) plus 0.7V forward bias (close to the cell V_{oc} value) treatments for couple of hours. The corresponding JV parameters are collected in Table 4.5. Light soaking was done under the standard 100 mW/cm^2 light intensity while the device was kept under room temperature. The ACIGS absorber received Cd PE treatment for 1 min before the Zn(S,O) buffer deposition. In contrast to the literature report [125] (where CBD- or ALD-Zn(S,O) buffer was used), our ACIGS / Zn(S,O) device demonstrated superior stability. V_{oc} and J_{sc} remained almost the same after the LS + forward bias treatments. FF was improved slightly and the efficiency boost was less than 1%. Similar device behaviors were also observed for the CIGS / Zn(S,O). The difference between the literature reports and our experiment results suggested the dependency of the Zn(S,O) properties and interface metastable defect states on the specific processing approaches.

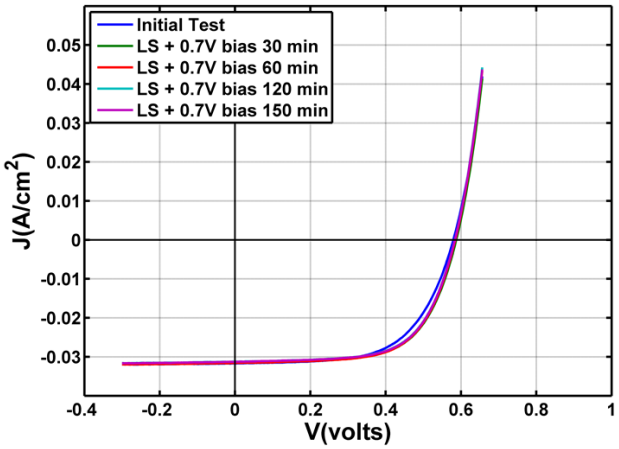

Figure 4.16: ACIGS / Zn(S,O) device JV curves under illumination before (initial test) and after light soaking + 0.7V forward bias treatments.

Table 4.5: JV results after light soaking + 0.7V treatment.

LS+0.7V bias	V_{oc} (mV)	J_{sc} (mA/cm^2)	FF (%)	Eff (%)
Initial	580	31.7	61	11.2
30min	587	31.5	64.3	11.9
60min	585	31.6	64.3	11.9
120min	584	31.2	64.4	11.7
150min	584	31.3	64.4	11.8

4.3.5 Effects of Sputtering Damage

The sputtering damage has been argued to cause CIGS device degradation [126]. It's possible that the high energy ion bombardment of the absorber surface during the Zn(S,O) deposition could deteriorate the quality of the critical interface. One set of experiments was specially designed in order to test the above hypothesis.

Four ACIGS samples were chosen from the same one-stage baseline evaporation run and therefore assumed of the same quality. Sample (a) went through the standard CBD-CdS process, acting as the reference cell. Sample (b) was dipped in

the 10% HCl solution for one minute first and then had the CBD-CdS deposition similar to sample (a). The purpose of sample (b) was to test any negative effects the HCl dipping could introduce to the ACIGS absorber. Sample (c) had the Cd PE surface treatment first and then was loaded into the sputtering chamber for the Zn(S,O) sputtering deposition. After that, the sample was dipped in the HCl solution to remove the Zn(S,O) layer, and then had the CBD-CdS process to form the ACIGS / CdS junction. It's hypothesized that this procedure would preserve any damage to the absorber surface caused by the high energy plasma which would then affect the device performance with the CdS buffer. Sample (d) was processed almost in the same was as sample (c) except that the absorber surface treatment was KCN cleaning instead of Cd PE treatment.

All of the sample processing details are listed in Table 4.6 along with the device performance parameters. The corresponding JV plots are shown in Figure 4.17. The reference sample (a) showed the baseline cell performance for one-stage ACIGS / CdS device with 14.6% efficiency and V_{oc} = 615 mV. The HCl dipping demonstrated barely any influence on the ACIGS absorber quality with the final device results (b) almost the same as the reference (a). The device degradation was indeed observed from sample (c) and (d) which had received the sputtering processing. The efficiencies were about 1% less than the reference (a), which were mainly caused by the decrease in V_{oc} and FF. The results suggest that the sputtering could induce some surface damages to the absorber layer.

Table 4.6: The JV parameters of four ACIGS / CdS cells for the sputtering damage test.

Sample	Processing steps	V_{oc} mV	J_{sc} mA/cm^2	FF %	Eff %
(a)	ACIGS / CdS baseline reference	615	31.3	75.6	14.6
(b)	ACIGS HCl dip, CdS	606	32.2	74.1	14.5
(c)	ACIGS Cd PE, Zn(S,O) growth, HCl dip, CdS	585	32.5	68.6	13
(d)	ACIGS KCN clean, Zn(S,O) growth, HCl dip, CdS	598	31.8	71.7	13.6

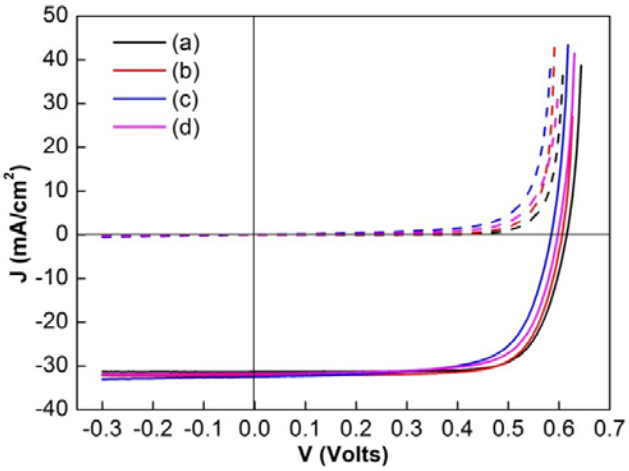

Figure 4.17: The JV plots of four ACIGS / CdS cells to test the possible sputtering damage to the absorber surface. The detailed processing steps are given in Table 4.6.

However, the device deterioration as shown in Table 4.6 was much less than the actual one-stage ACIGS / Zn(S,O) cells, which generally had the efficiency around 8% or even less and more than 100 mV V_{oc} deficit compared to the reference. One hypothesis was that the sputtering process indeed introduced damage to the absorber surface but some of the surface defect states could be eliminated in the following chemical bath for the CdS deposition. The beneficial effects of the CdS chemical bath

were illustrated in section 4.3.3. This could explain the different levels of device degradation between the cells shown in Table 4.6 and the ACIGS / Zn(S,O) cells. However, sample (c) and (d) went through several extra processing steps compared to the reference sample (a). Those extra steps could easily bring in defect states to the sensitive and critical absorber surface and result in the small V_{oc} and efficiency degradation as observed in Table 4.6 and Figure 4.17. The designed experiments here provided insight into the sputtering damage issue along with the unsatisfying behaviors of (A)CIGS / Zn(S,O) devices but stronger proofs would be needed for more confirmative conclusions.

4.3.6 Effects of Absorber Sodium Concentration

The presence of sodium in the (A)CIGS absorbers plays a critical role in achieving high efficiency devices. Although a definitive picture of the working mechanism of sodium is still incomplete, it's well accepted that sodium is involved in the passivation at the (A)CIGS film surface and along grain boundaries, which reduces the recombination current and leads to the V_{oc} improvements [23]. The SLG substrates commonly used for (A)CIGS solar cells are a source of sodium. During the high temperature growth of the absorber layer, sodium from SLG diffuses through the Mo back contact and into the bulk of (A)CIGS. The sodium diffusion process can be partly blocked by inserting a SiO_2 barrier layer between SLG and Mo, which then effectively reduces the sodium concentration in the absorbers [127].

The beneficial effects of sodium on device performance are demonstrated in Figure 4.18, where the black (a) and red (b) curves are the JV plots of two CIGS / CdS baseline devices processed in the same batch. The only difference was that sample (b) had a 1 μm thick SiO_2 sodium blocking barrier in between Mo and SLG. The

corresponding JV parameters are collected in Table 4.7. Due to the reduced sodium level in the absorber, the cell efficiency dropped and a 70 mV V_{oc} decrease was observed. The V_{oc}-T measurements were conducted to analyze the device behaviors. The derived barrier height Φ_b for sample (a) was 1.2 V, close to the bandgap of CIGS, while Φ_b =1.12 V for sample (b) was well below the E_g of the absorber. The results confirmed that the interface recombination was the main reason for the low V_{oc} performance of sample (b) [90].

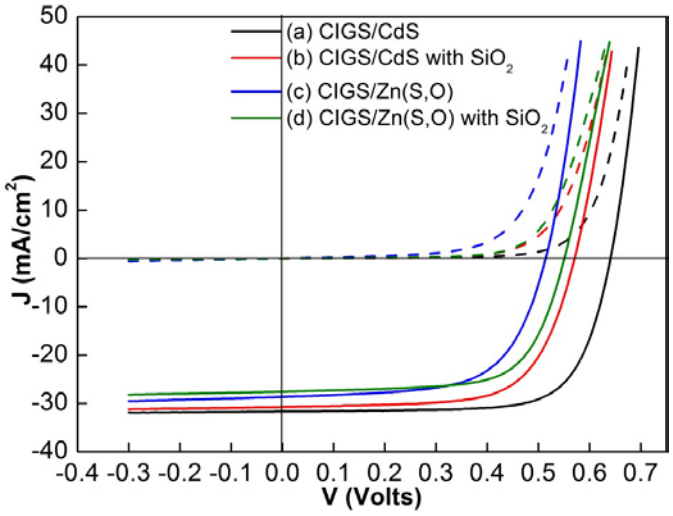

Figure 4.18: The JV plots of CIGS / CdS and CIGS / Zn(S,O) devices with and without the SiO_2 Na barrier. The solid curves are measured under one sun illumination. The dashed curves are measured in dark.

Table 4.7: JV results for CIGS / CdS and CIGS / Zn(S,O) devices with and without the SiO_2 Na barrier.

Buffer	Sample	SiO_2	V_{oc} mV	J_{sc} mA/cm^2	FF %	Eff %	Φ_b V	N_d cm^{-3}	V_b V
CdS	(a)	No	641	31.6	72.3	14.7	1.2	2E16	0.91
	(b)	Yes	571	30.7	67.0	11.8	1.12	1E15	0.28
Zn(S,O)	(c)	No	514	28.7	63.2	9.3	0.90	5E16	0.73
	(d)	Yes	551	27.6	67.7	10.3	1.12	4E14	0.28

Another device analysis technique applied here to characterize the sodium effect was the capacitance – voltage (C-V) measurements. Significant information including the minority carrier densities, potential barriers and deep trap densities can be extracted from the junction capacitance behaviors. The simple model for analysis of the space charge electrostatics can be expressed as following [91]:

$$C^{-2} = \frac{q\varepsilon N_d}{2(V+V_b)} \tag{4.3}$$

Where C is the capacitance per unit area, V is the voltage applied, q is the electron charge, ε is the dielectric constant, N_d stands for the space charge densities and V_b is the potential barrier. By fitting the plot C^{-2} vs. V with a straight line, the slope and the X axis intercept can yield the information about the free carrier density N_d and the potential barrier V_b related to the band bending.

Following the above procedure, Figure 4.19 shows the C^{-2} vs. V plot of sample (a) as one example. The experiments were conducted at 25 °C under $1*10^5$ Hz. The measurements gave $N_d = 2 \times 10^{16}$ cm^{-3}, a typical value for a well-behaved CIGS device [128], and $V_b = 0.91$V. For sample (b) the calculated $N_d = 1 \times 10^{15}$ cm^{-3}, one order of magnitude lower and $V_b = 0.28$ V. These are both characteristic features of low-sodium content absorbers [129].

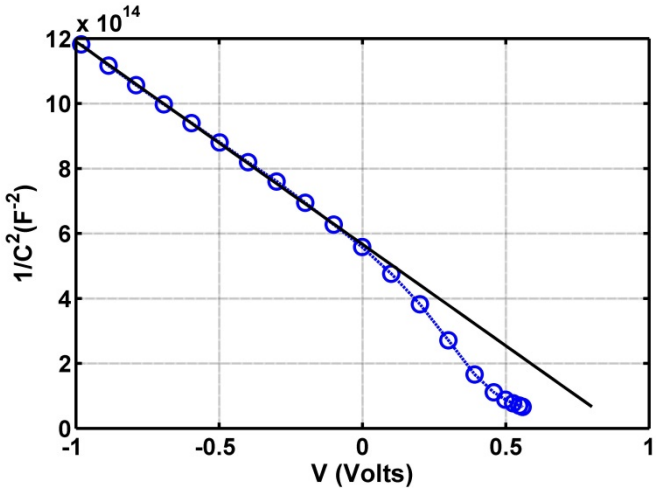

Figure 4.19: The $1/C^2$ vs. V plot of the sample (a) CIGS / CdS baseline device as listed in Table 4.7.

The story was different for CIGS devices with the sputtered Zn(S,O) buffer. It's already known that our CIGS / Zn(S,O) (sample (c)) underperformed reference cell (a) mainly due to the V_{oc} deficit, as discussed in section 4.3.2. However, when the low sodium content absorber was used (which was confirmed from the derived N_d and V_b values by CV measurements), the device efficiency and V_{oc} were enhanced slightly (sample (d)), in contrast to the case of CIGS / CdS cells. Similar phenomena were observed repeatedly and also for ACIGS / Zn(S,O) devices – the sodium content reduction in the absorber layer did not further degrade the (A)CIGS / Zn(S,O) devices, but instead produced cells with slightly better efficiencies and V_{oc}. It's suspected that sodium was involved in the already complicated absorber surface chemistry, which apparently demonstrated different properties during the CBD-CdS and the sputtering of Zn(S,O). The mystery of sodium in (A)CIGS / Zn(S,O) devices remains unresolved by this work.

4.4 Chapter Summary

Chapter 4 discusses the investigations of the sputtered Zn(S,O) alternative buffer layer on both the materials characterizations and the device applications.

The Zn(S,O) films are grown by the RF magnetron sputtering method from a $ZnO_{0.7}S_{0.3}$ compound target. The structural, compositional, and optical properties of the sputtered Zn(S,O) are studied with various characterization techniques. Zn(S,O) demonstrates low crystallinity and a wide bandgap. The composition is close to the compound target.

The sputtered Zn(S,O) films are applied in both CIGS and ACIGS devices as the alternative buffer. The champion CIGS / Zn(S,O) device has achieved 12.5% efficiency and an ACIGS / Zn(S,O) device has reached 13.2% efficiency. The device analysis reveals that the absorber / buffer interface recombination is the limiting factor of the device performance. The absorber surface treatments help to improve the cell efficiency and reproducibility. The effects of absorber processing conditions, post-device treatments, possible sputtering damage and absorber sodium content are discussed in details.

Overall our current Zn(S,O) sputtering process is not as robust as the CBD-CdS deposition, but the interesting experimental observations provide profound insights into the underlying device physics of the (A)CIGS / Zn(S,O) solar cells. The work in this chapter has paved the path for the future development and optimization of the sputtered Zn(S,O) alternative buffer.

Chapter 5

STUDY OF SUPERSTRATE CIGS SOLAR CELLS

5.1 Introduction

CIGS devices with the highest efficiencies use the substrate structure. As shown in Chapter 1, this has a configuration of glass / Mo / CIGS / buffer / i-ZnO / TCO, where the buffer layer is most commonly CdS, though many other options have been explored [130-132]. The TCO layer is typically Al- or B- doped ZnO or indium tin oxide (ITO).

The advantages of the superstrate CIGS configuration have been discussed in Chapter 1. The quality of the buffer / CIGS junction plays a vital role in the device performance. Criteria which need to be considered when selecting a suitable buffer material include the bandgap (E_g), electron affinity, conduction band alignment with the absorber, and thermodynamic stability. Previous studies of superstrate devices [133-138] have pointed out the difficulties of proper control of the buffer / CIGS junction formation. Work of the superstrate $CuInSe_2$ solar cells with CdS showed low efficiencies and speculated that the device performance was restricted by inter-diffusion between the CdS and $CuInSe_2$ [133, 134], though detailed interface characterizations to confirm this was still lacking. ZnO has been the most studied buffer material in superstrate CIGS cells and was used in the best devices to date with 12.8% efficiency after forward biasing treatment [135]. The origin of the benefits from light soaking and forward bias treatments is still under investigation. Haug [139] achieved over 11% superstrate ZnO / CIGS devices after light soaking and attributed

the substantial device improvement to the persistent photoconductivity of the bulk CIGS [140]. Ruberto and Rothwarf [141] suggested that deep defects at the interface could be saturated by charge carriers under forward bias conditions, which led to reduced interface recombination and increased V_{oc}. The effects of light soaking and bias treatments are reversible. So far the highest stable efficiency of superstrate CIGS devices with a ZnO buffer is 11.0% [142], achieved by controlled sodium delivery during the absorber growth. Another II-VI Zinc compound – ZnSe has been successfully applied in CIGS-based substrate devices [59] and our own work on CIGS / ZnSe substrate cells has been addressed in Chapter 3 [132], but no ZnSe / CIGS superstrate cells have been reported yet.

In this Chapter, three buffer materials (CdS, ZnO, ZnSe) which have all been successfully applied in the conventional CIGS substrate devices [60, 109, 143] are tested and compared in the superstrate structure. Their basic properties are listed in Chapter 1 Table 1.1. Devices with the CdS buffer have the structure of SLG / ITO / Ga_2O_3 / CdS / CIGS / Au. Devices with ZnO or ZnSe buffers have the structure of SLG / ITO / ZnO (ZnSe) / CIGS / Au. Detailed device processing steps can be found in Chapter 2. Necessary process modifications are applied in an effort to develop a well-behaved junction. Two new approaches for the buffer layers in superstrate CIGS devices are evaluated. First, the effects of $CdCl_2$ annealing treatments to crystallize and densify the CdS are studied along with reduced substrate temperature during CIGS deposition to determine if the inter-diffusion can be limited. Second, the application of ZnSe buffer is studied to determine if the common selenium anion in both ZnSe and CIGS may minimize the reaction to form undesirable phases at the junction interface. The superstrate device behaviors with the CdS, ZnSe, and ZnO

buffer materials are compared and in-depth interface characterizations are used to investigate the root causes that limit the device efficiencies.

5.2 Superstrate CdS / CIGS Solar Cells

5.2.1 Device Performance

Superstrate CdS / CIGS devices were completed with different process parameters and a summary of the representative JV results is given in Table 5.1. The highest efficiency is 4.3% and the light and dark JV curves are plotted in Figure 5.1.

Table 5.1: JV results for superstrate CdS / CIGS devices with various fabrication conditions.

#	T_{sub}* °C	CdS treat	Eff (%)	V_{OC} (mV)	J_{SC} (mA/cm^2)	FF (%)
1	550	none			Shorted	
	550	$CdCl_2$			Shorted	
2	400	none	0.7	260	10.2	26.5
	400	$CdCl_2$	1.6	313	13.8	36.1
3	350	none	3.4	434	20.7	37.9
	350	$CdCl_2$	4.3	406	25.5	41.3
4	350^+	none	0.1	86	5.1	26.9
	350^+	$CdCl_2$	0.1	53	4.4	26.0

T_{sub}* = 350^+ indicates T_{sub} = 350°C followed by a 1min in-situ post-deposition annealing at 550°C.

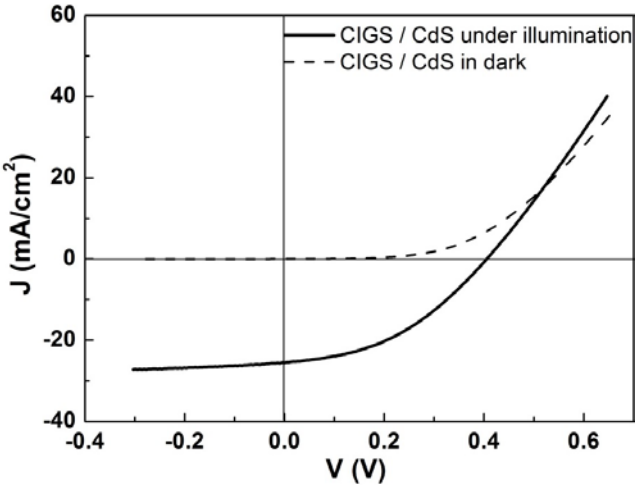

Figure 5.1: Best CdS / CIGS superstrate cell with 4.3% efficiency. The JV parameters are summarized in Table 5.1.

The primary variable explored in the absorber deposition was the substrate temperature over the range of 350°C ≤ T_{sub} ≤ 550°C where the reduced T_{sub} was intended to minimize potential intermixing between CdS and CIGS. Some CIGS runs were done at T_{sub} = 350°C and then annealed in-situ at 550°C for 1 min. Such a process was shown previously to produce absorber layers with quality as good as those grown at baseline temperature T_{sub} = 550°C [144]. The baseline single stage CIGS deposition usually produced substrate cells with ~ 15% efficiency but was catastrophic to the superstrate cells. Even 1 min post annealing at 550°C produced electrically shorted devices. The reduced absorber T_{sub} helped to improve the device performance. The best cell with 4.3% efficiency as shown in Figure 5.1 was fabricated with CIGS evaporated at T_{sub} = 350°C.

The CdS buffer processing steps were guided by our experience with CdTe solar cells [7, 87]. The CdS layer was grown by the CSD process [88] and then annealed in a parallel – plate $CdCl_2$ vapor reactor to improve its crystallinity and

stability [89]. The experimental details were illustrated in Chapter 2 section 2.3.2. The $CdCl_2$ vapor treatment helped control the inter-diffusion in CdTe superstrate devices [145]. Minor improvement was indeed observed compared to the cell without CdS – $CdCl_2$ treatment (Efficiency ~ 3.4%), in spite of the possible degradation of the absorber quality caused by Cl residue [146]. However, the merit of $CdCl_2$ vapor annealing was not validated in superstrate CIGS cells as the case with CdTe. Inter-diffusion between CdS and CIGS under process conditions cannot be prevented by this treatment as discussed below.

5.2.2 CdS / CIGS Interface Characterizations

5.2.2.1 Interface Characterization by SEM and TEM

In order to determine the causes for the poor device performance of the superstrate cells, SEM and TEM were used to characterize the buffer / CIGS interface. TEM sample preparation was done by use of the FIB to thin the specimen with Ga ion beam sputtering.

Figure 5.2 shows cross-section SEM images of two SLG / ITO / Ga_2O_3 / CdS / CIGS samples without CdS – $CdCl_2$ parallel – plate vapor treatment (a) and with the treatment (b). The two samples were prepared in the same baseline CIGS run with T_{sub} = 550°C. In both samples, the CIGS and CdS appear intermixed without a distinguishable junction. The CdS layer diffused into CIGS during the absorber growth and left behind a porous structure. Sample (a) without the CdS – $CdCl_2$ treatment exhibits more severe inter-diffusion. The CIGS grains are smaller compared to sample (b), especially near the interface, which indicates that CIGS growth was modified by CdS diffusion.

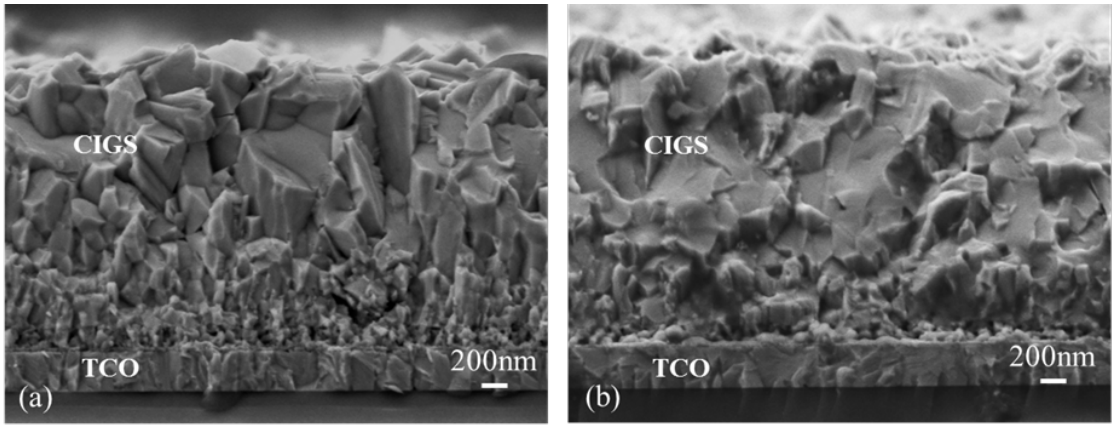

Figure 5.2: Cross-section SEM images of SLG / TCO / CdS / CIGS with baseline single stage CIGS depostion at T_{sub} = 550°C on (a) as-deposited CdS (b) CdS with parallel – plate $CdCl_2$ vapor treatment.

High resolution TEM images of the sample without CdS – $CdCl_2$ vapor annealing are presented in Figure 5.3. The bright field TEM image in Figure 5.3 (a) shows many voids (bright areas) in the interface region. Figure 5.3 (b) is the dark field STEM image of this sample. A compositional line scan measured along the white line across the critical CdS / CIGS interface by energy dispersive X-ray spectroscopy (EDS) is presented in Figure 5.3 (c). The S signal is mainly observed from 50 nm to 120 nm where the CdS layer is expected, corresponding to the dark area in Figure 5.3 (b). However, a considerable amount of Cu, In, Ga and Se are also detected in this region, suggesting the intermixing of CdS and CIGS. Strong signals of In, O, and Ga from 0 nm to 60 nm come from the window stack (ITO / Ga_2O_3). The Cd signal is very weak, probably due to the fact that it diffuses completely into the 2-μm bulk CIGS such that the concentration of Cd is too low to be detected. TEM and EDS results have shown a clear picture of the inter-diffusion issue between CIGS and CdS.

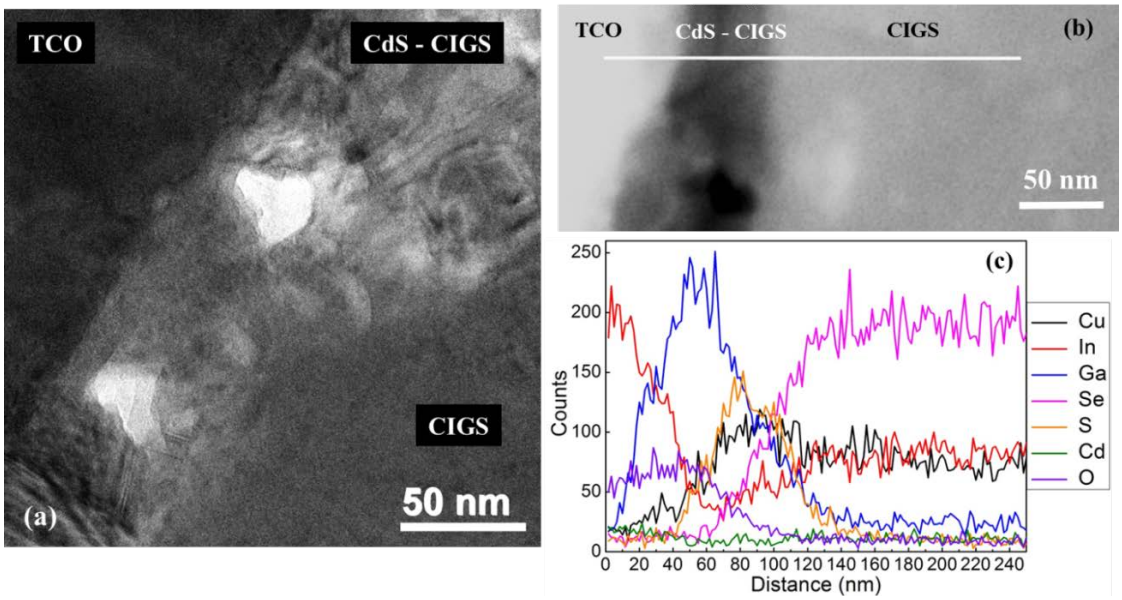

Figure 5.3: (a) High resolution TEM images of SLG / TCO / CdS / CIGS with baseline single stage CIGS depostion at T_{sub} = 550 °C. (b) STEM image of the same sample with the white line showing where the line scan EDS was measured. (c) EDS line scan results across the CdS / CIGS interface.

5.2.2.2 Interface Characterization by XPS

The buffer / absorber interface was also characterized by XPS measurements on the samples with ~ 100 nm thin absorbers where it is assumed that interface reactions would be the same as in real devices with thicker absorber layers (~ 2 μm). The XPS depth profiling was completed by repetition of the cycle of Ar sputter etching and then XPS fine scans for relevant elements. The sputter depth was calculated based upon the Ar etching rate. The integrated XPS peak intensities for each element at different depths were recorded and then normalized to the maximum value. In this way the elemental distributions from the bulk CIGS to front window layers were acquired.

Figure 5.4 shows the XPS depth profiling results for a CdS / CIGS superstrate sample. The CdS buffer in this case was annealed in $CdCl_2$ vapor and the CIGS was grown at T_{sub} = 550°C. The XPS elemental depth profiles are consistent with the EDS line scans in Figure 5.3 (c). Sulfur stays mainly at the back of the CIGS-CdS stack, accompanied by a large concentration of Cu, In, Ga and Se. Cd is detected at the surface of the CIGS and it diffuses through the entire layer. The rise of Ga and O signals from ~ 150 nm depth and In signal from ~ 180 nm depth indicates the reach of Ga_2O_3 / ITO front window layers. The CdS / CIGS inter-diffusion is also observed in other samples where lower T_{sub} has been used for the absorber deposition. Thus, XPS measurements provide solid evidence to the CdS / CIGS inter-diffusion in the superstrate configuration.

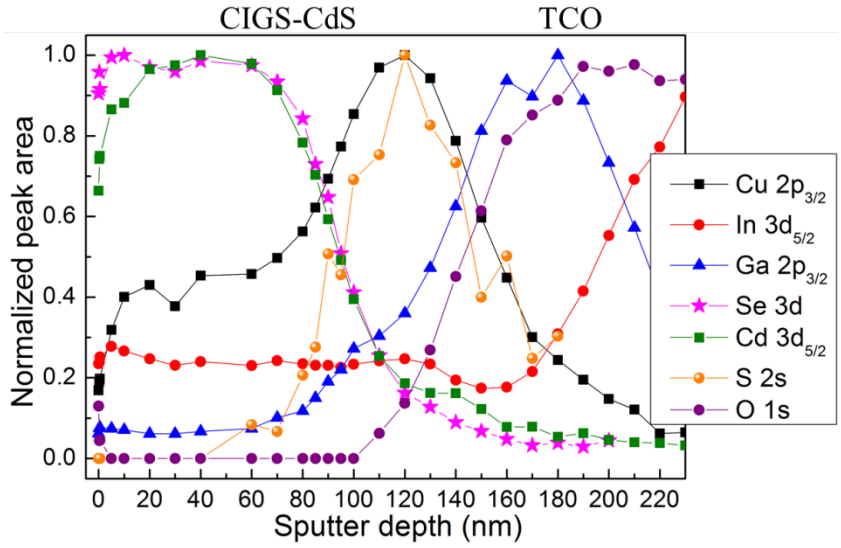

Figure 5.4: XPS depth profile measurements of the sample SLG / ITO / Ga_2O_3 / CdS / CIGS (100 nm) with the absorber layer deposited at T_{sub} = 550°C and the buffer layer annealed in $CdCl_2$ vapor.

5.3 Superstrate ZnO / CIGS Solar Cells

5.3.1 Device Performance

5.3.1.1 Effects of Deposition Conditions

Process modifications were applied to develop superstrate ZnO / CIGS cells. A summary of the device preparation conditions is shown in Table 5.2. Baseline process (sample (a)) had the ZnO sputtered at room temperature and CIGS grown at T_{sub} = 550 °C. Sample (b) aimed to improve the stability and crystallinity of the ZnO buffer layer by increasing the substrate temperature to 500 ˚C during sputtering. Sample (c) used lower CIGS growth temperature in order to reduce the thermal load during the absorber deposition. Sample (d) had the CIGS layer deposited at T_{sub} = 350°C and then annealed in-situ at 550°C for 1 min [144]. The purpose of process modifications was to prevent unfavorable interface reactions or excessive interdiffusion between ZnO and CIGS.

Table 5.2: Various deposition conditions for ZnO / CIGS superstrate devices.

	ZnO T_{sub}	**CIGS T_{sub}**	**Description**
(a)	RT	550 °C	Baseline
(b)	500 °C	550 °C	High temperature ZnO
(c)	RT	450 °C	Low temperature CIGS
(d)	RT	350 °C^{+}	1 min CIGS annealing [144]

RT: room temperature.
T_{sub} = 350°C^{+} indicates T_{sub} = 350°C followed by a 1min in-situ post-deposition annealing at 550°C.

The corresponding JV results are plotted in Figure 5.5. The overall device performance is poor. What's interesting is the shape of JV curves under different processing conditions. For sample (a) and (d) where ZnO was sputtered at room

temperature and high temperature T_{sub} = 550 °C was used for CIGS growth (even for only one minute), an s-shaped JV light curve with a kink or inflection in the fourth quadrant is observed. A kink in the JV curve can be attributed to an interface barrier for the photocurrent transport [85]. The s-shaped JV curve is not seen for sample (b) where the thermal stability of the ZnO buffer was enhanced by high temperature sputtering or for sample (c) with CIGS grown at low temperature. A ZnO buffer with better stability and lower temperature for the absorber deposition lead to less interface reaction of the ZnO / CIGS junction, which correlates closely with the device behaviors. This is further addressed in section 5.3.3.

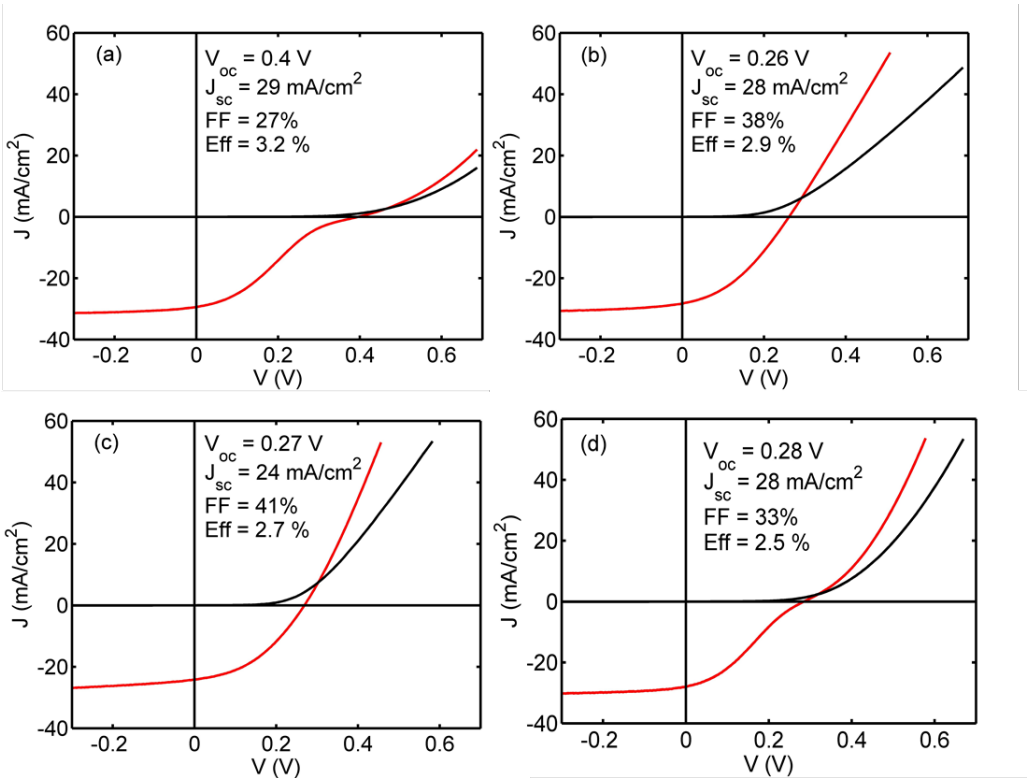

Figure 5.5: ZnO / CIGS superstrate JV results under various processing conditions which are shown in Table 5.2. The red curve is meaured under one sun illumination and the black curve is measured in dark.

5.3.1.2 Effects of Light Soaking and Forward Biasing Treatment

As stated in 5.1, light soaking and forward biasing treatments have proved to substantially enhance the ZnO / CIGS superstrate device performance. As shown in Figure 5.6 and Table 5.3 the superstrate ZnO / CIGS device efficiency is increased from 4.2% to 8.6% after light soaking under 100 mW/cm^2 illumination for a week with 1V forward bias applied at the same time. The main boosts come from V_{oc} and fill factor improvements while J_{sc} remains almost the same. Figure 5.7 gives one example of the evolutions of JV parameters vs. treatment time. The V_{oc} and efficiency jumped from less than 250 mV and 3% up to over 400 mV and 6% within the first two hours. The improvements tended to slow down afterwards. Fill factor increase shows a similar behavior. The major change occurred during the first couple of hours and then stayed stable. In contrast to above parameters, J_{sc} shows little variation- before and after the treatments.

Table 5.3: The champion ZnO / CIGS superstrate device before and after LS + FB* treatments.

	V_{oc} (mV)	**J_{sc} (mA/cm^2)**	**FF (%)**	**Eff (%)**
Before LS + FB	331	29.0	44.7	4.3
After LS + FB	493	29.5	59.3	8.6

LS + FB*: Light soaking and forward biasing treatments.

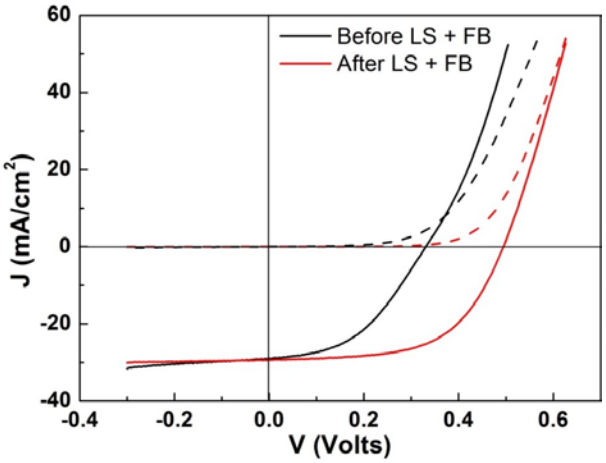

Figure 5.6: JV results of the best ZnO / CIGS superstrate device before and after the light soaking and forward biasing treatment. Solid curves are measured under one sun illumination and dash curves are measured in dark.

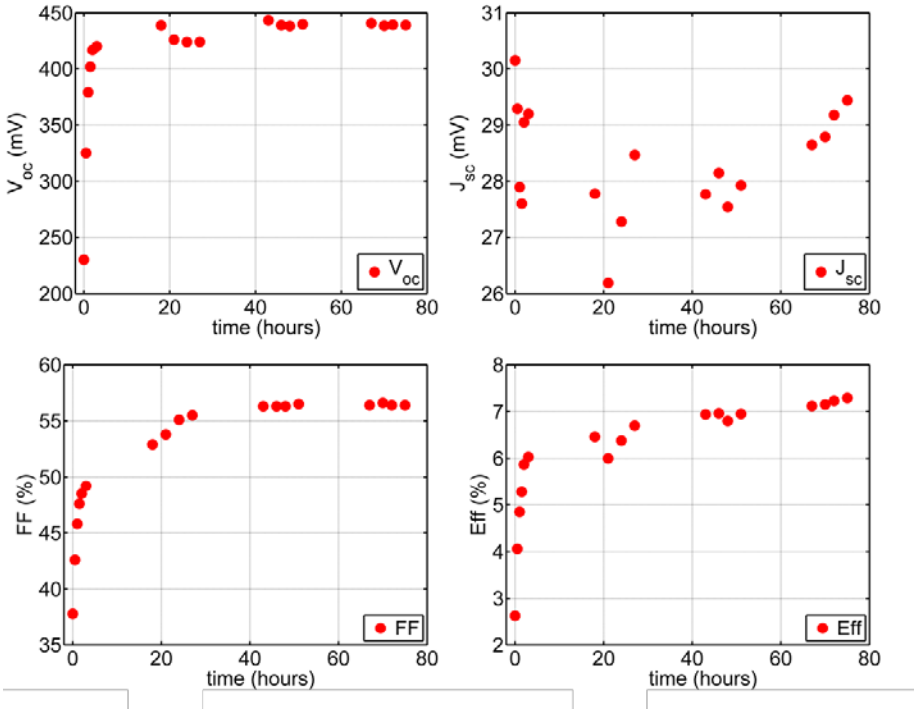

Figure 5.7: The effect of light soaking and forward biasing treatment on the JV parameters(V_{oc}, J_{sc}, FF, Eff) of one ZnO / CIGS superstrate device.

The origin of the benefits for superstrate CIGS devices from light soaking and forward biasing treatments is still under debate. Ruberto and Rothwarf [141] suggested that deep defects at the junction interface could be saturated by charge carriers under forward biasing conditions, which led to reduced interface recombination and increased V_{oc}. Recent work by Heinemann [138] claimed that forward biasing could cause the electromigration of mobile sodium and copper ions, which helped compensate defect states at the interface. Haug [139]achieved over 11% superstrate ZnO / CIGS devices after light soaking and attributed the substantial improvement under illumination to the persistent photoconductivity of the bulk CIGS [140]. The effective majority carrier density of the absorber was increased due to the light-induced capture of electrons into deep trap states in the forbidden gap [139].

Our champion ZnO / CIGS superstrate cell and world-record ZnO / CIGS superstrate cells [135, 139] cannot compete with the current development of substrate CIGS devices. The key limiting factors are the undesirable phase formation and unfavorable conduction band alignment at the ZnO / CIGS interface, as shown later in section 5.3.3.

5.3.2 ZnO / CIGS Interface Characterizations

5.3.2.1 Interface Characterization by XPS

In contrast to the case with the CdS buffer, extensive buffer – absorber inter-diffusion was not observed in the ZnO / CIGS superstrate structure based on XPS measurements. As shown in Figure 5.8, ZnO / CIGS prepared with the baseline process demonstrates a relatively sharp interface. Zn and O signals are barely detectable in the bulk CIGS region and increase dramatically at around 100 nm sputter

depth. The Ga accumulation between the CIGS and ZnO is due to gallium oxide formation as discussed later. This thin interface layer also appears to contain Cu, In and Zn.

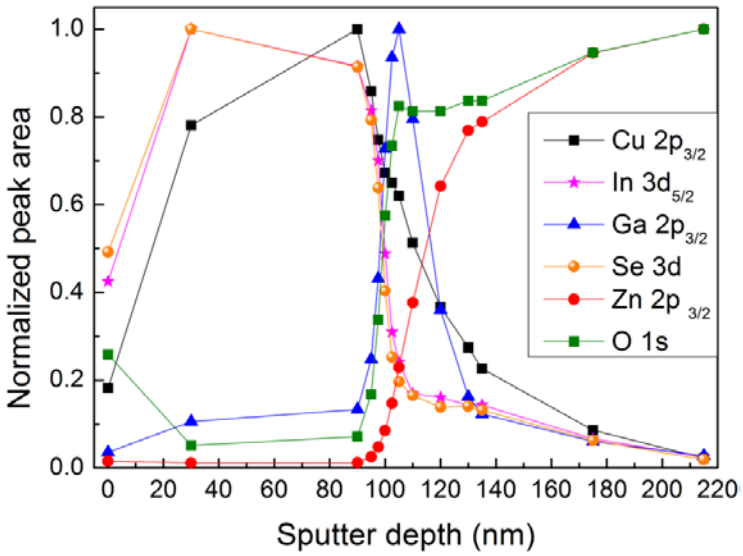

Figure 5.8: XPS depth profile measurements of the sample SLG / ITO / ZnO / CIGS (100 nm) with the absorber layer deposited at T_{sub} = 550°C and the buffer layer sputtered at T_{sub} = room temperature.

The chemical binding energy change of Ga near the ZnO / CIGS interface has been determined from XPS measurements. A series of ZnO / CIGS samples for XPS studies were prepared under the same conditions as in Table 5.2, except that the absorber layer was only about 100 nm for easier access to the junction interface by XPS Ar sputtering etching. The superstrate device behaviors in Figure 5.5 have been discussed in section 5.3.1.1. The corresponding XPS Ga 3d profiles at different etching depths (30 - 80 nm: bulk CIGS, around 100 nm: ZnO / CIGS interface region) of sample (a), (b), (c) and (d) are presented in Figure 5.9.

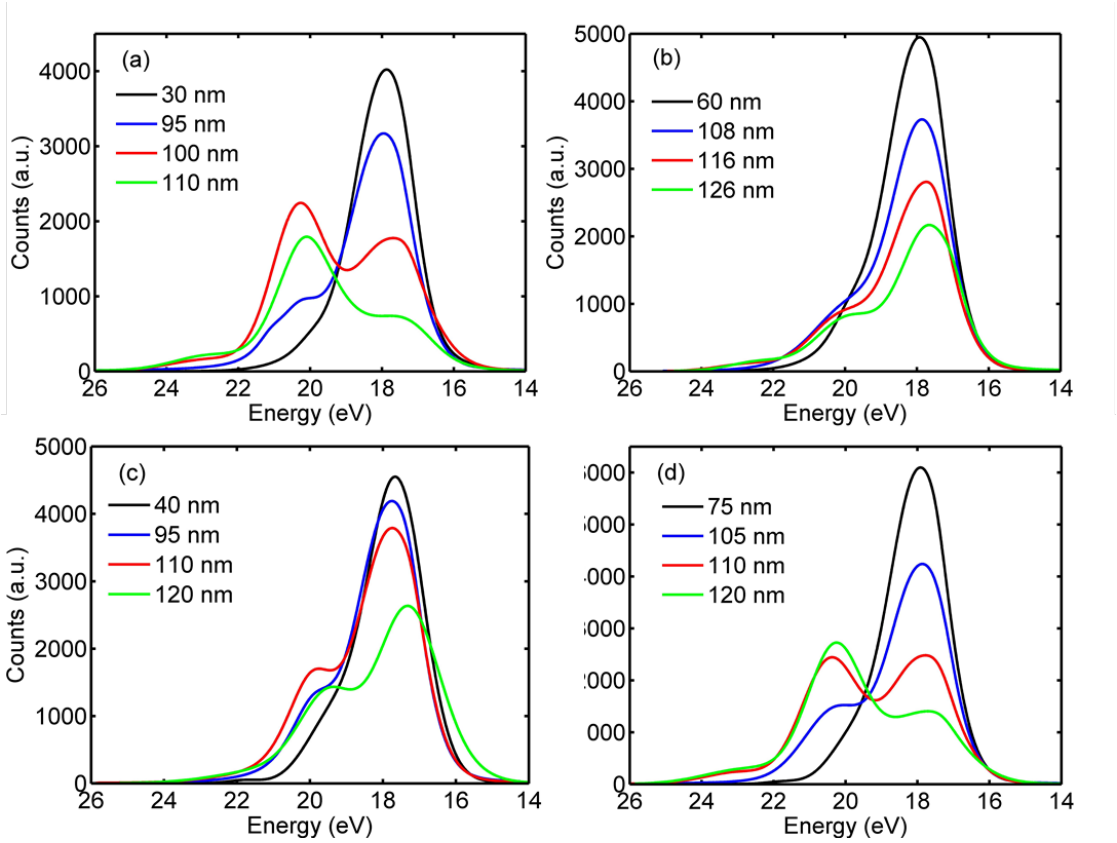

Figure 5.9: (a), (b), (c) and (d) Selected XPS spectra of the Ga3d depth profiles in the bulk of CIGS and near the ZnO /CIGS interface for samples prepared under the same conditions as in Table 5.2 (a), (b), (c) and (d), except that the CIGS layer is only about 100 nm thick.

The XPS Ga 3d spectra can be deconvoluted and fit with three Lorenzian-Gaussian components based on the binding energies: In 4d (17 eV), Ga 3d in bulk CIGS (18 eV) and Ga 3d in Ga_xO_y (20.5 eV) [84]. Figure 5.10 gives one example of how the peak fitting is conducted. The measured XPS data in this case is the blue spectrum (95 nm) in Figure 5.9 (a). For sample (a) and (d) where the ZnO was sputtered at room temperature and high temperature 550 °C was used for the CIGS deposition, the Ga 3d profile is dominated by Ga in CIGS (18eV) in the bulk CIGS.

With further Ar sputtering etch to reach the ZnO / CIGS interface around 100 nm depth, the Ga peak in CIGS drops off while the Ga 3d component attributed to Ga_xO_y increases rapidly. Similar behavior was also found in Ga LMM Auger peak profiles. This verifies the reaction between CIGS and ZnO to form Ga_xO_y at the interface, also shown from the Ga accumulation in Figure 5.8. Superstrate devices prepared under such processing conditions displayed the 's-shape' light JV curve behavior as shown in Figure 5.5 (a) and (d). For device preparation the substrates were held at the absorber growth temperature much longer. It's therefore suspected that the Ga_xO_y formation in the superstrate devices is likely to be stronger.

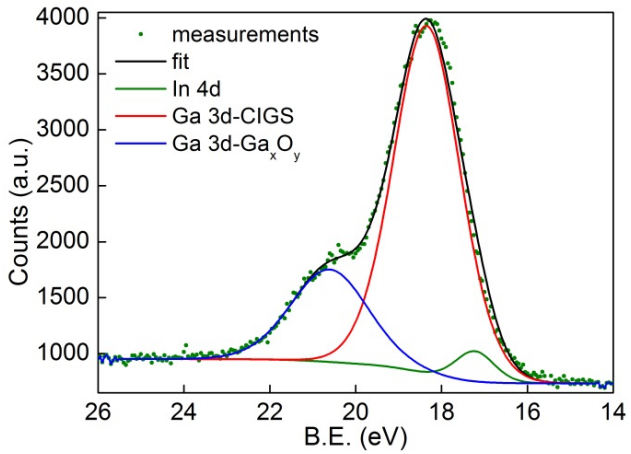

Figure 5.10: One example showing the deconvolution of XPS Ga 3d profile into three peaks – Ga 3d in bulk CIGS (18 eV), Ga 3d in Ga_xO_y (20.5 eV) and In 4d (17 eV). The spectrum is the blue curve (95 nm) in Figure 5.8 (a).

For sample (b) which used a high temperature sputtered ZnO buffer with enhanced thermal stability and sample (c) where the absorber deposition temperature was lowered to reduce the thermal load to the substrate stacks during CIGS growth,

XPS Ga 3d depth profiles revealed that the Ga_xO_y formation at the junction interface was limited, suggested by the absence of a strong well-defined peak at the binding energy around 18eV compared to the cases in (a) and (d). Concurrently, no ‘s-shape’ behavior was observed in the corresponding device JV measurements as in Figure 5.5 (b) and (c). XPS measurements demonstrate that the ZnO / CIGS interface chemistry varies with the process modifications, and correlates closely with the superstrate device behaviors.

5.3.2.2 Interface Characterization by SEM and TEM

ZnO / CIGS superstrate samples demonstrate a well-defined junction interface structure from cross-section SEM measurements, as shown in Figure 5.11 for a SLG / ITO / ZnO / CIGS sample. In this case, the ZnO buffer was sputtered at room temperature and CIGS was grown at baseline temperature T_{sub} = 550°C. The cross-section SEM image of the sample was taken during TEM specimen preparation by FIB. The inset figure shows the same interface region at higher magnification. The droplets on CIGS surface are Cu agglomerates due to preferential sputtering during FIB slicing [147]. The distinct interface between ZnO and CIGS implies that limited inter-diffusion occurs under the processing conditions.

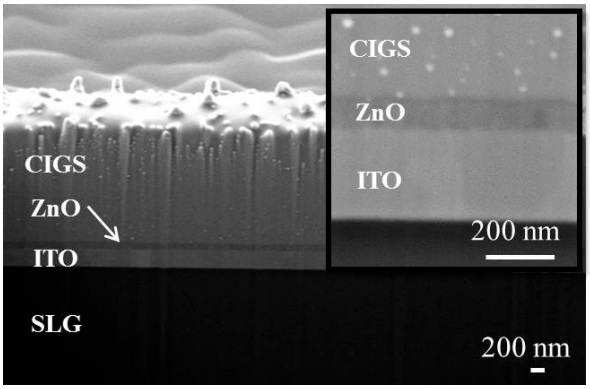

Figure 5.11: Cross-section SEM image of SLG / ITO / ZnO / CIGS with the absorber layer deposited at T_{sub}= 550 °C and the buffer layer sputtered at Tsub = room temperature. The image was taken during TEM sample preparation by FIB slicing. The inset figure shows the same interface region at higher magnification.

A closer look at the interface by high resolution TEM shows an amorphous layer of thickness 5 – 8 nm between ZnO and CIGS grains as seen in Figure 5.12. This is the Ga_xO_y layer due to the reaction between ZnO and CIGS as discussed in section 5.3.2.1. Higher ZnO sputtering temperature and lower CIGS deposition temperature can help limit the Ga_xO_y formation [137, 138, 148], and therefore affect the device performance.

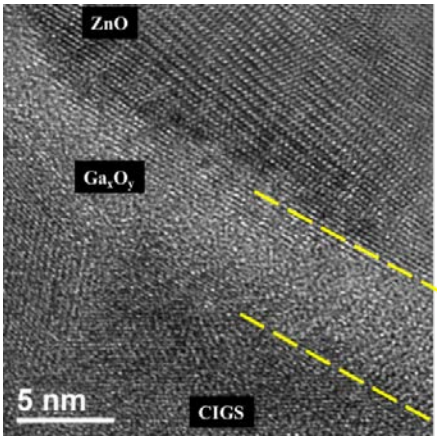

Figure 5.12: High resolution TEM image of the sample prepared under baseline conditions (ZnO sputtering at T_{sub} = room temperature and CIGS deposition at T_{sub} = 550°C) with the structure SLG / ITO / ZnO / CIGS.

5.3.3 Analysis of Device Behavior

Considering the correlation between the ZnO / CIGS superstrate device behaviors and the Ga_xO_y formation detected from XPS measurements and TEM image, it is therefore proposed that Ga_xO_y acts as a photocurrent blocking barrier at the junction interface [85, 137, 138]. Figure 5.13 shows a simple schematic of the conduction band alignment of the ZnO / CIGS junction with a Ga_xO_y layer formed in between. Band bending is not included in this case. Based on literature values [40] for the electron affinities (EA) of the CIGS, Ga_xO_y and ZnO, a spike type conduction band offset over 0.9 eV is expected between CIGS and Ga_xO_y. This barrier can severely limit the transport of the photogenerated electrons to the n-type ZnO buffer, leading to the 's-shape' in the J-V light curves. A simulation model [138] suggests that the interfacial Ga_xO_y layer is doped with Zn and Cu, consistent with our XPS depth profiles in Figure 5.8. This creates deep acceptor states and leads to the conduction band upward bending at the interface. This will introduce the electron transport

barrier. Although the Ga_xO_y formation can be reduced by process modifications, V_{oc} is still low as shown in Figure 5.5 (b) and (c), which might result from the unfavorable conduction band alignment between CIGS and ZnO [50], and electron-hole recombination caused by interface defects.

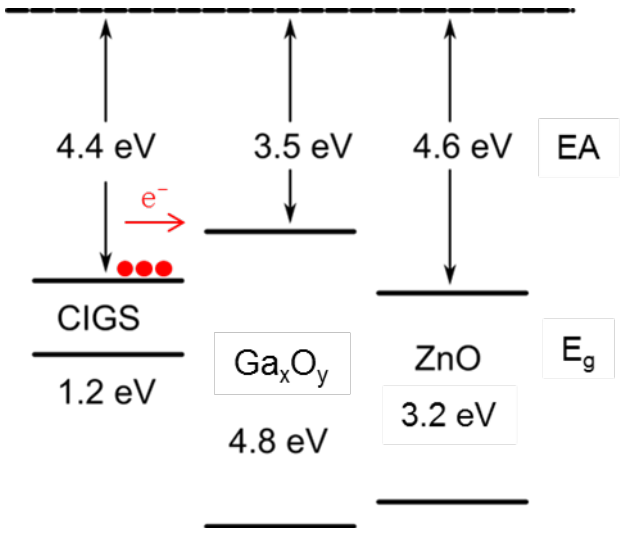

Figure 5.13: A schematic showing the conduction band alignment of the ZnO / CIGS junction with the Ga_xO_y layer in between.

5.4 Superstrate ZnSe / CIGS Solar Cells

5.4.1 Device Performance

The main merit to use ZnSe in the superstrate structure is that selenium is the constituent element for both ZnSe and CIGS so that the reaction to form undesirable phases at the junction interface under high temperature like the case with ZnO buffer can be avoided.

ZnSe buffers were deposited by RF magnetron sputtering in Ar atmosphere with no intentional substrate heating applied. The superstrate cells had the structure of

SLG / ITO / ZnSe / CIGS / Au. A range of different process conditions for both the buffer and absorber were investigated. Process modifications for the ZnSe buffer included post annealing of the sputtered ZnSe films in Ar atmosphere at 500 °C to increase the crystallinity and thermal stability, and varying the buffer thickness from 20 nm to 100 nm in the device by controlling the deposition time. Similar to the case with CdS / CIGS superstrate devices, the main variable explored in the absorber deposition was the substrate temperature over the range $350°C \leq T_{sub} \leq 550°C$ where lower deposition temperature was intended to minimize the thermal load to the substrate stack but the absorber quality sacrificed at the same time.

However, despite all those modifications the device performance was poor, with efficiency less than 4% and often severe shunting. Figure 5.14 shows the JV curves of one of the best ZnSe / CIGS superstrate device before and after one-week light soaking plus 1V forward biasing treatments. The corresponding JV parameters are summarized in Table 5.4. This cell had ZnSe buffer sputtered at room temperature and then annealed in Ar. The CIGS absorber was deposited at T_{sub} = 450 °C. The as-prepared cell was poorly behaved with only 1.4% efficiency before the light soaking and forward biasing treatments. The treatments had increased the device efficiency to 3.8% with the major improvements coming from V_{oc} and FF, but the effects were reversible. The origins of the poor device performance were investigated by a series of interface characterization techniques as discussed below.

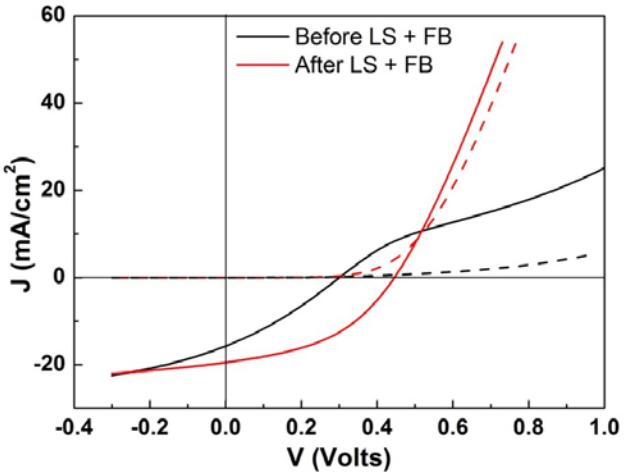

Figure 5.14: JV results of the best ZnSe / CIGS superstrate device before and after the light soaking and forward biasing treatment. Solid curves are measured under one sun illumination and dash curves are measured in dark.

Table 5.4: The ZnSe / CIGS superstrate cell before and after LS + FB treatments*

	V_{oc} (mV)	J_{sc} (mA/cm^2)	FF (%)	Eff (%)
Before LS + FB	301	15.7	29.7	1.4
After LS + FB	446	19.5	43.5	3.8

LS + FB*: Light soaking and forward biasing treatment.

5.4.2 ZnSe / CIGS Interface Characterizations

5.4.2.1 Interface Characterization by XPS

The inter-diffusion issue was again observed for a ZnSe / CIGS superstrate sample from XPS depth profiling measurements. The sample had the structure of SLG / ITO / ZnSe / CIGS (100 nm) with the absorber deposited at T_{sub} = 450°C. In Figure 5.15 the elemental depth profiles show that Zn is evenly distributed through the CIGS layer and decays along with the Cu and Se so there is no accumulation between CIGS

and ITO. Strong Zn signals can be detected at the surface of CIGS, indicating the extensive intermixing of ZnSe and CIGS. Similar behavior was observed in all ZnSe / CIGS superstrate samples with various process conditions. Ga tends to migrate to the back of CIGS which is often found in the XPS depth profiling measurements of the 100 nm – absorber samples.

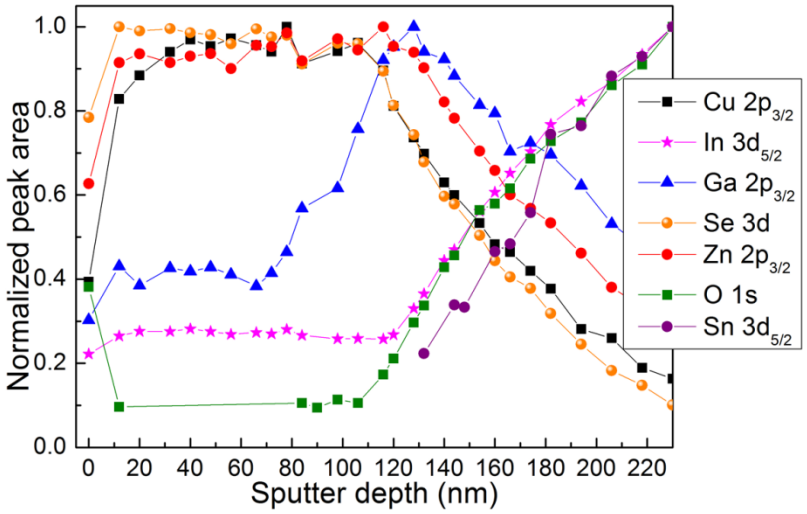

Figure 5.15: XPS depth profile measurements of the sample SLG / ITO / ZnSe / CIGS (100 nm) with the absorber layer deposited at T_{sub} = 450°C and the buffer layer sputtered at T_{sub} = room temperature.

5.4.2.2 Interface Characterization by SEM and TEM

Figure 5.16 shows the cross-section SEM image of the sample with the structure SLG / ITO / ZnSe / CIGS. The absorber was deposited at T_{sub} = 550°C. It is difficult to distinguish the interface between CIGS and ZnSe. The absorber layer has small grains near the interface region. High resolution TEM image and an elemental line scan of this sample are presented in Figure 5.17. In Figure 5.17 (a), a layer of thickness ~150 nm can be seen between ITO and CIGS. This is, however, not the

sputtered pure ZnSe anymore after the absorber growth. Figure 5.17 (b) shows the STEM image of the interface region. An EDS line scan acquired along the white line from the ITO to the absorber is plotted in Figure 5.17 (c). From the ITO / ZnSe interface to the bulk CIGS (position from 20 nm to 200 nm), Se, Cu and In are almost evenly distributed, along with a step to a slightly lower Zn concentration in the bulk CIGS, again suggesting extensive inter-diffusion of ZnSe and CIGS. The layer between ITO and CIGS as seen in Figure 5.17 (a) is now a mixture of Zn, Se, Cu, In, and Ga instead of the sputtered pure ZnSe after the absorber deposition. Due to the extensive inter-diffusion between ZnSe and CIGS, Gallium contacted the ITO window layers directly and formed gallium oxide, which explains the Ga accumulation around 20 nm. The gallium oxide formation was verified by the analysis of the Ga 3d peaks in XPS depth profiling measurements, as shown in Figure 5.18 where the Ga 3d component attributed to Ga_2O_3 (B.E. = 20.5 eV) [84] arises near the interface region.

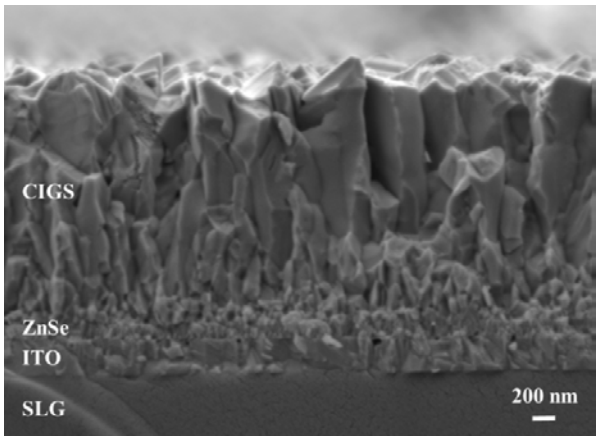

Figure 5.16: Cross-section SEM image of SLG / ITO / ZnSe / CIGS with the absorber layer deposited at T_{sub}= 550 °C and the buffer layer sputtered at T_{sub} = room temperature.

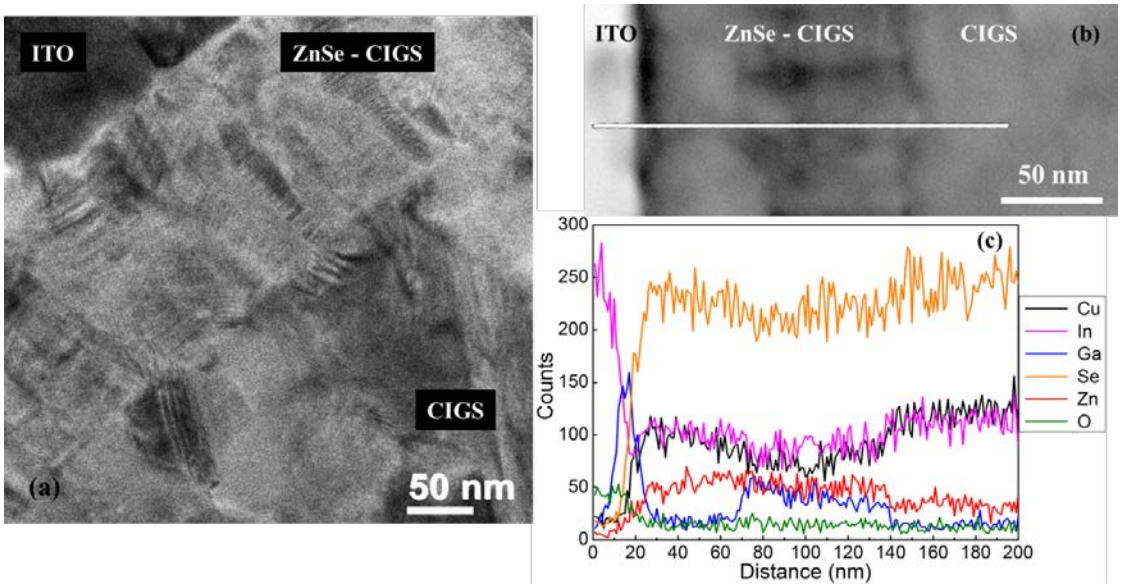

Figure 5.17: (a) High resolution TEM image of SLG / ITO / ZnSe / CIGS with baseline single stage CIGS depostion at T_{sub} = 550°C. (b). STEM image of the same sample with the white line showing where the line scan EDS was measured. (c) EDS line scan results across the interface region.

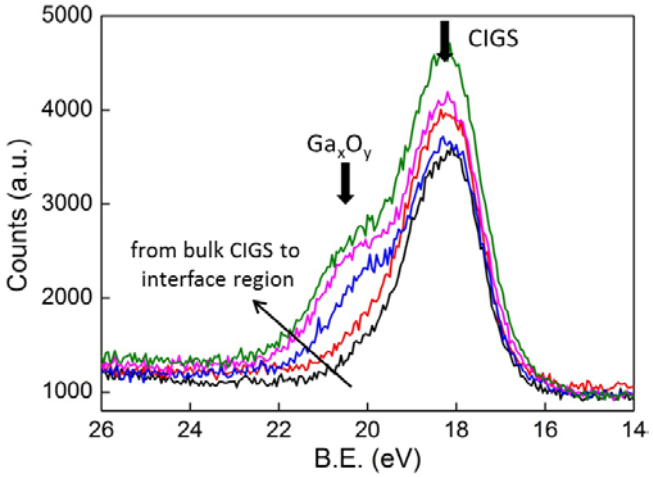

Figure 5.18: Ga 3d profiles from XPS depth profiling measurements of a SLG / ITO / ZnSe / CIGS sample.

5.5 Conclusion

We have studied the potentials and limitations of superstrate CIGS devices with three buffer options – CdS, ZnO and ZnSe. Specific problems of the superstrate cells are identified and compared by the interface studies. For CdS / CIGS superstrate devices, CdS intermixes with CIGS under the absorber growth conditions. $CdCl_2$ vapor treatment of CdS helps stabilize the buffer layer and improves the cell efficiency slightly but still cannot prevent inter-diffusion. A similar phenomenon is observed in ZnSe / CIGS superstrate cells. Inter-diffusion between the absorber and ZnSe layers severely deteriorates the junction quality and leads to poorly behaved devices, despite efforts to optimize the fabrication process. Finally, devices with ZnO buffers do not have significant inter-diffusion but Ga_xO_y formation at the interface is detected by TEM and XPS measurements. Ga_xO_y acts as a photocurrent blocking barrier and leads to an s–shaped JV curve.

Among the three buffer materials discussed above, ZnO is the most promising buffer choice for the superstrate structure. Light soaking and forward biasing treatments can significantly boost the cell efficiency but the improvements are usually reversible. The mechanisms behind the treatments still need further investigation. Intentional sodium delivery [23] to the absorber is another possible way to improve the cell efficiency as demonstrated in [138] since the window layers inhibit the out – diffusion of Na from SLG in the superstrate structure. The interface problem associated with ZnO / CIGS superstrate cells - Ga_xO_y formation can be reduced by process modifications. A recent study [149] shows that the electron affinity of Ga_xO_y is sensitive to the processing conditions, oxygen concentrations, crystallinity, dopants and so on. This could explain why the use of the Ga_2O_3 high resistance layer in CdTe solar cells did not create a blocking barrier [87]. And it also indicates that proper band

alignment between ZnO and CIGS might be achieved with further studies on better control of the gallium oxide properties.

In order to take advantage of the superstrate structure for CIGS – based solar cells, finding a suitable buffer material with required thermal, optoelectronic and band-alignment properties, as well as developing a robust fabrication process is necessary and challenging. Recently a backwall superstrate configuration was proposed [150] which could be another option for the application in a tandem structure.

Chapter 6

CONCLUSIONS AND FUTURE WORK

6.1 Conclusions

My Ph.D. research has focused on the development of Cd-free alternative buffer layer in CIGS-based thin film solar cells. Zn-compound buffer materials are chosen as the primary investigation candidates. Radio frequency (RF) magnetron sputtering is the main buffer layer deposition approach because its suitability for large-scale manufacturing is proven. The application of the Zn-compound alternative buffer layers in both substrate and superstrate CIGS-based solar cells are studied including material characterizations and device analysis.

6.1.1 Alternative Buffer Layer Development in Substrate CIGS Devices

The application of sputtered $ZnSe_{1-x}O_x$ as the buffer layer in CIGS solar cells is discussed in chapter 3. It first presents the device results and detailed analysis of CIGS / ZnSe solar cells with various Ga / (Ga+In) ratios. Device analysis reveals a conduction band spike at the CIGS / ZnSe heterojunction. Use of wider bandgap absorbers has shown a reduction of the height of this blocking barrier.

Another approach to potentially reduce the barrier height is to lower the conduction band minimum energy position of the ZnSe layer by adding oxygen. RF magnetron reactive sputtering is used to prepare $ZnSe_{1-x}O_x$ films. Detailed material characterizations include XRD, SEM, optical spectroscopies and XPS. As more oxygen is added, $ZnSe_{1-x}O_x$ is less crystallized as indicated by reduced x-ray

diffraction intensity. Bandgap values decrease at the same time, mainly by a conduction band downward shift. It's also observed that the oxygen miscibility in ZnSe lattice is very low. O / (O + Se) ratio of the $ZnSe_{1-x}O_x$ film is only around 0.06 (by XRD and optical measurements) – 0.12 (by EDS and XPS measurements) for the sample sputtered in 1% O_2 content gas mixture, and the E_g narrows by 0.2 eV. When the oxygen content is further increased, secondary phase formation has been observed. $ZnSeO_3$ formation is observed by XPS measurements and highly favorable based on thermodynamic analysis. Applications of $ZnSe_{1-x}O_x$ buffers in both CIGS and ACIGS substrate devices are also discussed.

The application of Zn(S,O) in (A)CIGS thin film solar cells as an alternative buffer layer is discussed in Chapter 4. Zn(S,O) is deposited by RF magnetron sputtering of a $ZnS_{0.3}O_{0.7}$ compound target in an Ar atmosphere and the effect of substrate temperature is characterized over the range $25°C \leq T_{sub} \leq 200$ °C. XRD measurements show that Zn(S,O) films have the wurtzite structure with increased crystallinity at elevated T_{sub}. Based on XRD and XPS measurements, the composition of the sputtered films is close to the target with S/(S+O) ratio around 0.33. Extrapolation of $(\alpha E)^2$ vs. E assuming a direct band-to-band transition gives E_g around 3.2 eV. Raman spectroscopy measurements show that Zn(S,O) exhibits a 'two-mode' phonon spectrum where the allowed optical modes of both the end binary members ZnO and ZnS are observed.

The sputtered Zn(S,O) alternative buffers are applied in both CIGS and ACIGS substrate devices. The champion CIGS / Zn(S,O) device has achieved 12.5% efficiency and ACIGS / Zn(S,O) device has reached 13.2% efficiency. Device analysis reveals that recombination at the absorber / Zn(S,O) interface limits the device

performance. The absorber surface treatments help to improve the cell efficiency and reproducibility. Zn(S,O) appears to be more sensitive to the absorber process variations and surface chemical environments compared to CdS. The effects of absorber processing conditions, post-device treatments, possible sputtering damage and absorber sodium content on the device performance are discussed in Chapter 4.

6.1.2 Alternative Buffer Layer Development in Superstrate CIGS Devices

Superstrate CIGS solar cells are prepared in the structure SLG / TCO / buffer / CIGS / Au with CIGS deposited onto the buffer layer by single stage co-evaporation process. Three buffer materials – CdS deposited by chemical surface deposition, ZnSe and ZnO by RF magnetron sputtering – are tested in the superstrate structure. The best cell achieves 8.6% efficiency with ZnO buffer after light soaking and forward bias treatments. The efficiency of devices with CdS or ZnSe buffers is less than 4%. The junction formation between the absorber and buffer layer and specific problems of the superstrate cells are identified and compared using interface studies including XPS, SEM and TEM. For ZnO / CIGS superstrate cells Ga_xO_y formation at the junction interface and unfavorable conduction band alignment are the main factors that limit the device performance. For CdS / CIGS and ZnSe / CIGS superstrate devices extensive inter-diffusion between the absorber and buffer layer under CIGS growth condition is the critical problem. Inter-diffusion severely deteriorates the junction quality and leads to poorly behaved devices, despite efforts to optimize the fabrication process.

6.2 Future Work

6.2.1 Future Work on Substrate CIGS Devices with the Alternative Buffer

$ZnSe_{1-x}O_x$ compound is an interesting material system with a lot more to explore. The effects of the sputtering parameters including the chamber pressure, the substrate temperature, and the sputtering power on the materials properties and oxygen solubility are worth more effort. As for the (A)CIGS device applications, $ZnSe_{1-x}O_x$ buffer with various oxygen concentrations should be investigated, and detailed interface characterizations of the (A)CIGS / $ZnSe_{1-x}O_x$ junction are still needed.

More effort should also be devoted to the investigations of RF sputtered Zn(S,O) alternative buffer layer in order to fully explore the potentials of this environmentally friendly material system and achieve a wider application in the manufacturing. Recommendations for future work on Zn(S,O) include:

1. In this work a $ZnS_{0.3}O_{0.7}$ target was chosen based on literature study. A wider compositional range of Zn(S,O) material system should be investigated to find out the optimal match with the (A)CIGS absorbers. This could be achieved by either using targets of various compositions or reactive sputtering of a ZnS target in O_2/Ar environment.

2. As mentioned in Chapter 4, there are still some unsolved yet important questions with (A)CIGS / Zn(S,O) solar cells, including the device reproducibility, the function of Na in the absorber bulk or at the junction interface, the working mechanism of light soaking treatment, the possible interface damage induced by buffer sputtering, etc. The above mentioned could all be interesting research topics for further development of (A)CIGS / Zn(S,O) thin film solar cells.

3. Considerable efforts have been put on CIGS device development with the sputtered Zn(S,O) buffer worldwide, but within our knowledge this project is the only one working on ACIGS / Zn(S,O) solar cells. Given the great potentials of ACIGS absorber, it's worthwhile to investigate more on the application of Zn(S,O) buffer in ACIGS devices.

6.2.2 Future Work on Superstrate CIGS Devices with the Alternative Buffer

In order to take advantage of the potential benefits of the superstrate structure for CIGS - based solar cells, finding a suitable buffer material with required thermal, optoelectronic and band-alignment properties, as well as developing a robust fabrication process is necessary and challenging. The recommendations for future work on superstrate CIGS devices are discussed below:

1. Among the three buffer materials – CdS, ZnO and ZnSe tested in the superstrate CIGS devices, ZnO is the most promising buffer option for the superstrate structure. Light soaking and forward biasing treatments have proven to significantly boost the cell efficiencies but the improvements are usually reversible. The mechanisms behind the treatments still need further investigation.

2. Intentional sodium delivery [23] to the absorber is another possible way to improve the superstrate cell efficiency as demonstrated in [138] since the window layers inhibit the out - diffusion of Na from SLG in the superstrate structure. Future study should focus on the working mechanism of sodium in the bulk CIGS and at the junction interface.

3. The interface problem associated with ZnO / CIGS superstrate cells - Ga_xO_y formation can be reduced by process modifications. A recent study [149] shows that the electron affinity of Ga_xO_y is sensitive to the processing conditions, oxygen concentrations, crystallinity, dopants and so on. And it also indicates that proper band alignment between ZnO and CIGS might be achieved with further studies to better control the gallium oxide properties.

4. We have recently proposed a backwall superstrate configuration in part to avoid the problems of interdiffusion and reaction at the absorber / buffer interface [150] The preliminary results have indicated the great promise for this structure to be used in a tandem device or with very thin absorbers. More efforts should be devoted to the backwall superstrate configuration to explore wider applications of CIGS thin film solar cells.

REFERENCES

[1] http://www.pv-magazine.com/news/details/beitrag/zsw-sets-new-thin-film-solar-world-record-with-226-efficient-cigs-pv-cell_100024995/#axzz4GNe3Mvqu.
[2] http://www.pv-magazine.com/news/details/beitrag/inside-tsmcs-165-cigs-module-world-record_100019430/#axzz4Grjj6uMO.
[3] http://www.avancis.de/en/press/news/article/avancis-erzielt-erneuten-wirkungsgradrekord-fraunhofer-ise-zertifiziert-cigs-solarmodul-mit-wirkungsgrad-von-179/.
[4] T. Wada, N. Kohara, S. Nishiwaki, T. Negami, Characterization of the Cu(In,Ga)Se_2/Mo interface in CIGS solar cells, Thin Solid Films, 387 (2001) 118-122.
[5] J. Wennerberg, J. Kessler, L. Stolt, Cu(In,Ga)Se_2-based thin-film photovoltaic modules optimized for long-term performance, Sol Energ Mat Sol C, 75 (2003) 47-55.
[6] T. Nakada, Y. Hirabayashi, T. Tokado, D. Ohmori, T. Mise, Novel device structure for Cu(In,Ga)Se_2 thin film solar cells using transparent conducting oxide back and front contacts, Solar Energy, 77 (2004) 739-747.
[7] A. Luque, S. Hegedus, Handbook of photovoltaic science and engineering, in, John Wiley & Sons, Chichester, West Sussex, U.K., 2011.
[8] M. Turcu, O. Pakma, U. Rau, Interdependence of absorber composition and recombination mechanism in Cu(In,Ga)$(Se,S)_2$ heterojunction solar cells, Appl Phys Lett, 80 (2002) 2598-2600.
[9] R. Klenk, Characterisation and modelling of chalcopyrite solar cells, Thin Solid Films, 387 (2001) 135-140.
[10] S. Siebentritt, What limits the efficiency of chalcopyrite solar cells?, Sol Energ Mat Sol C, 95 (2011) 1471-1476.
[11] C.T. Sah, R.N. Noyce, W. Shockley, Carrier Generation and Recombination in P-N Junctions and P-N Junction Characteristics, P Ire, 45 (1957) 1228-1243.
[12] M. Turcu, U. Rau, Fermi level pinning at CdS/Cu(In,Ga)$(Se,S)_2$ interfaces: effect of chalcopyrite alloy composition, J Phys Chem Solids, 64 (2003) 1591-1595.
[13] C. Persson, A. Zunger, Anomalous grain boundary physics in polycrystalline $CuInSe_2$: The existence of a hole barrier, Phys Rev Lett, 91 (2003).
[14] T. Dullweber, O. Lundberg, J. Malmstrom, M. Bodegard, L. Stolt, U. Rau, H.W. Schock, J.H. Werner, Back surface band gap gradings in Cu(In,Ga)Se_2 solar cells, Thin Solid Films, 387 (2001) 11-13.
[15] K. Kim, P. Xin, L. Yun, W.N. Shafarman, V_{OC} Enhancement of Sub-micron CIGS Solar Cells by Sulfization of the Mo Surface, in: 2015 IEEE 42nd Photovoltaic Specialist Conference (PVSC), 2015.

[16] J. Malmstrom, S. Schleussner, L. Stolt, Enhanced back reflectance and quantum efficiency in Cu(In,Ga)Se_2 thin film solar cells with a ZrN back reflector, Appl Phys Lett, 85 (2004) 2634-2636.
[17] S.B. Zhang, S.H. Wei, A. Zunger, Stabilization of ternary compounds via ordered arrays of defect pairs, Phys Rev Lett, 78 (1997) 4059-4062.
[18] S.B. Zhang, S.H. Wei, A. Zunger, H. Katayama-Yoshida, Defect physics of the $CuInSe_2$ chalcopyrite semiconductor, Phys Rev B, 57 (1998) 9642-9656.
[19] P.D. Paulson, R.W. Birkmire, W.N. Shafarman, Optical characterization of $CuIn_{1-x}Ga_xSe_2$ alloy thin films by spectroscopic ellipsometry, J Appl Phys, 94 (2003) 879-888.
[20] Y. Yan, C.S. Jiang, R. Noufi, S.H. Wei, H.R. Moutinho, M.M. Al-Jassim, Electrically benign behavior of grain boundaries in polycrystalline $CuInSe_2$ films, Phys Rev Lett, 99 (2007).
[21] J.T. Heath, J.D. Cohen, W.N. Shafarman, Bulk and metastable defects in $CuIn_{1-x}Ga_xSe_2$ thin films using drive-level capacitance profiling, J Appl Phys, 95 (2004) 1000-1010.
[22] J. Lee, J.D. Cohen, W.N. Shafarman, The determination of carrier mobilities in CIGS photovoltaic devices using high-frequency admittance measurements, Thin Solid Films, 480 (2005) 336-340.
[23] L. Kronik, D. Cahen, H.W. Schock, Effects of sodium on polycrystalline Cu(In,Ga)Se_2 and its solar cell performance, Adv Mater, 10 (1998) 31-36.
[24] P.T. Erslev, W.N. Shafarman, J.D. Cohen, Metastable properties of $Cu(In_{1-x}Ga_x)Se_2$ with and without sodium, Appl Phys Lett, 98 (2011).
[25] C.H. Henry, Limiting Efficiencies of Ideal Single and Multiple Energy-Gap Terrestrial Solar-Cells, J Appl Phys, 51 (1980) 4494-4500.
[26] J.T. Heath, J.D. Cohen, W.N. Shafarman, Defects in copper indium aluminum diselenide films and their impact on photovoltaic device performance, Mater Res Soc Symp P, 763 (2003) 441-446.
[27] B.M. Basol, A. Halani, C. Leidholm, G. Norsworthy, V.K. Kapur, A. Swartzlander, R. Matson, Studies on sulfur diffusion into Cu(In,Ga)Se_2 thin films, Prog Photovoltaics, 8 (2000) 227-235.
[28] W.N. Shafarman, R. Klenk, B.E. McCandless, Characterization of Cu(InGa)Se_2 solar cells with high Ga content, in: Conference Record of the Twenty Fifth IEEE Photovoltaic Specialists Conference, 1996, pp. 763-768.
[29] J.T. Heath, J.D. Cohen, W.N. Shafarman, D.X. Liao, A.A. Rockett, Effect of Ga content on defect states in $CuIn_{1-x}Ga_xSe_2$ photovoltaic devices, Appl Phys Lett, 80 (2002) 4540-4542.
[30] J.H. Boyle, B.E. McCandless, W.N. Shafarman, R.W. Birkmire, Structural and optical properties of (Ag,Cu)(In,Ga)Se_2 polycrystalline thin film alloys, J Appl Phys, 115 (2014).
[31] G.M. Hanket, J.H. Boyle, W.N. Shafarman, Characterization and Device Performance of (AgCu)(InGa)Se_2 Absorber Layers, in: 2009 34th IEEE Photovoltaic Specialists Conference, 2009, pp. 1962-1967.

[32] C.P. Thompson, L. Chen, W.N. Shafarman, J. Lee, S. Fields, R.W. Birkmire, Bandgap gradients in (Ag,Cu)(In,Ga)Se_2 thin film solar cells deposited by three-stage co-evaporation, in: 2015 IEEE 42nd Photovoltaic Specialist Conference (PVSC), 2015.
[33] K.P. Mitchell, R.; Ermer, J.; Wieting, R.; Eberspacher, C., High efficiency thin film tandem PV modules, in: 19th IEEE Photovoltaic Specialists Conference New York, 1987, pp. 13-18.
[34] R.L. Anderson, Experiments on Ge-GaAs Heterojunctions, Solid State Electron, 5 (1962) 341-351.
[35] A. Chirilă, S. Buecheler, F. Pianezzi, P. Bloesch, C. Gretener, A.R. Uhl, C. Fella, L. Kranz, J. Perrenoud, S. Seyrling, Highly efficient Cu(In,Ga)Se_2 solar cells grown on flexible polymer films, Nature Materials, 10 (2011) 857-861.
[36] T. Minemoto, T. Matsui, H. Takakura, Y. Hamakawa, T. Negami, Y. Hashimoto, T. Uenoyama, M. Kitagawa, Theoretical analysis of the effect of conduction band offset of window/CIS layers on performance of CIS solar cells using device simulation, Sol Energ Mat Sol C, 67 (2001) 83-88.
[37] A. Niemegeers, M. Burgelman, A. Devos, On the CdS/$CuInSe_2$ Conduction Band Discontinuity, Appl Phys Lett, 67 (1995) 843-845.
[38] O. Knacke, O. Kubaschewski, K. Hesselmann, Thermochemical properties of inorganic substances, 2nd ed., Springer-Verlag Berlin ; New York, 1991.
[39] R. Scheer, Towards an electronic model for $CuIn_{1-x}Ga_xSe_2$ solar cells, Thin Solid Films, 519 (2011) 7472-7475.
[40] J. Robertson, B. Falabretti, Band offsets of high K gate oxides on III-V semiconductors, J Appl Phys, 100 (2006).
[41] T. Homann, U. Hotje, M. Binnewies, A. Börger, K.-D. Becker, T. Bredow, Composition-dependent band gap in ZnS_xSe_{1-x}: a combined experimental and theoretical study, Solid State Sciences, 8 (2006) 44-49.
[42] R. Swank, Surface Properties of II-VI Compounds, Physical Review, 153 (1967) 844-849.
[43] R. Jayakrishnan, T. Sebastian, T.T. John, C.S. Kartha, K.P. Vijayakumar, Photoconductivity in sprayed beta-In_2S_3 thin films under sub-band-gap excitation of 1.96 eV, J Appl Phys, 102 (2007).
[44] D. Schmid, M. Ruckh, F. Grunwald, H.W. Schock, Chalcopyrite / Defect Chalcopyrite Heterojunctions on the Basis of $CuInSe_2$, J Appl Phys, 73 (1993) 2902-2909.
[45] D.X. Liao, A. Rockett, Cd doping at the $CuInSe_2$/CdS heterojunction, J Appl Phys, 93 (2003) 9380-9382.
[46] M. Mushrush, T. Bryden, R. Feist, S. Rozeveld, G. Mitchell, J. Fenton, Development of a High-Pressure CdS Sputtering Process for Improved Efficiency in CIGS-Based Photovoltaic Devices, 2012 38th IEEE Photovoltaic Specialists Conference (PVSC), (2012) 895-898.

[47] D. Abou-Ras, G. Kostorz, A. Romeo, D. Rudmann, A. Tiwari, Structural and chemical investigations of CBD- and PVD-CdS buffer layers and interfaces in Cu(In,Ga)Se_2-based thin film solar cells, Thin Solid Films, 480 (2005) 118-123.
[48] K. Orgassa, U. Rau, Q. Nguyen, H. Werner Schock, J.H. Werner, Role of the CdS buffer layer as an active optical element in Cu(In,Ga)Se_2 thin-film solar cells, Progress in Photovoltaics: Research and Applications, 10 (2002) 457-463.
[49] T. Minemoto, T. Negami, S. Nishiwaki, H. Takakura, Y. Hamakawa, Preparation of $Zn_{1-x}Mg_xO$ films by radio frequency magnetron sputtering, Thin Solid Films, 372 (2000) 173-176.
[50] T. Minemoto, Y. Hashimoto, T. Satoh, T. Negami, H. Takakura, Y. Hamakawa, Cu(In,Ga)Se_2 solar cells with controlled conduction band offset of window/Cu(In,Ga)Se_2 layers, J Appl Phys, 89 (2001) 8327-8330.
[51] D. Hariskos, R. Menner, P. Jackson, S. Paetel, W. Witte, W. Wischmann, M. Powalla, L. Burkert, T. Kolb, M. Oertel, B. Dimmler, B. Fuchs, New reaction kinetics for a high-rate chemical bath deposition of the Zn(S,O) buffer layer for Cu(In,Ga)Se_2-based solar cells, Prog Photovoltaics, 20 (2012) 534-542.
[52] M.A. Contreras, T. Nakada, M. Hongo, A.O. Pudov, J.R. Sites, ZnO/ZnS(O,OH)/Cu(In,Ga)Se_2/Mo solar cell with 18.6% efficiency, in: Proceedings of 3rd World Conference on Photovoltaic Energy Conversion, 2003, pp. 570-573.
[53] T. Nakada, M. Mizutani, Y. Hagiwara, A. Kunioka, High-efficiency Cu(In,Ga)Se_2 thin-film solar cells with a CBD-ZnS buffer layer, Sol Energ Mat Sol C, 67 (2001) 255-260.
[54] C. Platzer-Bjorkman, T. Torndahl, D. Abou-Ras, J. Malmstrom, J. Kessler, L. Stolt, Zn(O,S) buffer layers by atomic layer deposition in Cu(In,Ga)Se_2 based thin film solar cells: Band alignment and sulfur gradient, J Appl Phys, 100 (2006).
[55] M.M. Islam, S. Ishizuka, A. Yamada, K. Sakurai, S. Niki, T. Sakurai, K. Akimoto, CIGS solar cell with MBE-grown ZnS buffer layer, Sol Energ Mat Sol C, 93 (2009) 970-972.
[56] R. Klenk, A. Steigert, T. Rissom, D. Greiner, C.A. Kaufmann, T. Unold, M.C. Lux-Steiner, Junction formation by Zn(O,S) sputtering yields CIGSe-based cells with efficiencies exceeding 18%, Prog Photovoltaics, 22 (2014) 161-165.
[57] W. Eisele, A. Ennaoui, P. Schubert-Bischoff, M. Giersig, C. Pettenkofer, J. Krauser, M. Lux-Steiner, S. Zweigart, F. Karg, XPS, TEM and NRA investigations of Zn(Se,OH)/$Zn(OH)_2$ films on Cu(In,Ga)$(S,Se)_2$ substrates for highly efficient solar cells, Sol Energ Mat Sol C, 75 (2003) 17-26.
[58] A. Ennaoui, S. Siebentritt, M.C. Lux-Steiner, W. Riedl, F. Karg, High-efficiency Cd-free CIGSS thin-film solar cells with solution grown zinc compound buffer layers, Sol Energ Mat Sol C, 67 (2001) 31-40.
[59] S. Siebentritt, P. Walk, U. Fiedeler, I. Lauermann, K. Rahne, M.C. Lux-Steiner, T.P. Niesen, F. Karg, MOCVD as a dry deposition method of ZnSe buffers for Cu(In,Ga)$(S,Se)_2$ solar cells, Prog Photovoltaics, 12 (2004) 333-338.

[60] Y. Ohtake, K. Kushiya, M. Ichikawa, A. Yamada, M. Konagai, Polycrystalline Cu(InGa)Se_2 thin-film solar cells with ZnSe buffer layers, Japanese Journal of Applied Physics 34 (1995) 5949-5955.
[61] N. Naghavi, S. Spiering, M. Powalla, B. Cavana, D. Lincot, High-efficiency copper indium gallium diselenide (CIGS) solar cells with indium sulfide buffer layers deposited by atomic layer chemical vapor deposition (ALCVD), Prog Photovoltaics, 11 (2003) 437-443.
[62] N.A. Allsop, A. Schonmann, H.J. Muffler, M. Bar, M.C. Lux-Steiner, C.H. Fischer, Spray-ILGAR indium sulfide buffers for Cu(In, Ga)(S, $Se)_2$ solar cells, Prog Photovoltaics, 13 (2005) 607-616.
[63] S. Gall, N. Barreau, F. Jacob, S. Harel, J. Kessler, Influence of sodium compounds at the Cu(In,Ga)Se_2/(PVD) In_2S_3 interface on solar cell properties, Thin Solid Films, 515 (2007) 6076-6079.
[64] P. Pistor, R. Caballero, D. Hariskos, V. Izquierdo-Roca, R. Wachter, S. Schorr, R. Klenk, Quality and stability of compound indium sulphide as source material for buffer layers in Cu(In,Ga)Se_2 solar cells, Sol Energ Mat Sol C, 93 (2009) 148-152.
[65] S. Buecheler, D. Corica, D. Guettler, A. Chirila, R. Verma, U. Muller, T.P. Niesen, J. Palm, A.N. Tiwari, Ultrasonically sprayed indium sulfide buffer layers for Cu(In,Ga)(S,$Se)_2$ thin-film solar cells, Thin Solid Films, 517 (2009) 2312-2315.
[66] G.I. Rusu, M. Diciu, C. Pîrghie, E.M. Popa, Structural characterization and optical properties of ZnSe thin films, Applied Surface Science, 253 (2007) 9500-9505.
[67] A.J. Nelson, C.R. Schwerdtfeger, S.-H. Wei, A. Zunger, D. Rioux, R. Patel, H. Höchst, Theoretical and experimental studies of the ZnSe/$CuInSe_2$ heterojunction band offset, Appl Phys Lett, 62 (1993) 2557.
[68] C. Persson, C. Platzer-Bjorkman, J. Malmstrom, T. Torndahl, M. Edoff, Strong valence-band offset bowing of $ZnO_{1-x}S_x$ enhances p-type nitrogen doping of ZnO-like alloys, Phys Rev Lett, 97 (2006).
[69] http://www.solar-frontier.com/eng/news/2015/C051171.html.
[70] M. Ohring, Materials science of thin films, Academic press, 2001.
[71] M.K. Kiyotaka Wasa, and Hideaki Adachi, Thin Film Materials Technology: Sputtering of Compound Materials, Springer Science & Business Media, 2004.
[72] M. Gossla, W.N. Shafarman, Five-source PVD for the deposition of Cu($In_{1-x}Ga_x$)($Se_{1-y}S_y$)$_2$ absorber layers, Thin Solid Films, 480 (2005) 33-36.
[73] R. Scheer, T. Walter, H.W. Schock, M.L. Fearheiley, H.J. Lewerenz, $CuInS_2$ Based Thin Film Solar Cell with 10.2% Efficiency, Appl Phys Lett, 63 (1993) 3294-3296.
[74] S. Niki, M. Contreras, I. Repins, M. Powalla, K. Kushiya, S. Ishizuka, K. Matsubara, CIGS absorbers and processes, Prog Photovoltaics, 18 (2010) 453-466.
[75] J. Kessler, M. Bodegard, J. Hedstrom, L. Stolt, Baseline Cu(In,Ga)Se_2 device production: Control and statistical significance, Sol Energ Mat Sol C, 67 (2001) 67-76.

[76] R. Klenk, T. Walter, H.W. Schock, D. Cahen, A Model for the Successful Growth of Polycrystalline Films of $CuInSe_2$ by Multisource Physical Vacuum Evaporation, Adv Mater, 5 (1993) 114-119.
[77] W.N. Shafarman, J. Zhu, Effect of substrate temperature and depostion profile on evaporated $Cu(InGa)Se_2$ films and devices, Thin Solid Films, 361 (2000) 473-477.
[78] K. Ramanathan, M.A. Contreras, C.L. Perkins, S. Asher, F.S. Hasoon, J. Keane, D. Young, M. Romero, W. Metzger, R. Noufi, J. Ward, A. Duda, Properties of 19.2% efficiency $ZnO/CdS/CuInGaSe_2$ thin-film solar cells, Prog Photovoltaics, 11 (2003) 225-230.
[79] W.N. Shafarman, R. Klenk, B.E. McCandless, Device and material characterization of $Cu(InGa)Se_2$ solar cells with increasing band gap, J Appl Phys, 79 (1996) 7324-7328.
[80] P.T. Erslev, J. Lee, G.M. Hanket, W.N. Shafarman, J.D. Cohen, The electronic structure of $Cu(In_{1-x}Ga_x)Se_2$ alloyed with silver, Thin Solid Films, 519 (2011) 7296-7299.
[81] D. Abou-Ras, T. Kirchartz, U. Rau, Advanced characterization techniques for thin film solar cells, in, Wiley-VCH,, Weinheim, Germany, 2011, pp. 1 online resource (xxxvi, 547 p.).
[82] B.E. McCandless, Glancing incidence x-ray diffraction of polycrystalline thin films, in: MRS proceedings, 2005, pp. 75-86.
[83] J.I. Pankove, Optical processes in semiconductors, Dover, New York, 1975.
[84] C.D. Wagner, W.M. Riggs, L.E. Davis, J.F. Moulder, G.E. Muilenberg, Handbook of X-ray photoelectron spectroscopy, Perkin-Elmer, Eden Prairie, MN 1979.
[85] R. Scheer, H.W. Schock, Chalcogenide photovoltaics : physics, technologies, and thin film devices, John Wiley distributor, Weinheim, Germany, 2011.
[86] I. Kaur, D.K. Pandya, K.L. Chopra, Growth Kinetics and Polymorphism of Chemically Deposited CdS Films, J Electrochem Soc, 127 (1980) 943-948.
[87] B.E. McCandless, K.D. Dobson, Processing options for CdTe thin film solar cells, Solar Energy, 77 (2004) 839-856.
[88] B.E. McCandless, W.N. Shafarman, Chemical surface deposition of ultra-thin cadmium sulfide films for high performance and high cadmium utilization, in: Proceedings of 3rd World Conference on Photovoltaic Energy Conversion, 2003, pp. 562-565.
[89] B.E. McCandless, R.W. Birkmire, Influence of window and absorber layer processing on device operation in superstrate thin film CdTe solar cells, in: Conference Record of the Twenty-Eighth Ieee Photovoltaic Specialists Conference, 2000, pp. 491-494.
[90] C.P. Thompson, S. Hegedus, W. Shafarman, D. Desai, Temperature dependence of V_{oc} in CdTe and $Cu(InGa)(SeS)_2$-based solar cells, in: PVSC: 2008 33rd IEEE Photovoltaic Specialists Conference, 2008, pp. 788-793.
[91] S.S. Hegedus, W.N. Shafarman, Thin-film solar cells: Device measurements and analysis, Prog Photovoltaics, 12 (2004) 155-176.

[92] A. Bauknecht, U. Blieske, T. Kampschulte, J. Albert, H. Sehnert, M.C. Lux-Steiner, A. Klein, W. Jaegermann, Band offsets at the ZnSe/$CuGaSe_2$(001) heterointerface, Appl Phys Lett, 74 (1999) 1099.
[93] J. Ihm, M.L. Cohen, Self-Consistent Calculation of the Electronic Structure of the (110) GaAs-ZnSe Interface, Phys Rev B, 20 (1979) 729-733.
[94] S.H. Wei, S.B. Zhang, A. Zunger, Effects of Ga addition to $CuInSe_2$ on its electronic, structural, and defect properties, Appl Phys Lett, 72 (1998) 3199-3201.
[95] J.B. Li, S.H. Wei, Alignment of isovalent impurity levels: Oxygen impurity in II-VI semiconductors, Phys Rev B, 73 (2006).
[96] W. Shan, W. Walukiewicz, J.W. Ager, K.M. Yu, J. Wu, E.E. Haller, Y. Nabetani, T. Mukawa, Y. Ito, T. Matsumoto, Effect of oxygen on the electronic band structure in ZnO_xSe_{1-x} alloys, Appl Phys Lett, 83 (2003) 299-301.
[97] C.Y. Moon, S.H. Wei, Y.Z. Zhu, G.D. Chen, Band-gap bowing coefficients in large size-mismatched II-VI alloys: first-principles calculations, Phys Rev B, 74 (2006).
[98] R. Broesler, E.E. Haller, W. Walukiewicz, T. Muranaka, T. Matsumoto, Y. Nabetani, Temperature dependence of the band gap of $ZnSe_{1-x}O_x$, Appl Phys Lett, 95 (2009).
[99] Y. Nabetani, T. Mukawa, Y. Ito, T. Kato, T. Matsumoto, Epitaxial growth and large band-gap bowing of ZnSeO alloy, Appl Phys Lett, 83 (2003) 1148-1150.
[100] C.Y. Chen, C.Y. Yang, J.I. Chyi, C.H. Wu, Optical and electrical properties of ZnSeO alloys grown by plasma-assisted molecular beam epitaxy, J Cryst Growth, 378 (2013) 180-183.
[101] M.A. Mayer, D.T. Speaks, K.M. Yu, S.S. Mao, E.E. Haller, W. Walukiewicz, Band structure engineering of $ZnO_{1-x}Se_x$ alloys, Appl Phys Lett, 97 (2010).
[102] K. Ramanathan, R.N. Bhattacharya, J. Granata, J. Webb, D. Niles, M.A. Contreras, H. Wiesner, F.S. Hasoon, R. Noufi, Advances in the CIS research at NREL, in: Conference Record of the Twenty Sixth IEEE Photovoltaic Specialists Conference, 1997, pp. 319-322.
[103] M. Ashraf, S.M.J. Akhtar, A.F. Khan, Z. Ali, A. Qayyum, Effect of annealing on structural and optoelectronic properties of nanostructured ZnSe thin films, J Alloy Compd, 509 (2011) 2414-2419.
[104] A. Walsh, J.L.F. Da Silva, S.H. Wei, C. Korber, A. Klein, L.F.J. Piper, A. DeMasi, K.E. Smith, G. Panaccione, P. Torelli, D.J. Payne, A. Bourlange, R.G. Egdell, Nature of the band gap of In_2O_3 revealed by first-principles calculations and x-ray spectroscopy, Phys Rev Lett, 100 (2008).
[105] A.B.M.A. Ashrafi, A. Ueta, A. Avramescu, H. Kumano, I. Suemune, Y.W. Ok, T.Y. Seong, Growth and characterization of hypothetical zinc-blende ZnO films on GaAs(001) substrates with ZnS buffer layers, Appl Phys Lett, 76 (2000) 550-552.
[106] U. Weser, G. Sokolowski, W. Pilz, Reaction of Selenite with Biochemically Active Thiols - X-Ray Photoelectron Spectroscopic Study, J Electron Spectrosc, 10 (1977) 429-439.

[107] C.D. Wagner, D.A. Zatko, R.H. Raymond, Use of the Oxygen Kll Auger Lines in Identification of Surface Chemical-States by Electron-Spectroscopy for Chemical-Analysis, Anal Chem, 52 (1980) 1445-1451.
[108] V. Tomashyk, P. Feychuk, L. Shcherbak, Ternary alloys based on II-VI semiconductor compounds, CRC Press, 2013.
[109] C. Platzer-Bjorkman, J. Lu, J. Kessler, L. Stolt, Interface study of $CuInSe_2$/ZnO and $Cu(In,Ga)Se_2$/ZnO devices using ALD ZnO buffer layers, Thin Solid Films, 431 (2003) 321-325.
[110] B.K. Meyer, A. Polity, B. Farangis, Y. He, D. Hasselkamp, T. Kramer, C. Wang, Structural properties and bandgap bowing of $ZnO_{1-x}S_x$ thin films deposited by reactive sputtering, Appl Phys Lett, 85 (2004) 4929-4931.
[111] A. Grimm, D. Kieven, I. Lauermann, M. Lux-Steiner, F. Hergert, R. Schiwieger, R. Klenk, Zn(O,S) layers for chalcopyrite solar cells sputtered from a single target, in: EPJ Photovoltaics, 2012, pp. 30302.
[112] I.F. Chang, S.S. Mitra, Application of a Modified Random-Element-Isodisplacement Model to Long-Wavelength Optic Phonons of Mixed Crystals, Physical Review, 172 (1968) 924-&.
[113] A. Polity, B.K. Meyer, T. Kramer, C.Z. Wang, U. Haboeck, A. Hoffmann, ZnO based ternary transparent conductors, Phys Status Solidi A, 203 (2006) 2867-2872.
[114] F. Decremps, J. Pellicer-Porres, A.M. Saitta, J.C. Chervin, A. Polian, High-pressure Raman spectroscopy study of wurtzite ZnO, Phys Rev B, 65 (2002).
[115] T.C. Damen, S.P.S. Porto, B. Tell, Raman Effect in Zinc Oxide, Physical Review, 142 (1966) 570-571.
[116] Y.C. Cheng, C.Q. Jin, F. Gao, X.L. Wu, W. Zhong, S.H. Li, P.K. Chu, Raman scattering study of zinc blende and wurtzite ZnS, J Appl Phys, 106 (2009).
[117] O. Brafman, S.S. Mitra, Raman Effect in Wurtzite- and Zinc-Blende-Type ZnS Single Crystals, Physical Review, 171 (1968) 931-932.
[118] Y.B. He, L. Zhang, L.H. Wang, M.K. Li, X.Z. Shang, X. Liu, Y.M. Lu, B.K. Meyer, Structural and optical properties of single-phase $ZnO_{1-x}S_x$ alloy films epitaxially grown by pulsed laser deposition, J Alloy Compd, 587 (2014) 369-373.
[119] Y. Hashimoto, N. Kohara, T. Negami, M. Nishitani, T. Wada, Surface characterization of chemically treated $Cu(In,Ga)Se_2$ thin films, Japanese Journal of Applied Physics, 35 (1996) 4760-4764.
[120] L. Weinhardt, O. Fuchs, D. Gross, E. Umbach, C. Heske, N.G. Dhere, A.A. Kadam, S.S. Kulkarni, Surface modifications of $Cu(In,Ga)S_2$ thin film solar cell absorbers by KCN and H_2O_2/H_2SO_4 treatments, J Appl Phys, 100 (2006).
[121] U. Rau, D. Braunger, R. Herberholz, H.W. Schock, J.F. Guillemoles, L. Kronik, D. Cahen, Oxygenation and air-annealing effects on the electronic properties of $Cu(In,Ga)Se_2$ films and devices, J Appl Phys, 86 (1999) 497-505.
[122] A. Rockett, Surface analysis of chalcopyrite materials for photovoltaics, Prog Photovoltaics, 20 (2012) 575-581.
[123] K. Ramanathan, H. Wiesner, S. Asher, D. Niles, R.N. Bhattacharya, M. Contreras, R. Noufi, High-Efficiency $Cu(In,Ga)Se_2$ Thin Film Solar Cells Without

Intermediate Buffer Layers, in: 2nd World Conference and Exhibition on Photovoltaic Solar Energy Conversion, Vienna, Austria, 1998.
[124] S.S. Schmidt, D. Abou-Ras, T. Unold, T. Eisenbarth, H. Wilhelm, A. Grimm, J. Klaer, H.W. Schock, Effect of Zn incorporation into $CuInS_2$ solar cell absorbers on microstructural and electrical properties, J Appl Phys, 110 (2011).
[125] T. Kobayashi, Z.J. Li Kao, T. Nakada, Temperature dependent current-voltage and admittance spectroscopy on heat-light soaking effects of $Cu(In,Ga)Se_2$ solar cells with ALD-Zn (O,S) and CBD-ZnS(O,OH) buffer layers, Sol Energ Mat Sol C, 143 (2015) 159-167.
[126] T. Nakada, M. Mizutani, 18% efficiency Cd-free $Cu(In, Ga)Se_2$ thin-film solar cells fabricated using chemical bath deposition (CBD)-ZnS buffer layers, Japanese Journal of Applied Physics, 41 (2002) L165-L167.
[127] R.V. Forest, E. Eser, B.E. McCandless, J.G.G. Chen, R.W. Birkmire, Effect of Na on $Cu(In,Ga)Se_2$ in-plane conductance and Seebeck coefficient, in: 2014 IEEE 40th Photovoltaic Specialist Conference (PVSC), 2014, pp. 345-349.
[128] I. Repins, M. Contreras, M. Romero, Y.F. Yan, W. Metzger, J. Li, S. Johnston, B. Egaas, C. DeHart, J. Scharf, B.E. McCandless, R. Noufi, Characterization of 19.9%-Efficient CIGS Absorbers, in: 2008 33rd IEEE Photovoltaic Specialists Conference (PVSC), 2008, pp. 1127-1132.
[129] P.T. Erslev, J.W. Lee, W.N. Shafarman, J.D. Cohen, The influence of Na on metastable defect kinetics in CIGS materials, Thin Solid Films, 517 (2009) 2277-2281.
[130] N. Naghavi, D. Abou-Ras, N. Allsop, N. Barreau, S. Bucheler, A. Ennaoui, C.H. Fischer, C. Guillen, D. Hariskos, J. Herrero, R. Klenk, K. Kushiya, D. Lincot, R. Menner, T. Nakada, C. Platzer-Bjorkman, S. Spiering, A.N. Tiwari, T. Torndahl, Buffer layers and transparent conducting oxides for chalcopyrite $Cu(In,Ga)(S,Se)_2$ based thin film photovoltaics: present status and current developments, Progress in Photovoltaics: Research and Applications, 18 (2010) 411-433.
[131] S. Siebentritt, Alternative buffers for chalcopyrite solar cells, Solar Energy, 77 (2004) 767-775.
[132] P. Xin, C.P. Thompson, J.K. Larsen, W.N. Shafarman, Sputtered zinc selenide buffer layers for $Cu(InGa)Se_2$ substrate and superstrate solar cells, in: Photovoltaic Specialist Conference (PVSC), 2014 IEEE 40th, 2014, pp. 0443-0447.
[133] T. Yoshida, R.W. Birkmire, Fabrication of $CuInSe_2$ solar cells in a superstrate configuration, in: Proceedings of the 11th EC Photovoltaic Solar Energy Conference, 1992, pp. 811.
[134] T. Nakada, N. Okano, Y. Tanaka, H. Fukuda, A. Kunioka, Superstrate-type $CuInSe_2$ solar cells with chemically deposited CdS window layers, in: Conference Record of the Twenty Fourth. IEEE Photovoltaic Specialists Conference, IEEE, 1994, pp. 95-98.
[135] T. Nakada, T. Mise, High-efficiency superstrate type CIGS thin film solar cells with graded bandgap absorber layers, in: Proceedings of the 17th European Photovoltaic Solar Energy Conference, 2001, pp. 1027-1030.

[136] F.J. Haug, D. Rudmann, G. Bilger, H. Zogg, A.N. Tiwari, Comparison of structural and electrical properties of Cu(In,Ga)Se_2 for substrate and superstrate solar cells, Thin Solid Films, 403 (2002) 293-296.
[137] J.K. Larsen, P. Xin, W.N. Shafarman, Formation of Ga_2O_3 barrier layer in Cu(InGa)Se_2 superstrate devices with ZnO buffer layer, in: MRS Proceedings, Cambridge University Press, 2013, pp. 67-72.
[138] M.D. Heinemann, V. Efimova, R. Klenk, B. Hoepfner, M. Wollgarten, T. Unold, H.-W. Schock, C.A. Kaufmann, Cu(In,Ga)Se_2 superstrate solar cells: prospects and limitations, Progress in Photovoltaics: Research and Applications, (2014).
[139] F.J. Haug, D. Rudmann, H. Zogg, A.N. Tiwari, Light soaking effects in Cu(In,Ga)Se_2 superstrate solar cells, Thin Solid Films, 431 (2003) 431-435.
[140] F. Engelhardt, M. Schmidt, T. Meyer, O. Seifert, J. Parisi, U. Rau, Metastable electrical transport in Cu(In,Ga)Se_2 thin films and ZnO/CdS/Cu(In,Ga) Se_2 heterostructures, Phys Lett A, 245 (1998) 489-493.
[141] M.N. Ruberto, A. Rothwarf, Time-Dependent Open-Circuit Voltage in $CuInSe_2$/Cds Solar Cells: Theory and Experiment, J Appl Phys, 61 (1987) 4662-4669.
[142] M.D. Heinemann, D. Greiner, T. Unold, R. Klenk, H.W. Schock, R. Schlatmann, C.A. Kaufmann, The Importance of Sodium Control in CIGSe Superstrate Solar Cells, Ieee J Photovolt, 5 (2015) 378-381.
[143] P. Jackson, D. Hariskos, R. Wuerz, O. Kiowski, A. Bauer, T.M. Friedlmeier, M. Powalla, Properties of Cu(In,Ga)Se_2 solar cells with new record efficiencies up to 21.7%, Physica Status Solidi RRL, 9 (2014) 28-31.
[144] J.D. Wilson, R.W. Birkmire, W.N. Shafarman, In-situ annealing of Cu(In,Ga)Se_2 films grown by elemental co-evaporation, in: Photovoltaic Specialists Conference, 33rd IEEE, 2008.
[145] B.E. McCandless, R.W. Birkmire, $CdTe_{1-x}S_x$ absorber layers for thin-film CdTe/CdS solar cells, in: Conference Record of the Twenty Sixth IEEE Photovoltaic Specialists Conference, 1997, pp. 307-312.
[146] R. Saez-Araoz, J. Krammer, S. Harndt, T. Koehler, M. Krueger, P. Pistor, A. Jasenek, F. Hergert, M.C. Lux-Steiner, C.H. Fischer, ILGAR In_2S_3 buffer layers for Cd-free Cu(In,Ga)$(S,Se)_2$ solar cells with certified efficiencies above 16%, Prog Photovoltaics, 20 (2012) 855-861.
[147] D. Abou-Ras, B. Marsen, T. Rissom, F. Frost, H. Schulz, F. Bauer, V. Efimova, V. Hoffmann, A. Eicke, Enhancements in specimen preparation of Cu(In,Ga)$(S,Se)_2$ thin films, Micron, 43 (2012) 470-474.
[148] P. Xin, J.K. Larsen, F. Deng, W.N. Shafarman, Development of Cu(In,Ga)Se_2 superstrate devices with alternative buffer layers, Sol Energ Mat Sol C, 157 (2016) 85-92.
[149] M.D. Heinemann, J. Berry, G. Teeter, T. Unold, D. Ginley, Oxygen deficiency and Sn doping of amorphous Ga_2O_3, Appl Phys Lett, 108 (2016) 022107.
[150] J.K. Larsen, H. Simchi, P. Xin, K. Kim, W.N. Shafarman, Backwall superstrate configuration for ultrathin Cu(In,Ga)Se_2 solar cells, Appl Phys Lett, 104 (2014).

Appendix A

PUBLICATION LIST

Larsen, Jes K., Peipei Xin, and William N. Shafarman. "Formation of Ga_2O_3 barrier layer in Cu(InGa)Se_2 superstrate devices with ZnO buffer layer." In MRS Proceedings, vol. 1538, pp. 67-72. Cambridge University Press, 2013.

Larsen, Jes K., H. Simchi, P. Xin, K. Kim, and W. N. Shafarman. "Backwall superstrate configuration for ultrathin Cu (In,Ga)Se_2 solar cells." Applied Physics Letters 104, no. 3 (2014): 033901.

Xin, Peipei, Christopher P. Thompson, Jes K. Larsen, and William N. Shafarman. "Sputtered zinc selenide buffer layers for Cu(InGa)Se_2 substrate and superstrate solar cells." In 2014 IEEE 40th Photovoltaic Specialist Conference (PVSC), pp. 0443-0447. IEEE, 2014.

Kim, Kihwan, Peipei Xin, Jaeho Yun, and William N. Shafarman. "V_{OC} enhancement of sub-micron CIGS solar cells by sulfization of the Mo surface." In Photovoltaic Specialist Conference (PVSC), 2015 IEEE 42nd, pp. 1-4. IEEE, 2015.

Xin, Peipei, Jes K. Larsen, Fei Deng, and William N. Shafarman. "Development of Cu(In,Ga)Se_2 superstrate devices with alternative buffer layers." Solar Energy Materials and Solar Cells, 157 (2016): 85-92.

Appendix B

REPRINT PERMISSIONS

Part of Chapter 3 comes from a published IEEE paper cited below. The reprint permissions are granted by default for Thesis resus.

Xin, Peipei, Christopher P. Thompson, Jes K. Larsen, and William N. Shafarman. "Sputtered zinc selenide buffer layers for Cu(InGa)Se_2 substrate and superstrate solar cells." In 2014 IEEE 40th Photovoltaic Specialist Conference (PVSC), pp. 0443-0447. IEEE, 2014.

Part of Chapter 5 comes from a published paper in the journal Solar Energy Materials and Solar Cells. The reuse of the data in Thesis is with permission from: Xin, Peipei, Jes K. Larsen, Fei Deng, and William N. Shafarman. "Development of $Cu(In,Ga)Se_2$ superstrate devices with alternative buffer layers." Solar Energy Materials and Solar Cells, 157 (2016): 85-92, Elsevier, December 2016.

Order Completed

Thank you for your order.

This Agreement between Peipei Xin ("You") and Elsevier ("Elsevier") consists of your license details and the terms and conditions provided by Elsevier and Copyright Clearance Center.

Your confirmation email will contain your order number for future reference.

Printable details.

License Number	4026510771773
License date	Jan 12, 2017
Licensed Content Publisher	Elsevier
Licensed Content Publication	Solar Energy Materials and Solar Cells
Licensed Content Title	Development of Cu(In,Ga)Se2 superstrate devices with alternative buffer layers
Licensed Content Author	Peipei Xin,Jes K. Larsen,Fei Deng,William N. Shafarman
Licensed Content Date	December 2016
Licensed Content Volume	157
Licensed Content Issue	n/a
Licensed Content Pages	8
Type of Use	reuse in a thesis/dissertation
Portion	full article
Format	both print and electronic
Are you the author of this Elsevier article?	Yes
Will you be translating?	No
Order reference number	
Title of your thesis/dissertation	Alternative Buffer Layer Development in Cu(In,Ga)Se2 Thin Film Solar Cells
Expected completion date	Feb 2017
Estimated size (number of pages)	150
Elsevier VAT number	GB 494 6272 12
Requestor Location	Peipei Xin 451 Wyoming Road Institute of Energy Conversion NEWARK, DE 19716 United States Attn: Peipei Xin
Total	0.00 USD